REACTOR DESIGN PARAMETERS, IN-SITU SPECIATION IDENTIFICATION, AND POTENTIAL BALANCE MODELING FOR NATURAL ORGANIC MATTER REMOVAL BY ELECTROCOAGULATION

by

Kristian Lukas Dubrawski

B.A.Sc., The University of British Columbia, 2007

M.A.Sc., The University of British Columbia, 2008

A THESIS SUBMITTED IN PARTIAL FULFILMENT OF THE REQUIREMENTS FOR THE DEGREE OF

DOCTOR OF PHILOSOPHY

in

The Faculty of Graduate Studies

(Chemical and Biological Engineering)

THE UNIVERSITY OF BRITISH COLUMBIA
(Vancouver)

April 2013

Abstract

Electrocoagulation (EC), a disruptive "green" technology, was investigated for the removal of natural organic matter (NOM) from drinking water sources. Three anode materials (aluminum, zinc, and iron) and three NOM sources (Suwannee, Nordic, and a local source) were investigated. After one minute of process time, dissolved organic carbon (DOC) reduction was approximately 70-80%. High performance size exclusion chromatography (HPSEC) fractionation showed reductions mostly in the larger apparent molecular weight (AMW) fraction of NOM, from 76% of NOM > 1450 Da initially to approximately 40% after EC. For iron EC, significant EC design variables were investigated, including: current density (*i*) (2.43 to 26.8 mA/cm^2), and charge loading rate (*CLR*) (100 to 1000 C/L/min). Optimum NOM removal was found at *i* ~10 mA/cm^2 and lower *CLR*. *In-situ* identification of iron speciation in EC investigated the impact of *i* and *CLR* on speciation and NOM removal from a local natural source. Low *i* and intermediate *CLR* increased bulk pH and reduced bulk dissolved oxygen (DO), where green rust (GR) was identified *in-situ* for the first time in EC by Raman spectroscopy. Further oxidation at higher *i* and *CLR* led to magnetite (Fe_3O_4) formation, while all other conditions led to increased DO and/or increased pH, with subsequent identification of only orange lepidocrocite (γ-FeOOH). GR showed the marginally higher NOM DOC and AMW fraction reductions. In synthetic water, differing operating parameters led to differences in φ and iron speciation, characterized by *in-situ* Raman spectroscopy, aqueous XRD, SEM, and cryo-TEM. High *i* in the presence of pitting promoters led to φ near unity where a GR intermediate was seen, and an end product of Fe_3O_4. A mechanism scheme summarizing EC speciation is proposed. A

general model relating cell potential and current was developed for parallel plate continuous EC, relying only on geometric and tabulated variable inputs. For the model, the anode and cathode were vertically divided into *n* equipotential segments. Potential and energy balances were simultaneously solved for each vertical segment iteratively. Model results were in good agreement with experimental data, mean relative deviation was 9% for a low flow rate, narrow electrode gap, and polished electrodes.

Preface

The work performed in this thesis included the supervision of several students and the resulting submission of several manuscripts to top journals in the field of environmental and water technology. Chapter 2, investigating the metal type and natural organic matter source for electrocoagulation, was completed with the assistance of summer student Miléna Fauvel, from the Ecole Nationale Supérieure de Chimie de Rennes, France. It was submitted as:

> Dubrawski, K.L.; Fauvel, M., Mohseni, M., 2012. Metal Type and Natural Organic Matter Source for Direct Filtration Electrocoagulation of Drinking Water. *Submitted.*

Chapter 3, investigating the operating parameters of iron EC on NOM removal, was submitted as:

> Dubrawski, K.L.; Mohseni, M., 2012. Standardizing Electrocoagulation Reactor Design: Iron Electrodes for NOM Removal. *Submitted.*

Chapter 4, investigating the identification and impact of iron speciation on NOM removal in EC, was submitted as:

> Dubrawski, K.L.; Mohseni, M., 2012. *In-situ* identification of iron electrocoagulation speciation and application for natural organic matter (NOM) removal. *Submitted.*

Chapter 5, investigating the identification of speciation and transformation in iron EC, is in preparation as:

> Dubrawski, K.L.; Mohseni, M., 2012. Speciation and transformation of electrochemically generated iron nanoparticles in electrocoagulation. *In preparation.*

Chapter 6, modeling the potential-current relationship in EC, was completed with the assistance of undergraduate thesis student Codey Du, and submitted as:

> Dubrawski, K.L.; Du, C., Mohseni, M., 2012. General Potential-Current Model and Validation for Electrocoagulation. *Submitted.*

Appendix B, the comparison of EC to chemical coagulation and bench-scale pilot, was submitted to the refereed American Water Works Association Water Quality Technology Conference (the top water technology conference in North America) as:

> Dubrawski, K.L.; Mohseni, M., 2012. Electrocoagulation for NOM Removal From Natural Water Without pH Control or Addition of Conductivity Enhancing Salts *In Proceedings of American Water Works Association – Water Quality Technology Conference 2012*.

Other contributions during Mr. Dubrawski's tenure as a Ph.D. student at UBC included:

- Collaboration with a major university-industry partnership, including a multi-million proposal to treat UBC's domestic wastewater with iron EC as a "Campus as a Living Laboratory" research-industry partnership. This proposal is being evaluated as of 2012.
- Contributions from Chapter 5, and a process, known as "magneto-EC", discovered by Mr. Dubrawski while on academic exchange at Lawrence Berkeley National Laboratory, led to one patent submission in a UBC/University of California, Berkeley collaboration, and one US Department of Energy research funding proposal totaling $1 million USD.

- Contributions from Mr. Dubrawski's tenure as a doctorate student in the UBC Bridge Program (2009) led to a successful NSERC/CIHR proposal, studying the effects of industry on Aboriginal Health:

  > Gamontle, B., Dubrawski, K. and Elliott, M. (2010) Unearthing and Communicating Health Implications and Possible Interventions for Aboriginal Communities Experiencing Mine Development in Canada. Tri-agency knowledge synthesis proposal developed for UBC BRDG 501/601 (collaboration between industry and academia). Awarded $100 000.

  The research here also led to Mr. Dubrawski being awarded the UBC SPPH Joel Bert Award, Pacific Century Scholarship, being named a Liu Scholar, and teaching as a Sessional Instructor at UBC CHBE, teaching on health, safety and risk assessment in CHBE 479.

- Three students were directly supervised by Mr. Dubrawski during the course of this research: one undergraduate thesis in Chemical and Biological Engineering (Codey Du, UBC B.A.Sc. CHBE class of 2012), and two exchange students from the Department of Chemistry from the Ecole Nationale Supérieure de Chimie de Rennes, France at the M.A.Sc. equivalent level (Miléna Fauvel - 2011, and Régis Kister – 2012), several students were also advised in EC research from research and conference meetings.

- This research also led to a panel discussion at the RES'EAU WaterNET Knowledge Transfer Workshop on global water issues, which Mr. Dubrawski moderated. Guests included representatives from academia, industry, and the United Nations think-tank on water.

Table of Contents

List of Tables

List of Figures

List of Abbreviations

AAS – atomic absorption spectroscopy

AMW – apparent molecular weight

AWWA – American Water Works Association

BOD – biological oxygen demand

CDWQ – Canadian Drinking Water Quality

CL – charge loading

CLR – charge loading rate

CNOM – chromophoric natural organic matter

COD – chemical oxygen demand

Cryo-TEM – cryogenic transmission electron microscopy

DBP – disinfection by-product

DO – dissolved oxygen

DOC – dissolved organic carbon

EC – electrocoagulation

GR – green rust

HGMS – high gradient magnetic separation

HPLC – higher performance liquid chromatography

ICP-OES – Inductively coupled plasma optical emission spectroscopy

IR – infra-red

LCA – life cycle assessment

LGMS – low gradient magnetic separation

ML – metal loading

MW – molecular weight

MW – molecular weight

NOM – natural organic matter

PPER – parallel plate electrochemical reactor

PVA – poly-vinyl acid

RO – reverse osmosis

RSE – relative standard error

SAV – surface area to volume ratio

SE – standard error

SEC – size exclusion chromatography

SEM – scanning electron microscopy

SUVA – specific ultraviolet absorbance

TDS – total dissolved solids

TDS – total dissolved solids

THM – tri-halo methane

TOC – total organic carbon

UNEP – United Nations Environmental Programme

UV – ultraviolet

UV-abs-254 – absorbance of ultraviolet light at 254 nm

VIS-abs-420 – absorbance of the visible light spectrum at 420 nm

XRD – x-ray diffraction

List of Symbols

A – nominal electrode area [m^2]

b_a – anodic Tafel slope [mV/dec]

b_c – cathodic Tafel slope [mV/dec]

C_p – heat capacity [J/mol/K]

CL – charge loading [C/L]

CLR – charge loading rate [C/L/min]

d – inter-electrode distance [m]

dA – segment electrode area [m^2]

dV – volume between electrodes [m^3]

dy – height of each segment [m]

E^0 – equilibrium cell potential [V]

E_a^0 – anodic equilibrium potential [V]

E_c^0 – cathodic equilibrium potential [V]

E_a^T – anodic equilibrium potential at temperature T [V]

E_c^T – cathodic equilibrium potential at temperature T [V]

$E_{a,j}$ – anodic potential at segment j [V]

$E_{c,j}$ – cathodic potential at segment j [V]

E_{cell} – cell potential [V]

E_j – cell potential at segment j [V]

F – Faraday's constant [A·s/mol]

Fe_{ris} – residual iron [mg/L]

$\dot{H_{in,J}}$ – enthalpy flow into segment *j*, relative to elements at standard state and 298K [W]

$\dot{H_{out,J}}$ – enthalpy flow out of segment *j*, relative to elements at standard state and 298K [W]

$\dot{H}_{2,j}$- hydrogen flow rate at segment *j* [m^3/s]

h – electrode height [m]

h_f– enthalpy of formation [J/mol]

i - current density [A/m^2]

$i_{0,a}$ – anodic exchange current density at segment *j* [A/m^2]

$i_{0,c}$ – cathodic exchange current density at segment *j* [A/m^2]

$i_{a,j}$ – anodic current density at segment *j* [A/m^2]

$i_{c,j}$ – cathodic current density at segment *j* [A/m^2]

$I_{Fe,exp}$ – current going to iron dissolution, experimental [A]

$I_{Fe,th}$ – current going to iron dissolution, theoretical [A]

I_j – cell current at segment *j* [A]

i_j – current density at segment *j* [A/m^2]

i_L – limiting current density [A/m^2]

j – segment number [dim]

n – number of experiments performed, or number of electrode segmentations [dim]

$\dot{n}$ – molar flow [mol/s]

$\dot{n}_{H_2,gen,j}$ – molar generation rate of hydrogen gas at segment *j* [mol/s]

$\dot{n}_{Fe(OH)_2,gen,j}$ – molar generation rate of ferrous hydroxide at segment *j* [mol/s]

$p_{H_{2_0}}$ – initial partial pressure of hydrogen gas [Pa]

$p_{H_{2_n}}$– reactor exit partial pressure of hydrogen gas [Pa]

pH_0 – initial pH [dim]

pH_n – reactor exit pH [dim]

$\dot{Q}_J$ – heat flow entering or exiting dV at segment *j* [W]

R – Universal gas constant, or resistance [J/mol·K], [Ω]

R_j – resistance at segment *j* [Ω]

ΔS – entropy change [J/mol·K]

t – Student's t-test variable [dim]

T – temperature [K]

T_0 – initial temperature [K]

T_j – temperature at segment *j* [K]

T_n – temperature at reactor exit [K]

U_0 – superficial velocity of liquid in PPER [m/s]

U_n – superficial velocity of liquid at PPER exit [m/s]

w – electrode width [m]

$\dot{W}_J$ – work flow entering or exiting dV at segment *j* [W]

$\dot{V}$ – solution flow rate [m^3/s]

$\measuredangle X$ – absolute error

z – charge transfer number [dim]

Greek Symbols

α – charge transfer coefficient [dim]

α_k – conductivity temperature coefficient [1/K]

$\epsilon_{L,0}$ – initial liquid volume fraction [dim]

$\epsilon_{L,j}$ – liquid volume fraction at segment j [dim]

$\epsilon_{g,j}$ – gas volume fraction at segment j [dim]

κ – conductivity [S/m]

κ_0 – initial conductivity [S/m]

κ_n – conductivity at reactor exit [S/m]

κ_j – conductivity at segment *j* [S/m]

κ_j^T - conductivity at segment *j*, adjusted for temperature *T* [S/m]

ζ – mean relative deviation [%]

μ – experimental mean

η – overpotential [V]

η_{Mt} – mass transfer overpotential [V]

$\eta_{a,j}$ – anodic overpotential at segment j [V]

$\eta_{c,j}$ – cathodic overpotential at segment j [V]

η_k – kinetic overpotential [V]

η_{ohmic} – ohmic overpotential [V]

σ – slip ratio [dim]

σ_x – experimental standard deviation

φ – current efficiency [dim]

$\nabla\Phi$ – electric field [V/m]

$[Fe^{2+}]_0$ – initial ferrous iron concentration [mol/m^3]

$[Fe^{2+}]_n$ - exit ferrous iron concentration [mol/m^3]

Acknowledgements

To my wife Emma, the source of all my strength and happiness.

To my family, thank-you for teaching me everything I know today.

To my supervisor, Prof. Mohseni, thank-you for your guidance and friendship.

To Dr. Susan Addy and Prof. Ashok Gadgil at the UC-Berkeley ECAR group, for the inspiration and opportunity to work with your arsenic group in Berkeley and in India.

To my labmates: Bradley, Laith, Sona, Mehdi(s), Clara, Ramin, Ran, Ken, and Gustavo.

To the students I have taught and supervised over the years. Thank-you for your patience.

To the CHBE machine shop. For putting up with my 1/1000 inches of perfectionism.

To Tanya, Chad, Prof. Turner and Prof. Blades at the Michael Smith Labs – thank-you for teaching me your wealth of Raman spectroscopy knowledge and techniques.

To Brad and Garnet, for the excellent cryo-TEM sample preparation advice.

To Dr. Arman Bonakdarpour – For your ideas and expertise in electrochemistry and physics.

To Prof. Wilkinson – for the use of your lab's multistat and fuel cell lab.

To Prof. Gyenge, Prof. Bizzotto, and Prof. Oloman, for the helpful teaching, manuscript preparation, and advice.

Dedication

To the children of Africa who drink unsafe water …

The most humiliating (and angering) experience in my life has been to watch children drink unsafe river water and not be able to do anything about it; for lack of a treatment technology or safer alternative. This happened in rural West Africa six years ago, during an era of unprecedented wealth in the Western world. The same water sent me home to Canada emaciated and ill; but worse, caused the death of one of my local hosts, an otherwise healthy father of two. At any given moment, half of the world's hospital beds are occupied by people suffering from water-borne diseases. One in five deaths in Bangladesh is caused by arsenic in the well water. Over one million children die each year of water-borne disease. This is completely unjust. Lest I forget, we are also running out of water at home. Agriculture and industry consume our water resources faster than natural recharge rates. Emerging anthropogenic contaminants include carcinogens that are consumed daily by millions.

Why do a Ph.D. then? I believe that public research has an important role in linking the water, health, and environment nexus, something I can see myself doing in a research career. I believe in a world where clean, sustainable, and affordable water is accessible to all. This world can (and will) happen, but it is up to us as citizens and leaders as to when it will - the second most humiliating experience in my life would be if I stood idle and waited for this world to happen. I am humbled and inspired by every small difference that brings our global community closer to this goal.

"You cannot change the world, but you can make changes."

1. Introduction

1.1. Drinking Water

The world's supply of uncontaminated freshwater is becoming increasingly scarce. About one-third of the world's population currently resides in countries with moderate to high water stress, defined by the United Nations to be water consumption that exceeds ten percent of renewable freshwater resources. By 2020, water use is expected to increase by 40%, and by 2025, 1.8 billion people will be living with absolute water scarcity, and two out of three people could be living under conditions of water stress (UNEP, 2007). Surface waters, including lakes, rivers and streams, are most at risk due to their proximity to industrial civilization – good watershed protection and management are critical to the protection of these drinking water sources. In areas where water protection is compromised, treatment strategies must minimize environmental and economic burden. These technologies are varied in terms of pollutant selectivity, scale, cost, effectiveness, and appropriateness. In small, decentralized settings, treatment options are often expensive and/or difficult to operate and maintain. This thesis focused specifically on small community water systems appropriate for rural Canada and in developing nations, and investigated one specific and potentially disruptive physicochemical technology, electrocoagulation (EC), to treat a community's drinking water supply. The water constituent of focus for this thesis was natural organic matter (NOM), which causes disagreeable taste and colour, absorption of UV light (rendering UV disinfection infeasible), filter fouling, and is known to react with halogen disinfectants to create suspected carcinogenic disinfection by-products (DBPs) such as tri-halo-methanes (THMs). NOM is

typically removed by the addition of chemical salts (such as aluminum or iron salts) with subsequent pH adjustment, which can be costly and difficult for small communities. This thesis proposes EC as an effective, easy-to-implement, low footprint solution for NOM removal, as well as digging deeper into the principles and science of EC in general.

1.2. Research Objectives and Chapters

The structure of this thesis was written as a logically flowing narrative, with each chapter of the thesis separated into a clear and concise research topic. Each chapter was built on the knowledge accumulated from the previous, which led to the development of the process from a broad investigation in bulk pollutant removal to specific analyses of metal speciation and electrochemical modeling of EC as a continuous process. This thesis looked at five separate tasks, each with specific objectives:

i) Quantifying NOM removal with EC,
    a. Demonstrate the capability of direct filtration EC to reduce levels of NOM from levels of 10-20 mg/L DOC by USEPA guidelines of at least 50%.
    b. Compare the NOM removal capabilities of three metals: zinc, aluminum, and iron in three different sources of NOM: Suwannee River, Nordic Reservoir, and locally sourced natural water.
    c. Investigate the effect of initial NOM concentration and co-occurring solutes on the robustness of EC to handle input waters of differing properties.

ii) Optimizing iron EC design for NOM removal,

    a. Investigate specific EC parameters, including: current density, charge loading rate, and flocculation mode, on metal use and electrical consumption for NOM removal.

    b. Investigate the speed of the process, its applicability for settling or filtration, and appropriateness for differing scales of operations.

iii) Investigating iron EC for NOM removal in natural water,

    a. Investigate the previous EC parameters as to their impact on pH and dissolved oxygen during the EC process.

    b. Determine the effects of these parameters on the speciation of iron oxides and hydroxides.

    c. Develop a suitable *in-situ* identification experiment for differentiation of species during the EC NOM removal process.

iv) Further investigating iron EC,

    a. Determine the operating parameters that lead to different speciation in synthetic water.

    b. Determine the role of differing solute types and concentrations on speciation.

    c. Develop an EC process mechanism scheme, describing the variables that lead to differing speciation.

v) Investigating the cell potential and current relationship in a parallel plate continuous EC reactor,

a. Create a numeric model predicting cell current based on potentiostatic operation.
b. Determine if the model is appropriate without the use of experimentally derived values or constants.
c. Apply the model to an experimental reactor, and test the robustness with regards to differing geometries, solutes, and electrode surface conditions.

Tasks i), ii), and iii) were specific to NOM removal, while tasks iv) and v) were generalizable to pollutants other than NOM. The knowledge generated by this thesis is likely the most comprehensive and scientific contribution to EC drinking water treatment to date. Positive impact is expected for several stakeholders: small communities in Canada dealing with water treatment issues, low-income nations looking for cost-effective water and wastewater treatment technologies, industries developing EC as a "green" chemical-free technology, and the academic community researching the scientific fundamentals of EC. A summary of error analysis and a general literature review on EC follows. The literature review is meant to be an introduction to EC literature, and not specific to the research chapters. A more specific review introduces each chapter, which is directly relevant to the chapter's research goals. For convenience, abbreviations are often repeated in chapter introductions, to allow better readability of chapters independently.

1.3. Literature Review

An emerging research field in drinking water treatment is the *in-situ* electrochemical generation of metal hydroxide coagulants, often called electro-coagulation (EC), which has demonstrated an ability to remove biological pathogens (Mills, 2000; Zhu et al., 2005; Ghernaout et al., 2008), arsenic (Ratna Kumar et al., 2004; Song et al., 2006; Gomes et al., 2007; Martínez-Villafañe et al., 2009), iron (Ghosh et al., 2008), fluoride (Mameri et al., 1998; Hu et al., 2003), nitrate (Kumar and Goel, 2010), natural organic matter (Jiang et al., 2002; Vepsäläinen et al., 2009), and turbidity (Holt et al., 2005) from a wide range in quality of source water. The advantages of EC over conventional chemical (typically alum) coagulation have been discussed (Mollah et al., 2004), including: more effective at pollutant removal, safer and more environmentally friendly due to avoiding the handling of chemicals, more efficient by using up to 100 times less metal, and more robust and better suited to automation, requiring as little maintenance as one electrode replacement once or twice per year. In community drinking water systems, alum and iron salts are still the most commonly used coagulant (Sobsey, 2002), despite the known advantages of EC.

A review of the seminal knowledge of EC, including wastewater and drinking water literature, is necessary in determining where the relevant knowledge gaps exist, and what steps other researchers have attempted in addressing these gaps. Much research in EC has been undertaken in wastewater treatment, exposing a wealth of knowledge for drinking water applications, both of which will be reviewed here.

1.3.1. Principles of EC

A lack of fundamental understanding of the mechanism of pollutant removal has hindered the mainstream use of EC, confining it to heuristic and empirical experimentation for niche applications. The science behind the EC reaction is a complex process, combining the sciences of electrochemistry, coagulation, and separation:

Electrochemistry: The coagulant metal is electrochemically dissolved into solution (Figure 1-1A), usually with the aid of a DC current. Generally speaking, the metal cations combine with hydroxides produced as a result of cathodic reduction of water, which also releases hydrogen bubbles. Pollutant removal is usually affected by the electric field and thus cannot be considered just as a different coagulant dosing technology. This is because: a) the electrochemical reaction can consume dissolved oxygen, b) the electric field can oxidize some polyvalent pollutants (As, Cr) to less soluble forms, and c) electrolytic gases inevitably change the mixing characteristics.

Coagulation: A generally accepted theory of the coagulation mechanism in EC has been proposed (Mollah et al., 2001): coagulants compress the diffuse layer of charged pollutant species, which reduces electrostatic inter-particle repulsion until Van Der Waals forces predominate, causing charge stabilization and coagulation (Figure 1-1B). The coagulated flocs create a sludge blanket that entraps and bridges colloids while providing active sites for adsorption of other pollutants.

Separation: The flocs are separated/clarified, usually by settling, flotation or filtration (Figure 1-1C), and the water is further disinfected.

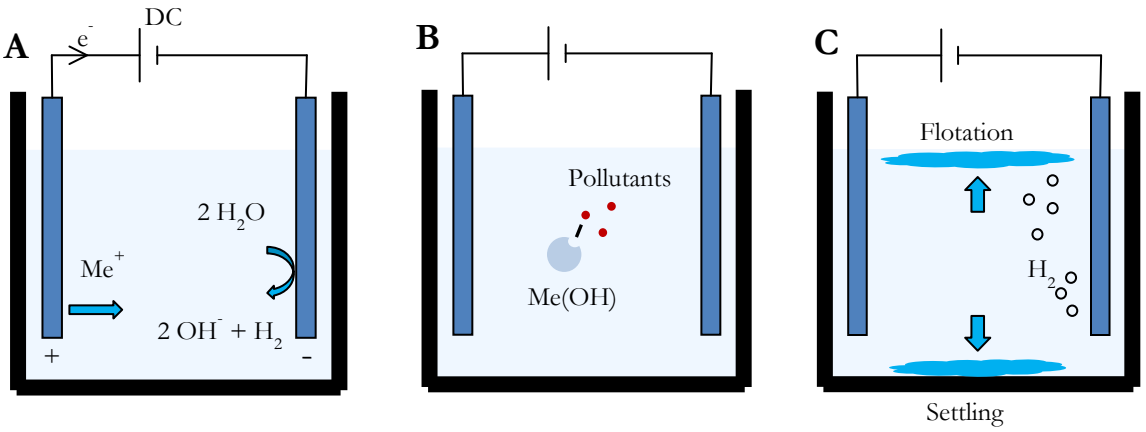

Figure 1-1: Principles of EC

1.3.2. Electrocoagulation in Wastewater Applications

The treatment of wastewater has seen the most common use of EC, dating from over a century ago, to more recent interest since the 1970s (Kul'skii et al., 1978). Success has already been found in niche applications, and several commercial wastewater treatment using EC operate today. Commercial patents include several EC designs (see Lazarevich, 1967; Cognot, 1995; Gardner, 1996; Chatnija, 1998; Almaz, 2001; Young-Sik, 2001; Lee, 2006) while the academic literature includes hundreds of studies, although most studies are limited to empirical "trial and error" due to a lack of alternative.

Mollah et al. (2001) describe the advantages of EC including: simple and easy to operate, giving palatable, colourless, and odorless water, low sludge production, and chemical-free.

The authors also describe some of the disadvantages, including: regular replacement of sacrificial anodes, possible passivation and loss of efficiency, conductivity enhancing salts may be required, and the gelatinous hydroxide may tend to solubilize under certain conditions. Several proposed coagulant generation and coagulation mechanisms are reviewed, as well as several reactor configurations.

Kim et al. (2002) studied the removal of organic dyes from wastewater in a continuous EC process varying several operating parameters: current density, number of electrodes, electrode gap, initial pollutant concentration, flow rate, NaCl concentration, and initial pH. The authors considered the reaction as a first-order plug flow tubular reactor, and found that the rate constant was largely controlled by the operating parameters governing the anodic dissolution, and quite independent of initial pH.

Koparal et al. (2008) used aluminum EC for the removal of humic substances in wastewater, varying initial concentrations of 100, 200, and 500 mg/L, and initial pH of 5, 7, and 8.5. Humic substance concentration was measured spectrophotometrically, and pH was controlled using HNO_3 and NaOH. The authors established that $Al(OH)_3$ production is not affected by initial pH (and presumed to be only by Faraday's Law), but that a gel layer on the anode caused decreasing pollutant removal rates at higher pHs. The authors concluded that below NOM concentrations of 200 mg/L, there are no pH limitations causing the gel layer, and thus removal efficiency should not be affected. Yildiz et al. (2008) performed similar experiments for NOM removal, determining optimum supporting electrolyte type (NaCl, Na_2SO_4, and $NaNO_3$) and concentration for different combinations of initial NOM

concentration and initial pH, finding an optimum level of 5 mM of Na_2SO_4 at lower initial pH values.

Shen et al. (2003) removed fluoride ions using aluminum electrodes with electroflotation in a continuous reactor. The influence of pH, cations (Ca^{2+}, $Mg^{2+,}$ Fe^{3+}), and anions (Cl^-, Br^-, SO_4^{2-}, PO_4^{3-}) were studied under a constant charge loading of 5 F / m^3. F^- was measured using an ion-sensitive electrode. At a pH of 2, only AlO_2^- (soluble) was formed, and thus no F^- removal was observed, and at pH > 10, no flocs were observed. The authors measured only charge loading, and not electrolysis time or current density, which led to one less control variable, but perhaps neglected the effects of secondary reactions at different currents and potentials. Competing anions were shown to reduce F^- removal, except for chlorine, probably due to the pitting-corrosion, which led to a 130% current efficiency. For cations, Ca^{2+} led to better fluoride removal, probably due to CaF_2 formation, which used $Al(OH)_3$ as nucleation sites. Fe^{3+} and Mg^{2+} aided F^- removal at concentrations of 50 mg/L, but larger concentrations led to the formation of $Fe(OH)_3$ and $Mg(OH)_2$, which precipitated on the $Al(OH)_3$ surface and has less affinity for fluoride removal. Sludge characteristics (elemental ratios) were determined with X-ray photoelectron spectroscopy (XPS) and time-of-flight secondary ion mass spectroscopy (SIMS).

Linares-Hernandez et al. (2007) coupled EC with biosorption in complex wastewater to reduce BOD, COD, colour, turbidity, and fecal coliforms. Cyclic voltammetry experiments showed a chemically irreversible oxidation peak at potentials lower than those corresponding to oxygen evolution, suggesting direct oxidation of pollutants. Moreno-

Casillas et al. (2007) re-examined the mechanism of EC in COD removal using a KALESCO bench scale EC unit and Fe Pourbaix thermodynamics, to determine that the variability in COD removal depends on floc formation (which happens at pH > 7.5), reactivity of Fe(II)/Fe(III) with various organic compounds, and final pH. Heidmann et al. (2008) performed a model heavy metal removal batch EC process with perforated electrodes at various current densities. The authors found that initial heavy metal concentrations did not affect removal rates for most heavy metals except Cr. This is one of the few studies to monitor the co-removal of several pollutants simultaneously.

Wu et al. (2008) compared EC with advanced oxidation processes such as UV/TiO_2 and ozone combinatory systems for textile dye removal, finding the following order for removal: O_3 (24W) > O_3 (16W) > O_3 (16W)/EC(8W) > UV/TiO_2/O_3 (8W)/EC(8W) > O_3 (10W) > UV/O_3 (8W)/EC(8W) > UV/O_3 (8W) > O_3 (8W) > UV/TiO_2/O_3 (8W) > O_3 (8W)/EC(8W) > O_3 (4W)/EC (4W) > UV/TiO_2/EC(8W) > UV/TiO_2 > UV/EC(8W) > EC(8W). Hsing et al. (2007) found a decolourization of dye removal rate order of Fenton>EC>O_3/UV/TiO_2>O_3 and a TOC removal rate of O_3/UV/TiO_2 > O_3 >EC > Fenton for a 30 minute process. Khataee et al. (2009) found a similar decolourization order of Fenton > EC > UV/nano-TiO_2>Electro-Fenton. These experiments were done at small scale, but highlight the possibility of using generated Fe^{2+} for free radical generation and advanced oxidation of organic compounds.

The studies in this section are highlighted for their relevance in the current work of this thesis, and shown in Table 1-1.

Table 1-1: EC wastewater studies and relevance to thesis

Study	Investigated Parameters	Relevant Chapter(s)
Mollah et al. (2001)	- Reactor design - Electrochemistry - Coagulation mechanisms	All
Kim et al. (2002)	- Current density - Electrode gap - Initial pollutant concentration	Chapters 2, 3
Koparal et al. (2008)	- Effect on humic substances - Initial concentration - Initial pH	Chapters 2, 3
Yildiz et al. (2008)	- NOM initial concentrations - Electrolyte type - Electrolyte concentration	Chapters 2, 3
Shen et al. (2003)	- Electrolyte type - Current efficiency	Chapters 3, 6
Linares-Hernandez et al. (2007)	- Current efficiency - Cyclic voltammetry	Chapters 3, 6
Moreno-Casillas et al. (2007)	- Reactor design - Pourbaix thermodynamics	Chapters 3, 5, 6
Heidmann et al. (2008)	- Reactor design - Initial pollutant concentration	Chapters 2, 3, 5
Wu et al. (2008) Hsing et al. (2007) Khataee et al. (2009)	- Process combination - Advanced oxidation	Chapters 3, 4

1.3.3. Electrocoagulation in Drinking Water Applications

The advantages of EC soon became apparent for the drinking water treatment sector as well. A method for purification of drinking water using EC was first applied in the USA in 1946 (Stuart, 1946), and has been the topic of increasing research since 1984, with recent interest due to environmental and economic concerns. Vik et al. (1984) investigated EC using aluminum for small Norwegian drinking water systems, as small systems had problems

with pH control, chemical mixing, and alum dosing. Surface waters with TOC of 5.9-15.6 mg/L were tested in a flow-through reactor, with removal to a TOC level of ≈ 4 mg/L after ≈ 750 C of charge had passed between the electrodes.

Mameri et al. (1998) used empirical testing in the defluoridation of Saharan drinking water with an Al bipolar EC array, finding optimum conditions at 20 °C, inter-electrode distance of 2 cm, pH in the range of 5-7.6, current density of 75 A/m^2, and a SA/V ratio of 25 m^2/m^3 with first order kinetic fitting and without the addition of soluble salts. Mameri et al. (2001) refined the technology to work in a continuous system with an anode surface area of 1.6 m^2, allowing up to 1.5 m^3/h, reaching WHO fluoride limits within 12 minutes of residence time, with better results at 25 A than 60 A, likely due to electrolytic gas interference with fluoride adsorption.

Zhu et al. (2007) examined the mechanism of fluoride removal in EC with Al electrodes, investigating parameters such as pH, charge loading, current density, and initial fluoride concentration. The authors found that adsorption onto passivation layers on electrodes was responsible for the majority of the removal, and that higher current densities hindered this effect, leading to more fluoride adsorption in the flocs.

Mills (2000) developed a coaxial carbon steel anode and stainless steel cathode configuration in a continuous flow reactor capable of providing 32,600 L/day (presumably equating to 22.2 L/min) of treated lake or river water with a power consumption of about 14 W (8 A at a pulsating 1.75 V). The system used 45 anodes at a cost of approximately $3.00 per anode, to be replaced every six months. The author suggested that the small electrode gap of 1.58

mm provided an electric field on the order of 1900 V/m, which may have aided in the apparent elimination of spiked *E.coli*. Only one study was found relevant to virus removal, Zhu et al. (2005) used Fe EC prior to microfiltration using the MS2 macrophage as a surrogate virus, finding only 0.5 log removal without EC, and over 4-log removal with EC. The likely cause was virus sorption to iron hydroxide flocs and subsequent enmeshment and removal by filtration.

Holt et al. (2002) investigated EC using aluminum for clay suspension removal, dividing the process into a lag phase (12 minutes for 0.5 A) with no noticeable turbidity difference, a reactive phase (12-32 minutes) where the primary removal mechanism suggested is sweep flocculation causing 90% of the removal, and a stabilising phase (32-60 minutes) where there is only slight further turbidity decrease. The authors also found that the Al concentration during EC without clay present follows Faraday's law until a saturation point occurs, where excess Aluminum simply precipitates (at 30 mg/L at 30 min, 0 g/L clay, and 1 A). With clay present, the aluminum concentration does not follow Faraday's law because the clay provides binding sites which precipitate out as well, levelling off at 4 mg/L Al (60 minutes, 1 g/L clay, 1 A).

Jiang et al. (2002) found that EC-Electroflotation (EF) performed better than chemical alum coagulation in removing dissolved organic carbon (DOC), colour, and UV absorbance with a flow-through reactor at 0.001 m^3/h with bipolar and monopolar arrangements, current densities of 3-25 A/m^2 at pH of 6.5 and 7.8, using both potentiostatic and galvanostatic modes. The authors suggested that anomalous pitting corrosion did not affect Faradaic

yield because experiments were not done in the pitting potential range of -0.5 V SHE; however, localized pH changes were not investigated.

Mechelhoff (2009) examined the effects of electrode surface pre-treatment and solution composition, using electrochemical impedance spectroscopy and atomic force microscopy to quantify passivation on aluminum electrodes. The author compared polished and rough surface finishes of aluminum, and concluded that a rough surface demonstrated spontaneous depassivation, although this effect was not observed after the electrodes were allowed to age in solution. Likewise, the effect did not work in pilot-scale testing suggesting that other ionic substances present in natural water eliminated this effect. Pilot-scale operations were shown to increase steadily from an operating voltage of 100 V to 350 V over 300 minutes, demonstrating the wasteful effects of passivation. The extra energy was consumed in the growth of the passivation layer, and wasted as heat. Also, residual levels of aluminum were 0.2 mg/L, four times greater than the AWWA recommendation of 0.05 mg/L, requiring further processing.

In low-income settings for arsenic removal, Addy (2009) used Fe EC for arsenic removal, reducing As levels of 550 ppb to < 10 ppb in water with co-occurring phosphate, silicate, and carbonate, and showing no passivation on the Fe electrode up to a current density of 10 mA/cm^2. Interestingly, the author found larger removal capacity with lower current densities and increased contact time, while also ruling out oxygen evolution as a cause for decreasing removal capacity, suggesting that particles that are generated more slowly and coagulate slower allow for better As adsorption.

The studies in this section are highlighted for their relevance in the current work of this thesis, and shown in Table 1-2.

Table 1-2: EC drinking water studies and relevance to thesis

Study	Investigated Parameters	Relevant Chapter(s)
Vik et al. (1984)	- NOM concentration - Reactor design - Charge loading	Chapters 2, 3, 6
Mameri et al. (1998) Mameri et al. (2001)	- Temperature - Current density - Reactor design - Initial pH	Chapters 2, 3, 4
Zhu et al. (2007)	- Charge loading - Current density	Chapter 3
Mills (2000)	- Reactor design - Cell current-voltage relationship - Flow rate	Chapters 3, 6
Zhu et al. (2005)	- Process combination - Disinfection	Chapters 2, 3
Holt et al. (2002)	- Charge loading rate - Flocculation	Chapter 3
Jiang et al. (2002)	- Initial NOM concentration - Process combinations - Current density	Chapters 2, 3, 4
Mechelhoff (2009)	- Electrode passivation - Current density - Cell current-voltage relationship	Chapters 3, 6
Addy (2009)	- Charge loading rate - Iron formations	Chapters 3, 5

1.3.4. Modeling Studies of Electrocoagulation

The theoretical modeling of EC has been plagued by the complexity in achieving a mathematical relationship between an electrochemical reaction and a coagulation mechanism

affected at least in some part by an electric field. Still today, no study has successfully predicted the voltage-current relationship in EC or the coagulation rate and pollutant removal from theory alone. Nevertheless, several attempts are reviewed.

Matteson et al. (1995) modeled an EC coagulation and separation of ultra-fine kaolinite (mass median particle size of 1.2 μm) in distilled water. The model was applied to both a batch system and a continuously flowing continuous-stirred reactor array, and found relatively good agreement between theoretically derived and experimental coagulation rates. The model assumed that coagulation, and not the formation of ferrous ions, was the rate-determining step, supported by findings of no difference in coagulation rates for different electrode mesh sizes. The authors also found no significant difference in coagulation rates with different current densities because of the higher speed of the generation of ferrous ions, which was determined not to be the rate determining step. Instead, the authors suggested that the electrophoretic velocity, controlled by the potential between the two electrodes had a more significant effect, although no further explanation was given.

Chen et al. (2002) modeled the voltage balance in aluminum EC, using a combination of experimental variables and theoretical work. The total voltage required at a given current density included contribution from the equilibrium potential difference, anodic activation and concentration overpotentials, cathodic activation and concentration overpotentials, anodic passivation overpotential, and ohmic potential drop. Values of ionic concentration, equilibrium potential, Tafel parameters, equilibrium constants, and diffusion constants were grouped into constants and thus found "empirically" instead of from tabulated data. It is

doubtful whether this approach is applicable for more general cases, where one wants an estimate of voltage consumption before construction of a unit.

Carmona et al. (2006) modeled mathematically the removal of oil (measuring TOC) in an aluminum electrode plug-flow EC reactor with a batch flocculation reactor with recycle. The following assumptions were made: Faradaic efficiency of 150%, that the Al^{3+} is entirely converted to $Al(OH)_3$, that the solid phase is always in equilibrium with the liquid phase with fast external mass transport, and that the oil does not undergo any chemical reaction. A mass balance of Al(III) in the plug flow reactor (PFR) and one of either a Langmuir, Langmuir-type, or Freundlich isotherm was solved with a fourth-order Runge-Kutta method, showing that the Langmuir-type model best approximated experimental data at different current densities, decreasing oil content from 50 g/L to less than 5 g/L in a time of 75 minutes. Khemis et al. (2006) built on this model by incorporating the COD abatement latency period observed in experimental findings, and found good agreement of experimental results with modeling data when a coagulation "latency period" was accounted for.

Zongo et al. (2009) fit both Al and Fe EC polarization curves (forward, backward, and real wastewater treatment) to $E_{cell} = 0.1 + (d/\kappa)\, i + 0.20 \ln (i)$ where E_{cell} is the potential, d is the electrode gap, κ is the electrolyte specific conductivity, and i is the current density. The authors then modeled Cr (VI) removal, using experimentally derived constants for pollutant mass balances, as well as dimensionless Sherwood, Reynolds, and Schmidt numbers for mass balance at the cathode due to hydrogen bubble evolution.

Holt et al. (2005) briefly described a modeling algorithm for a clay pollutant coagulation mechanism using aluminum electrodes based on previous dissolved air flotation (DAF) modeling. The model suggested that under high current densities (27 A m^{-2}), flotation had a large effect on separation efficiency, while under low current densities (3.4 A m^{-2}), flotation is negligible and EC can be thought of as electro-dosing. However, the model did not account for any effects of an electric field, nor was it validated with experimental data.

Mechelhoff (2009) constructed a two-dimensional finite element model to investigate the distribution of ionic species during parallel plate aluminum dissolution to derive possible causes of spontaneous depassivation. The model used no experimental data, and simultaneously solved the Navier-Stokes and Nernst-Plank equations using tabulated coefficients and constants from literature, as well as some assumptions for unknown constants. The model showed uniform current density throughout the electroactive area of the reactor as well as a higher potential distribution that mirrors the ionic conductivity distribution.

The studies in this section are highlighted for their relevance in the current work of this thesis, and shown in Table 1-3.

Table 1-3: EC modeling studies and relevance to thesis

Study	Investigated Parameters	Relevant Chapter(s)
Matteson et al. (1995)	- Coagulation rate - Current density - Electrode potential	Chapters 3, 6
Chen et al. (2002)	- Cell current-voltage relationship - Current density	Chapter 6
Carmona et al. (2006) Khemis et al. (2006)	- Pollutant removal at varying charge loading - Effect of flocculation	Chapter 3
Zongo et al. (2009)	- Cell current-voltage relationship - Pollutant removal at varying charge loading	Chapters 3, 6
Holt et al. (2005)	- Current density - Charge loading rate - Effect of flocculation	Chapters 2, 3
Mechelhoff (2009)	- Electrode passivation - Current density - Cell current-voltage relationship	Chapter 6

1.3.5. Electrochemistry Studies of Electrocoagulation

Several studies have used advanced electrochemical techniques to aid in the understanding of the anodic dissolution and electrode passivation. Hu et al. (2003) used a potentiostat/galvanostat to determine the effects of co-existing anions (Cl^-. NO^{3-}, SO_4^{2-}) on fluoride removal using bipolar aluminum electrodes. The kinetic overpotential without anions rose from 10 V to 100 V due to the resistance of an aluminum hydroxide gel layer between electrodes, and performed best with Cl^- anions, probably due to pitting corrosion. Mouedhen et al. (2008) examined the behaviour of Al electrode polarization, pH evolution, amount of Al(III) released in an EC cell, finding that a minimum Cl^- concentration of 60

ppm is required to breakdown the anodic passivation layer, and an increase of current density leads to significantly shorter electrolysis times without a substantial increase in charge loading.

Sasson et al. (2009) studied Fe^{3+} and Fe^{2+} formation in distilled water from EC with perforated Fe electrodes, NaCl and an organic buffer (3-(N-morpholino)-propanesulfanoic acid) to avoid possible precipitates predicted with carbonate and phosphate buffers. 1,10 phenanthroline was added to "freeze" and quantify Fe^{2+} formation due to the fast oxidation of Fe^{2+} to Fe^{3+} with dissolved oxygen present, measured by UV absorbance. Total Fe was measured with flame AAS. Fe^{2+} to total Fe^{3+} ratio was between 82-91% for all pH and current density values tested, demonstrating that the principal EC product is $Fe^{2+,}$ which rapidly oxidizes to Fe^{3+} under normal operating conditions. Overpotential was deemed negligible due to cleaning of the electrodes with HCl, although short-term passivation during operation may still have occurred. At low pH, it was found that Fe^{2+} auto-dissolved in the absence of an electric field, and that at high pH, other reactions, such as the oxidation of water to non-dissolving oxygen gas occurred.

The studies in this section are highlighted for their relevance in the current work of this thesis, and shown in Table 1-4.

Table 1-4: EC electrochemistry studies and relevance to thesis

Study	Investigated Parameters	Relevant Chapter(s)
Hu et al. (2003)	- Cell current-voltage relationship - Co-occurring solutes	Chapters 3, 6
Mouedhen et al. (2008)	- Cell current-voltage relationship - Effect of Cl^- on passivation	Chapters 3, 5, 6
Sasson et al. (2009)	- Fe^{2+}/Fe^{3+} ratio - Effect of passivation	Chapters 3, 5, 6

1.3.6. Separation of Sludge

The separation of sludge is of great importance to the EC process, especially for drinking water production, as the treated water should be generated as close to on-demand as possible, and without suspended material in the effluent. Filtration is an obvious choice, although due to the gel-like sludge, pure filtration can incur a significant fouling on any membrane. Pure settling without filtration would be ideal, although the time required and/or the risk of disturbance of the sludge might hinder this. At least some settling would be beneficial to prevent membrane/filter fouling/clogging, as done in typical chemical coagulation processes, although the current literature of the settling characteristics in EC is sparse.

Hansen et al. (2006) used Fe electrodes to remove arsenic from wastewater in a continuous process with a nominal residence time of 9 min at 3 L/h. Aliquots were measured every 30 minutes for residual arsenic, showing that a steady state was found between 1.5 - 2.0 hours.

Addy (2009) investigated pure settling, and found a steady state time of 72 hours to achieve arsenic removal comparable to 0.1 μm membrane filtration.

Zodi et al. (2009) studied the settling properties of EC-treated industrial wastewater with high suspended solid content, high turbidity, and fair COD, showing that after settling and decantation, Al and Fe have similar values of SS and turbidity, and initial pH has a negligible effect. Settling rates were faster for Fe than Al, probably due to different morphology of $Fe(OH)_3$ and a lack of hydrogen bubbles which keep $Al(OH)_3$ from settling.

Larue and Vorobiez (2003) estimated electrochemically generated iron floc sizes from settling data in a 1 m settling chamber using a 16 μm kaolin suspension. The floc-supernatant interface settled from an initial height of 0.5 m to 0.1 m in about 20 minutes, which compared favourably to $FeCl_3$ and $FeSO_4$, and critical points were determined to estimate floc size using a Richardson and Zaki model. The estimation did not necessarily compare well to optical findings, but was regarded as a useful tool for quick estimation.

Other separation options include flotation and magnetic separation. Flotation is usually associated with wastewater treatment, as it generally does not remove the smallest particles required for the quality of drinking water, although it is still considered by some (Jiang et al., 2002). Magnetic separation is an attractive option, eliminating the need for both membrane filtration and settling. However, it is only associated with Fe, and only for the two stable ferromagnetic species, magnetite and maghemite. Tsouris et al. (2000) investigated EC as a magnetic seeding method for high-gradient magnetic separation in wastewater treatment, showing that 100 nm magnetite particles form in a distilled water/sodium chloride solution,

but magnetically susceptible product formation decreases with increased competitive cation and anion concentrations. Yavuz et al. (2006) showed that low-field strength magnetic filtration (<100 T/m) could remove magnetite particles (synthesized chemically, not electrochemically) of 12 nm in diameter, also showing a reduction in orders of magnitude of consumed iron associated with arsenic removal.

The studies in this section are highlighted for their relevance in the current work of this thesis, and shown in Table 1-5.

Table 1-5: EC sludge separation studies and relevance to thesis

Study	Investigated Parameters	Relevant Chapter(s)
Hansen et al. (2006)	- Effect of charge loading - Effect of flocculation	Chapters 2, 3
Addy (2009)	- Effect of settling times - Effect of charge loading	Chapter 3
Zodi et al. (2009)	- Effect of electrode type - Effect of settling time	Chapters 2, 3
Larue and Vorobiez (2003)	- Comparison with iron chemical coagulation - Effect of settling time	Chapters 2, 3
Tsouris et al. (2000) Yavuz et al. (2006)	- Effect of charge loading - Effect of co-occurring solutes - Effect of magnetic field	Chapters 3, 4, 5

1.3.7. Natural Water and NOM

The main components of natural surface water in Canada are organic, typically called natural organic matter (NOM), typically measured as DOC, and found in normal ranges of 2-10 mg/L, but levels up to 50 mg/L have been found during the spring snow-melt in forested areas of remote and/or northern Canada. The difference between DOC and total organic

carbon (TOC) is that DOC includes only carbon that passes through a 0.45 μm filter. UV absorbance at 254 nm (UV-abs-254) is also used to complement DOC data, which is expressed in unitless absorbance that passes through a 1 cm cuvette, hence expressed in units (cm^{-1}). Approximately 50 – 70% of natural organic matter is found as humic and fulvic acids (humic substances), with the remainder being low molecular weight hydrophobic and hydrophilic molecules (Malcolm, 1993). Humic substances are colloidal by nature, and are likely deprotonated at neutral pH, with pKa values between 3.7 and 6.6 in the stronger and weaker acidic groups (Tombacz et al., 2000). This gives the species a net negative charge, and thus more likely to bind to metal cations. NOM, while itself not harmful to human health, is a problematic concern in drinking water treatment because NOM forms suspected carcinogenic disinfection by-products (DBPs) such as tri-halomethanes (THMs) upon contact with typical disinfectants such as chlorine. NOM also absorbs UV light, decreasing effectiveness of UV disinfection, and causes fouling of the membrane during the physical membrane separation process.

1.3.8. Community Focus: Aboriginal Community in Canada

The RES'EAU-WaterNET network of academic and industry specialists has come together to address the concerns of small communities in Canada that have difficulty in accessing a reliable supply of clean and safe drinking water. Indeed, some communities in Canada have been on a boil water advisory for over 10 years, and some require that their drinking water supplies are trucked in. In rural communities, a trained operator is needed to ensure the

proper use of the drinking water treatment plant. This is often very dependent on the technology used to treat the typical water in the community watershed. While clear groundwater from a well may only need UV disinfection followed by small standardized doses of chlorine for secondary disinfection, water containing high concentrations of NOM requires expensive and complicated chemical dosing of coagulants or membrane filtration prone to fouling. There is no current affordable technology to suitably remove NOM, especially in the most remote and smallest communities, some only accessible by airplane. A representative Aboriginal or remote community of several hundred persons in a location with high concentrations of NOM was thus chosen for the community focus of this thesis.

1.3.9. Knowledge Gaps in EC Research

After reviewing the existing scientific literature on the EC process, several key points and knowledge gaps were identified:

i) Due to its robust, economic, and ecologically-friendly nature, EC is particularly suited to treating water sources with fluctuating variability in type and concentration of contaminants, in settings where regular testing and operator input is not available. This makes EC especially suited to rural drinking water treatment, which has not been thoroughly investigated.

ii) While there has been some electrode comparison (Al, Fe, Zn) for waste water, there has been no systematic comparison of electrode materials for drinking water treatment, especially for natural water containing NOM.

iii) A large knowledge gap exists in terms of EC reactor design, even operating parameters are not well defined and differ greatly between researchers. For these reasons, scale-up is mostly empirical and has yet to be successful.

iv) The electrochemical aspect of EC has not been well researched, especially that of the cell potential and current relationship, has yet to be adequately explained or modeled, reducing modeling to empirically-derived constants, and preventing realistic predictions of scaled-up electrical consumption.

v) The investigation on the differing EC species is extremely under researched, with no studies examining speciation systematically or attempting to determine what parameters affect speciation.

This thesis aims to address as many of these research gaps as possible, in hopes of providing a better understanding of the science and application of EC for drinking water treatment.

2. Metal Type and Natural Organic Matter Source for Direct Filtration Electrocoagulation

2.1. Chapter Introduction

Natural organic matter (NOM), a product of broken-down plant and animal matter, is present in natural drinking water reservoirs such as lakes and rivers. NOM has no single structure, rather it is characterized as groups of colloidal species with a typical apparent molecular weight (AMW) of 200-20,000 Da, containing a wide variety of aromatic, carboxylic acid, and phenol groups (Schulten and Schnitzer, 1993), see Figure 2-1. The structure of NOM varies from sample to sample, showing structural heterogeneity, causing difficulty in identifying even 10% of a typical NOM sample (Schmitt-Kopplin et al., 1998).

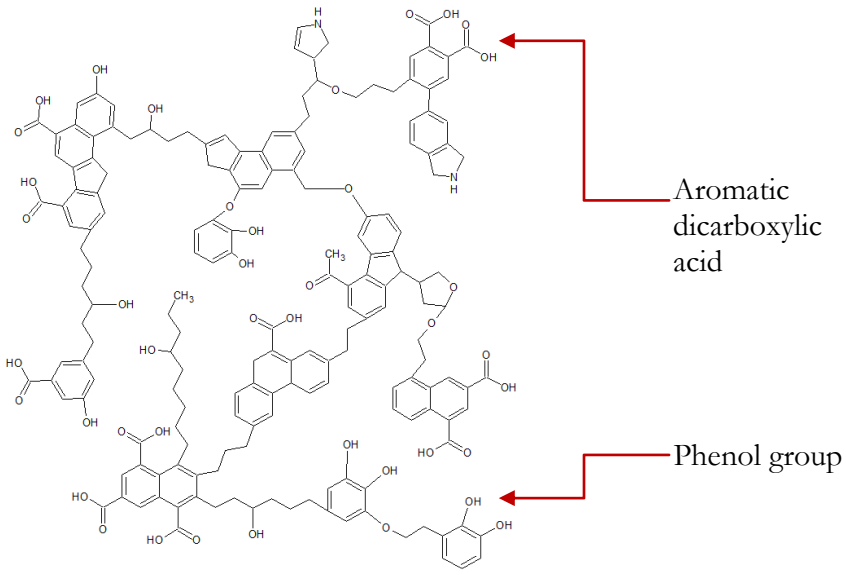

Figure 2-1: A possible structure of NOM

NOM is problematic in drinking water treatment because it leads to the formation of harmful disinfection by-products (DBPs), including suspected carcinogenic substances such as tri-halomethanes (THMs) and haloacetic acids (HAAs) upon contact with chlorine disinfectants, due to Cl substitution into the organic molecule or partial oxidation of NOM. NOM is also known to cause fouling in membranes and to absorb UV radiation, decreasing effectiveness of UV disinfection. For these reasons, NOM should be removed from drinking water prior to disinfection. Coagulation and flocculation is a conventional treatment for NOM removal, where metal chloride or sulfate salts are added to destabilize colloid structures such as NOM (normally a stable colloid that does not settle), decreasing intermolecular repulsion, and inducing agglomeration. USEPA has a guideline removal of 50% dissolved organic carbon (DOC) for low alkalinity waters (USEPA, 1998), but at high initial NOM levels, reducing DOC and UV absorbance to acceptable levels remains a challenge, both technically and economically, with conventional technologies. NOM-impacted waters show high variability in DOC concentration due to seasonal fluctuations (Reckhow et al., 2008), and thus require treatment systems that respond quickly and remotely to demand.

EC is currently applied for wastewater treatment and has been investigated previously for drinking water, but has been held back until recently due to lack of fundamental process understanding and specific drinking water based evidence. EC involves a deceivingly simple infrastructure: a sacrificial metal anode and inert cathode are placed in the water to be treated, and a small amount of electrical current passes between the electrodes. Subsequent

electrochemical metal ion generation and bulk electrolyte coagulant generation in neutral conditions are:

$$\text{Anode: Me } (s) \rightleftharpoons \text{Me}^{z+} (aq) + z\,\text{e}^- \tag{2-1}$$

$$\text{Cathode: } x_w\,\text{H}_2\text{O } (l) + z\,\text{e}^- \rightleftharpoons y_H\,\text{H}_2\,(g) + z\,\text{OH}^-\,(aq) \tag{2-2}$$

$$\text{Electrolyte: Me}^{z+}\,(aq) + z\,\text{OH}^-\,(aq) \rightleftharpoons \text{Me(OH)}_z\,(s) \tag{2-3}$$

where Me can represent any anode metal type, z is the charge transfer number, and x_w and y_H represent the stoichiometric values of reacted water and produced hydrogen, respectively. Cathodic reduction of dissolved oxygen can also take place, but dissolved oxygen effects were not studied here. For NOM removal, Vik et al. (1984) investigated EC for surface waters of 5.9-15.6 mg/L TOC with aluminum electrodes, reducing TOC to 4 mg/L, but found higher residual aluminum than with alum coagulation. Vepsäläinen et al. (2009) similarly used aluminum EC to reduce DOC from 18.35 mg/L to less than 4.50 mg/L, but only 1 out of 30 experiments met American Water Works Association (AWWA) residual aluminum guidelines of 0.05 mg/L. Jiang et al. (2002) compared aluminum EC with alum coagulation for DOC, VIS-abs-420, and UV-abs-254 removal, and consistently found that EC performed better than alum, reducing DOC from 8 mg/L to less than 4 mg/L for the same metal dose. The authors also found that initial pH did not affect DOC removal with EC, while it was essential to alum coagulation. DOC decreased by an addition 25% when adjusted from pH 7.8 to 6.5 due to higher coagulant positive charge, and lower net molecular charge on the NOM compounds at lower pH. Bagga et al. (2008) used Fe EC as a microfiltration pre-treatment in surface water to decrease DOC from 5.6 mg/L to less

than 4.0 mg/L, finding no significant difference between chemical and electrochemical dosing methods. Most studies have used aluminum electrodes for EC drinking water treatment, but application has been hindered due to growth of an anodic passivation layer, which can be removed in wastewater treatment with the addition of chloride salts (Mechelhoff, 2009) due to anodic evolution of chloride containing pitting corrosion promoters. This option, however, is not practical for drinking water.

Relatively few studies investigated iron electrodes for drinking water (Mills, 2000; Bagga et al., 2008; Addy, 2009; van Genucthen et al., 2011), and no reports of zinc electrodes. Aluminum and iron electrodes have been compared previously for various pollutants, with aluminum anodes showing better removal results for arsenic (Koyba et al., 2011), and iron showing better results for COD and BOD (Asselin et al., 2008), and in a different study, iron was superior to aluminum for arsenic removal (Ratna Kumar et al., 2004). The difference seen in pollutant removals highlights the need for further comparison with electrode material in identical EC reactor conditions. Also, several EC studies have investigated the effect of co-occurring solutes (Kim et al., 2002; Shen et al., 2003; Aber et al., 2009; Addy, 2009; Izquierdo et al., 2010). Reports show that chloride increases dissolution efficiency of the anodic material (Kim et al., 2002; Aber et al., 2009), although can also negatively affect EC treatment (Fouad et al, 2009) due to neutralization of Cl^- instead of negatively charged colloid particles. Phosphate has been shown to compete with coagulant sorption capacity and affect mineralogy (Mayer et al., 2000), while carbonate (Villalobos et al., 2000) and calcium (Wilkie et al., 1996) have been shown to compete for sorption sites.

Coagulation and floc growth are typical aspects in a water treatment system, and since mixing promotes particle collisions and floc growth, EC usually requires post-electrolysis flocculation. Flocculation and settling tanks are common place in large scale treatment facilities, but are cost prohibitive for small and rural communities, who are the most likely to be impacted by high and varying NOM source water. While EC is often reported as a "slow" technology, with reactor residence times up to 240 minutes (Holt et al., 2005), the investigation of a direct filtration EC (DFEC) process without major infrastructure, or with optimized and minimal infrastructure, would be of great benefit to these communities. The use of EC with differing NOM sources would also demonstrate the robustness of the technology seasonally and geographically. This chapter focused on evaluating and comparing three different metal anodes in order to determine their efficacy at removing NOM and improving drinking water quality. The effect of EC on NOM structure was assessed by examining changes in AMW distribution by high performance size exclusion chromatography (HPSEC), since changes in MW distribution can lead to changes in DBP formation potential (Buchanan et al., 2005). While HPSEC is a powerful tool for NOM MW characterization (Zhou et al., 2000), it has several limitations, including: detecting only chromophoric NOM (CNOM) species, use of an idealized peak fitting methodology for categorizing MW size fractions, and incomplete understanding of relationship between the actual "size" in Da of the NOM molecule compared to the measured hydrodynamic volume (Grubisic et al., 1967). Still, in combination with DOC and UV-abs-254 characterization, HPSEC gives better insight into the behaviour and removal abilities of EC. In general, EC makes an excellent candidate to meet the challenges for fast and low-cost NOM removal,

but the significant research gaps still exist in systematically looking at anode metal types, NOM sources, and influent water conditions, which was the objective of this chapter's work.

2.2. Materials and Methods

2.2.1. Operating Variables of Interest

Three anode metal types were selected: iron, aluminum, and zinc, the three most ubiquitous and inexpensive metals capable of electrochemical dissolution and formation of charged metal oxide and hydroxide species. Three NOM sources were selected to investigate the range of applicability: Suwannee River (Georgia, USA) NOM reverse osmosis (RO) isolate, a Nordic Reservoir (Vallsjøen, Norway) NOM isolate from the International Humic Substances Society (Denver, Colorado, USA) and a local source in British Columbia (Lost Lagoon, Vancouver, Canada). Two initial NOM concentrations (13.79 mg/L and 21.59 mg/L DOC) were selected to investigate the capability of EC of treating peak needs and seasonal fluctuations. Four common solutes (carbonate, calcium, phosphate, and chloride) were selected in two concentrations: a lower concentration typical of natural water, and a higher one indicative of spike effects. Charge loading (*CL*), sometimes referred to as charge density, was the common independent variable in most experiments, measured as Coulombs/L [C/L], but can be reported as time with a constant current, or metal loading if Faraday's Law applies and current efficiency is known. *CL* was generally reported as time [min] in order to show the speed of the process.

2.2.2. Synthetic and Natural Water

The synthetic water was composed of Milli-Q deionized water, with standardized NOM isolate produced by reverse osmosis (RO) (Suwannee River and Nordic Reservoir standards). Na_2CO_3, $CaSO_4$, Na_2HPO_4 (Laboratory Grade, Fisher Scientific) were added, well mixed, and filtered to 0.45 μm to target only dissolved NOM species. The addition of 30 mg/L NOM RO-isolate gave DOC concentrations of approximately 12 mg/L after filtration. Batches were made as needed, and stored at 5°C. Conductivity was enhanced in synthetic waters with the addition of 150 mg/L Na_2SO_4 (Laboratory Grade, Fisher Scientific), chosen for its electrochemical inertness (Bard and Faulkner, 1980), to a nominal value of ~300 μS/cm. Solution pH was adjusted before DOC analysis by NaOH or H_2SO_4 (Laboratory Grade, Fisher Scientific) to attain a pH of 7.00 ± 0.05. Natural local water was collected from Lost Lagoon, Stanley Park, Vancouver, Canada as representative poor quality and high DOC source water typical of rural community drinking water sources. The local water was collected in June 2011, with no further filtration, pH adjustment, solute addition, or disinfection, and stored at 5°C. Relevant characteristics were: DOC_0=13.31 mg/L, $SUVA_0$=4.21, κ=990 μS/cm, and alkalinity = 28 mg/L $CaCO_3$. All waters were allowed to equilibrate to room temperature, and were at 20 ± 1 °C during experiments. Error analysis of duplicate batches of synthetic water showed high repeatability in initial DOC concentration (*RSE*=2.3%) and UV-abs-254 (*RSE*=1.4%). Local water collection occurred only once, and hence had no relative standard error.

2.2.3. Analytical Methods

TOC concentration was determined by a UV/persulfate oxidation TOC analyzer (Shimadzu TOC-VCPH). Temperature, pH (Denver Instruments ATC UB-10), and conductivity (YSI-3200) were continuously monitored. Absorbance measurements were determined using a UV-Vis spectrophotometer (Shimadzu UV-mini 1240) with a cell path of 1 cm. Specific UV absorbance (SUVA) was calculated as (UV-abs-254 × 100)/DOC in L/mg-m. Residual metal concentration was measured by inductively coupled plasma optical emission spectroscopy (ICP-OES) with wavelengths: iron - 238.204 nm; aluminum - 396.153 nm; zinc - 206.200 nm (PerkinElmer Optima 7300 DV).

For HPSEC analysis, 100 μL samples were filtered to 0.45 μm, and injected into a high performance liquid chromatography (HPLC) system (Waters 2696 Separation Module, Waters 2487 dual λ absorbance detector at 260 nm, Waters Protein-Pak 125 Å column). Column retention time was calibrated to AMW using the method of Pelekani et al. (1999) with polysulfonate standards (7 kDa PSS7K, 4 kDa PSS4K, 2 kDa, PSS2K, American Polymer Standards Corporation) and 1 g/L acetone (certified A.C.S., Fisher Scientific). The carrier eluent was 0.05 M acetate buffer (Laboratory grade, Fisher Scientific) with a column flow rate of 0.7 mL/min. HPSEC chromatograms were deconvoluted and resolved using Systat Peakfit v4.12 as described by Sarathy and Mohseni (2007). Parameters were Gaussian response widths of 20 s, a frequency domain filter of 60%, and an amplitude rejection threshold of 3%, leading to $R^2 > 0.97$ for all fitted chromatograms. Fitted peak areas were normalized over total peak area, representing total CNOM (Sarathy and Mohseni, 2007), and

grouped into chromophoric NOM (CNOM) AMW fraction categories: <550 Da, 550-750 Da, 750-950 Da, 950-1200 Da, 1200-1450 Da, >1450 Da. All experiments in this chapter were performed twice, with error bars in all figures representing standard error.

2.2.4. Electrocoagulation

A custom 60 mL, high surface area, batch electrolysis chamber was manufactured from inert acrylic. Twelve custom electrodes were utilized in monopolar connection, six anodes and six cathodes, each with a nominal surface area of 18.65 cm^2 on each side, and an inter-electrode gap of 2 mm, see Figure 2-2.

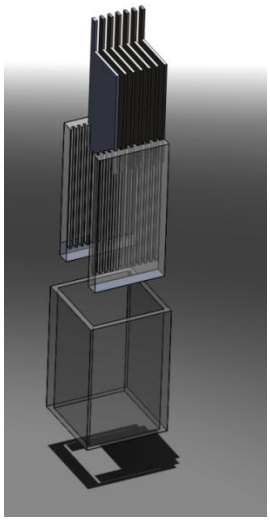

Figure 2-2: Batch reactor with electrode array

Each electrode was completely submerged in the solution, allowing for complete utilization of the electro-active surface area, and maintained electrical contact with an un-submerged

copper bus bar. The electrodes were maintained perfectly parallel by machined spacers, giving an overall electrode surface area to volume (SAV) of 0.34 m^2/L. The electrode metal grades (McMaster-Carr) were: zinc, EN988; aluminum, 5052; iron, 1018; and cathode, 304 stainless steel. A DC power supply (GW Instek PSP-2010) supplied DC current in galvonostatic mode, connected to a PC by RS-232 connection. Electrodes were washed with de-ionized Milli-Q water, wet-polished with P1500 SiC paper, rinsed with 2% sulphuric acid, and double rinsed with Milli-Q water. Electrolysis took place directly after polishing to avoid surface films or auto-dissolution. After electrolysis, the electrodes were removed, and the system was immediately filtered on a new 0.45 μm PTFE membrane filter for analysis. All analytical measurements were performed within 2 hours of each experiment, and all experiments were performed in duplicate, or in some cases, triplicate. The relationship between *CL* and metal loading (*ML*) is described by Faraday's Law in equation (2-4):

$$ML = \frac{\varphi \cdot CL \cdot MW}{z \cdot F} \tag{2-4}$$

where φ is the current efficiency, MW is the molecular weight of the metal type, z=3 for aluminum, 2 for zinc, and 2 for iron (Lakshmanan et al., 2009; Sasson et al., 2009), and *F* is Faraday's constant (96,485 C/mol·e^-). The value for φ was determined by linear regression of experimental metal dissolution, determined by ICP-OES, and varied between 0.8-1.05 depending on metal/water/solute combination. Taking into account the systematic error of

all instrumentation, σ_x was estimated at 2%. Since the purpose of the experiments in this chapter was not to optimize metal dose nor control for φ as in later chapters, φ was assumed to be unity for all metal and solute combinations. For example, 30 seconds of EC at 0.50 A with aluminum anodes in this study gave a *CL* of 250 C/L and a *ML* of 23.3 mg Al/L.

2.3. Results and Discussion

2.3.1. Effect of Anode Metal Type

NOM removal for the three different metal anodes showed sufficient DOC removal to meet the USEPA target reductions of 50% with 30 seconds process time (Figure 2-3). The best short term performance was obtained with the iron anode, the rate of DOC reduction after 15 sec was 0.40 mg-DOC/sec, with 0.32 mg-DOC/sec and 0.18 mg-DOC/sec for zinc and aluminum, respectively. After one minute of electrolysis, DOC reduction reached a lower plateau at approximately 70% reduction for all metals, with iron showing marginally better removal at one and two minutes electrolysis time, and essentially the same (>95% confidence using Student's t-test) removal with all electrodes was observed after three minutes of electrolysis.

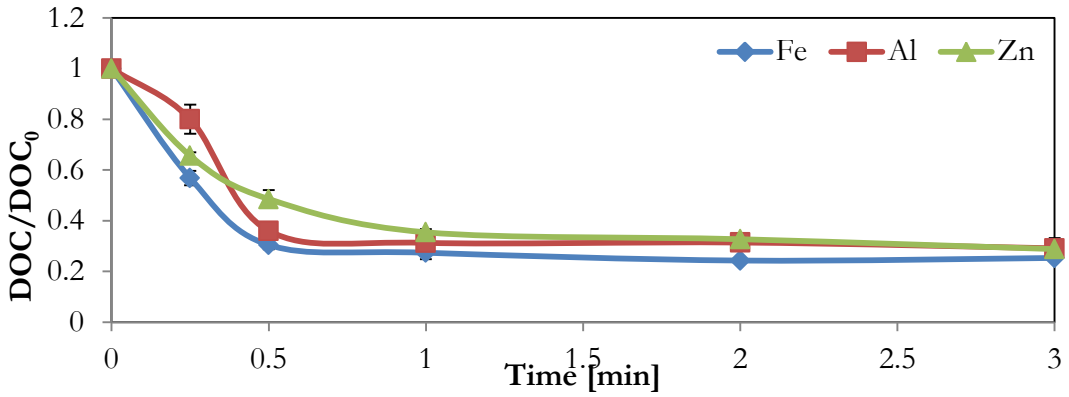

Figure 2-3: NOM removal with different metal anodes. NOM = Suwannee, DOC_0=13.79 mg/L, I=0.5 A, i=2.43 mA/cm^2, Electrolyte= Na_2SO_4, $E_{cell} \approx$ 2.6 V.

Further electrolysis of up to 5 minutes indicated that the DOC removal beyond one minute reached steady-state, after which further electrolysis led to no additional decrease in DOC, nor did extended EC display increases in DOC, as seen with overdosed chemical coagulants (van Leeuwen et al., 2005). The UV-abs-254 reduction data showed the three metals performed similarly, shown in Figure 2-4.

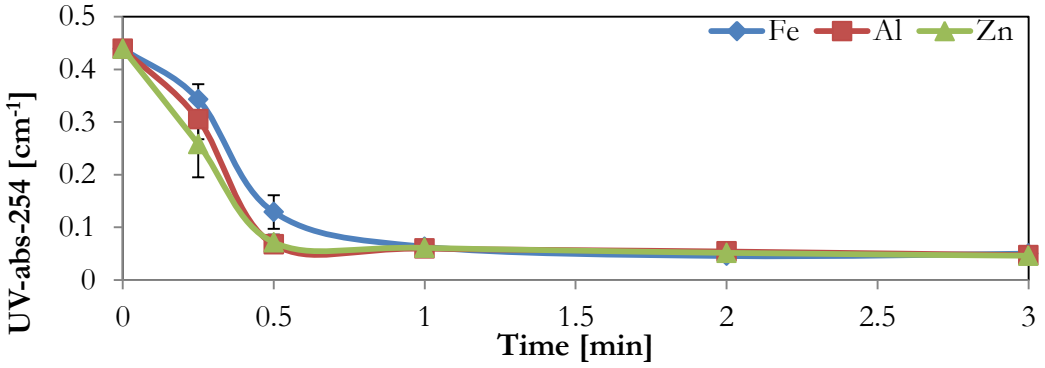

Figure 2-4: UV-abs-254 reduction with different anode metal types. NOM = Suwannee, DOC_0=13.79 mg/L, i=2.43 mA/cm^2, Electrolyte= Na_2SO_4

The best short term performance in UV-abs-254 removal was achieved with the zinc anode, the rate of reduction was 0.012 cm^{-1}/sec, with 0.008 cm^{-1}/sec and 0.006 cm^{-1}/sec for aluminum and iron, respectively. For longer term performance, all metals performed equally well after 1 min of electrolysis (>99% confidence using Student's t-test), reducing UV-abs-254 to approximately 0.06 cm^{-1}, over 85% reduction. Further electrolysis greater than 3 minutes showed no further reductions in UV-abs-254, with a steady state minimum of approximately 0.05 cm^{-1}, or 88.6% reduction. The only difference between metals in terms of UV-abs-254, was higher UV absorption by the iron coagulant in the first 30 seconds of electrolysis. This difference was likely seen because of the UV absorbing orange colour produced by iron EC particles; at smaller doses the iron did not flocculate enough before filtration, imparting a subtle orange tint to the water.

A sharp drop could be seen in both DOC and UV-abs-254 after an initial dosing period, usually 30 seconds. The drop region can be defined as the "reactive" stage of the three proposed stages of EC pollutant removal: the "lag" stage, "reactive" stage, and "stabilising" stage (Holt et al., 2005). The "lag" stage was not observed likely due to the higher rate of coagulant generation in the current investigation. The reactive stage only lasted in a range of 15 seconds to 1 minute electrolysis time, much shorter than the 15 minutes or more reported elsewhere (Holt et al., 2005; Addy, 2009). Total process time was 40 times faster for similar pollutant removal as shown by Holt et al. (2005), suggesting that EC need not be a slow dosing process as typically represented. The fast electrolysis time reported here was only economically feasible at low voltages (under 5.0 V for these parameters), the high SAV and low inter-electrode gap allowed this with reduced electrolyte ohmic resistance. When

electrode area was reduced, cell operating voltage exceeded 20V, leading to excessive joule heating of the solution, likely rendering the process infeasible.

Cell voltage growth was observed only for the aluminum anode, where cell voltages grew to as high as 7.0 V for 3 minutes of electrolysis, the passivation layer on the aluminum anode could only be removed by polishing or chloride addition as elsewhere (Mechelhoff, 2009), which brought cell voltage to initial levels. Iron showed no passivation or voltage increase as seen elsewhere (Addy, 2009), zinc also showed no immediate passivation. Iron showed marginally higher DOC removal, consistent with other anode metal comparison studies for both organic (Asselin et al., 2008) and inorganic (Ratna Kumar et al., 2004) pollutants. A temporary pH increase due to EC hydroxide generation was seen for all sources and all metals, with an increase of 0.5 units for lower dose (<1 min) and a maximum increase of 3.5 units for 3 minutes. The pH decreased back to approximately pH~8 after several minutes of equilibration.

2.3.2. Effect of NOM Source

EC reduced DOC for all three types of NOM sources tested (Suwannee, Nordic, and Local), again greatly exceeding 50% target reduction for all three NOM sources (Table 2-1):

Table 2-1: DOC and UV-abs-254 removal with different NOM sources. *n*=2, *i*=2.43 mA/cm^2, Electrolysis time = 1 min, Electrolyte= Na_2SO_4 (Suwannee, Nordic) Electrolyte = none (Local)

	Suwannee	*Nordic*	*Local*
DOC_0 [mg/L]	13.79	9.03	13.31
UV-abs-254_0 [cm^{-1}]	0.439	0.315	0.560
$SUVA_0$	3.18	3.48	4.21
Iron			
$DOC_{treated}$ [mg/L]	3.77	3.19	2.26
DOC removal %	72.6	64.7	83.0
UV-abs-$254_{treated}$ [cm^{-1}]	0.063	0.044	0.077
UV-abs-254 removal %	85.6	86.0	86.3
$SUVA_{treated}$	1.67	1.38	3.40
Aluminum			
$DOC_{treated}$ [mg/L]	4.31	4.13	3.96
DOC removal %	68.7	54.2	70.2
UV-abs-$254_{treated}$ [cm^{-1}]	0.060	0.046	0.043
UV-abs-254 removal %	86.3	85.4	92.3
$SUVA_{treated}$	1.39	1.11	1.08
Zinc			
$DOC_{treated}$ [mg/L]	4.89	4.04	2.13
DOC removal %	64.5	55.2	84.0
UV-abs-$254_{treated}$ [cm^{-1}]	0.069	0.051	0.038
UV-abs-254 removal %	84.2	83.8	93.2
$SUVA_{treated}$	1.41	1.26	1.78

Averaged between all NOM sources, iron performed slightly better than the aluminum or zinc for DOC removal, and aluminum generally showed the lowest UV-abs-254. Nordic NOM isolate was the most resistant to EC treatment, with aluminum and zinc barely surpassing the DOC removal guideline at 54.2% and 55.2% removal, respectively. SUVA values decreased from 3.2-4.2 L/(m·mg) to less than 2.0 in all cases except for the iron

anode in the natural NOM source water, where effluent SUVA was 3.4. Initial SUVA values in this range suggest a more hydrophobic dissolved carbon species (Edzwald, 1994), containing aquatic humic material of high MW, more likely to be effectively removed by coagulation. SUVA values of less than 3 generally indicate a low MW hydrophilic dissolved carbon, which has lower charge density (Edzwald, 1994), thus only slightly affected by coagulation. Treated waters for all metals and NOM sources generally showed a SUVA below 1.75, indicating the efficacy of the EC process at removing high MW fractions of the NOM, and also a stop point for EC's effectiveness for additional DOC removal. The hydrophilic DOC components may have formed bonds with the hydroxyl groups on hydrolyzed metal complexes, facilitating some coagulation, although likely not enough to remove the bulk of hydrophilic DOC. The fraction of NOM removed by EC is thus predominantly the large hydrophobic and high MW fraction of NOM, seen similarly in chemical coagulation studies (Amy, 1993; Randtke, 1993). The higher SUVA value of 3.4 in the iron-natural combination was likely due to the low residual DOC and the slightly higher UV-abs-254 of iron, rather than a difference in hydrophobic or hydrophilic NOM behaviour in the treated solution. The AMW distribution of the recalcitrant NOM post electrolysis was determined by HPSEC, results for Suwannee NOM are shown in Figure 2-5.

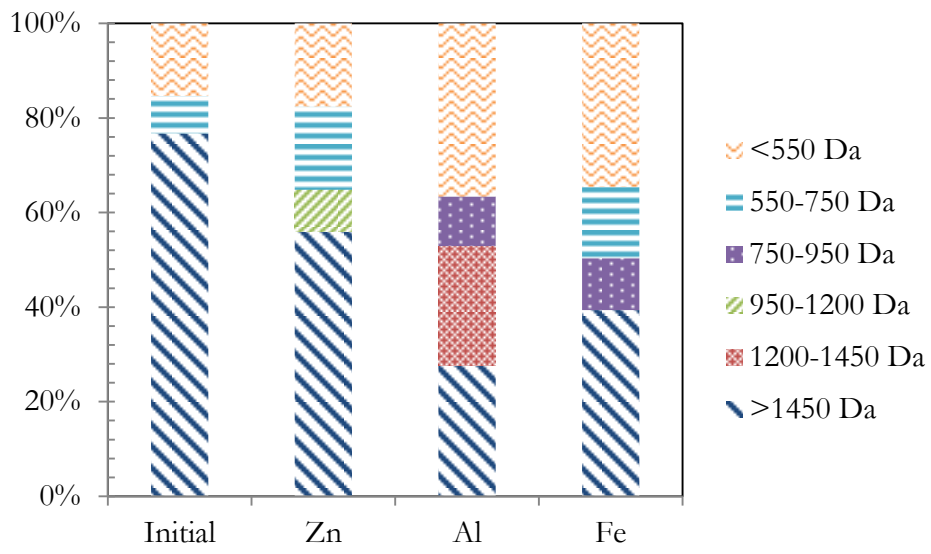

Figure 2-5: HPSEC molecular size distribution for Suwannee NOM and three metal types. NOM = Suwannee, DOC_0=13.79 mg/L, i=2.43 mA/cm^2, t=2 min, Electrolyte= Na_2SO_4

A similar MW Suwannee River was found as elsewhere, in accordance with reports of average MW of 1910 Da (Beckett et al., 1997) and 1700 Da (Chin et al., 1991). Reductions were from an initial of 76% DOC > 1450 Da to an average of 40% DOC > 1450 Da for the post electrolysis recalcitrant fraction for all metals and Suwannee NOM. HPSEC results had high repeatability between different samples (*RSE*=1.8%). These results quantitatively demonstrated that EC preferentially removed the higher MW fraction of NOM, confirming SUVA results. For Suwannee NOM, aluminum anodes decreased the fraction of large (>1450 Da) NOM species greater than iron or zinc anodes, following findings of post-EC SUVA values, where residual SUVA values of aluminum were lower than zinc and iron for Suwannee NOM. However, since Fe EC removed greater total DOC, this finding suggests

that Fe better removed intermediate size DOM fractions (550-950 Da), and to a greater total extent than Al. . This may be explained by the increased molar mass/z ratio of Fe (27.9) compared to Al (9.0), allowing Fe to target more DOC, even when Al better removes the larger fractions. Some studies have shown that Fe salts better remove the larger DOM fraction than alum (Matilainen et al., 2005), although this was found at a lower optimum pH (pH=5) for iron salt coagulation, while pH was not optimized or controlled in the current study. Other than coagulation, electro-oxidation (or electro-reduction) was considered as a mechanism for reduction in AMW size, as has been previously investigated (Kim, 2006). However, when the sacrificial anodes were replaced with inert stainless steel, HPSEC chromatograms demonstrated no reduction in AMW size, suggesting negligible NOM electro-oxidation mechanisms.

HPSEC results for Nordic and Natural NOM sources are shown in Figure 2-6. Nordic NOM showed a lower initial fraction of high MW species than Suwannee or Natural NOM sources, in accordance with less total DOC removal for Nordic NOM. HPSEC findings also corresponded with post-EC SUVA values for Nordic NOM, where aluminum had both the lowest SUVA and the greatest reduction of large MW NOM, followed by zinc, and then iron. Natural NOM showed the highest fraction of large MW NOM species (>1450 Da), explaining the highest total DOC reduction between the three NOM sources. This also explains the greatest UV-abs-254 reduction with natural water. The recalcitrant fraction had a larger fraction of large MW (>1450 Da) NOM species than the other NOM sources, suggesting either a more difficult to remove large MW NOM species, or that EC may be further utilized with greater dose or flocculation for greater DOC removal. Natural NOM

also compared well to chemical coagulation for iron EC, results for this are shown in Appendix B.

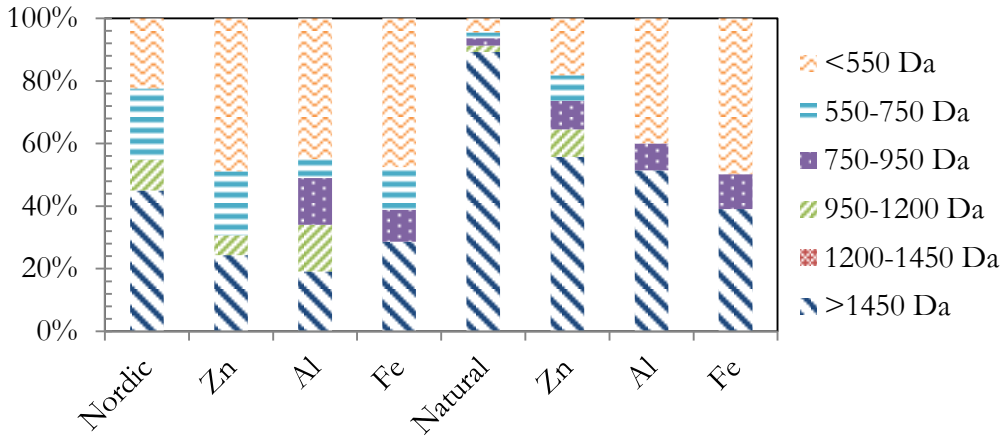

Figure 2-6: HPSEC molecular size distribution for Nordic and Natural NOM Sources with three metal types. i=2.43 mA/cm^2, t=2 min, Electrolyte= Na_2SO_4

Residual metal was analyzed for the three NOM sources and three metal types. Values were compared with 2010 guidance values from the Canadian Drinking Water Quality (CDWQ) guidelines (CDW, 1998), which were: aluminum (0.1 mg/L), iron (0.3 mg/L), and zinc (5 mg/L). Table 2-2 shows average residual metal concentrations for NOM-metal pairs. Aluminum was greatly above both the USEPA guideline (USEPA, 1999) of 0.05 mg/L and the CDWQ guideline of 0.1 mg/L, with a general trend of higher residual aluminum than iron or zinc regardless of NOM source, with similar residual aluminum to previous studies (Vepsäläinen et al., 2009). This may have been due to the different type of floc formation

seen in EC than chemical coagulation (CC) (Holt et al., 2005) the higher solubility of $Al(OH)_3$ ($K_{sp}=3.0 \times 10^{-34}$) than $Fe(OH)_3$ ($Ksp=2.8 \times 10^{-39}$), or due to the smaller aluminum floc size as seen in chemical coagulation studies (Li et al., 2006; Wang et al., 2009) allowing small flocs to pass through the filter. Zinc and iron residuals were well within the CDWQ guidelines, regardless of NOM source. The natural NOM source had the lowest residual metal for all metals, likely due to a NOM species with a lower affinity for metal chelation – possibly in part due to the larger MW species of the natural NOM with less binding sites per molecule. ICP-MS repeatability between samples was moderate (Suwannee *RSE* =7.6% for iron, 6.3% for aluminum, and 8.5% for zinc), likely since the liquids/solids mixture was not completely homogenous upon aliquot sampling.

Table 2-2: Average residual metal concentrations with different NOM sources and anode metal types. n=2, i=2.43 mA/cm^2, t = 1 min

	Suwannee	*Nordic*	*Natural*
Fe EC -Residual Fe [mg/L]	0.088	0.114	0.073
Al EC - Residual Al [mg/L]	0.221	0.344	0.154
Zn EC - Residual Zn [mg/L]	0.143	0.327	0.046

2.3.3. Effect of Initial NOM Concentration

EC achieved DOC removal of greater than 50% for two different initial concentrations of DOC (Figure 2-7 - only iron anode and Suwannee NOM shown). There was a certain percentage of DOC unaffected by EC, regardless of initial DOC concentration or coagulant dose. In the case of Suwannee NOM isolate, the fraction of unaffected DOC was approximately 25%, similar to recalcitrant fractions seen in chemical coagulation (van

Leeuwen et al., 2005), showing the same *relative* DOC remaining regardless of initial NOM concentration. UV-abs-254 reduction was accordingly reduced by a relative amount, approximately 89% for either initial DOC concentration. SUVA decreased from 3.18 to 1.34 and 2.84 to 1.06 for initial DOC values of 13.79 mg/L and 21.59 mg/L, respectively. The SUVA decreased approximately 60% in either case, suggesting a maximum SUVA reduction for differing initial Suwannee DOC concentrations.

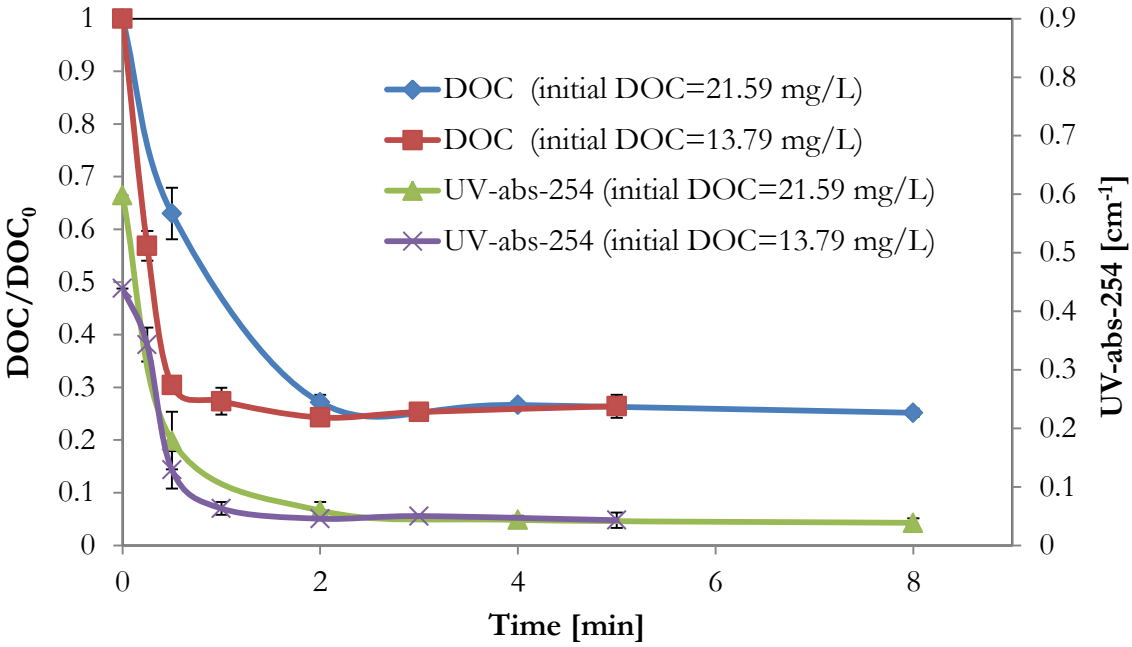

Figure 2-7: DOC and UV-abs-254 reduction with increased initial concentration of NOM. NOM = Suwannee, Metal=iron, *I*=0.5 A, *i*=2.43 mA/cm^2, Electrolyte= Na_2SO_4

HPSEC analysis showed similar molecular size distributions of initial and post-EC NOM fractions at both NOM concentrations (Figure 2-8). Post-EC fractions of larger NOM molecules (>1450 Da) were almost identical (39%), and distributions of 550-750 Da and 750-950 Da were very similar, regardless of initial DOC concentration. AMW fractionation

findings suggest that EC performs equally well for differing initial NOM concentrations for percentage removal of the differing NOM fractions, and that there remains a certain percentage of DOC that is unaffected by EC. This finding has two implications. First, after two minutes of electrolysis, EC was equally effective for initial DOC concentrations between 13-22 mg/L, showing robust process behaviour for fluctuating water conditions of variable DOC concentrations, which is the case in many rural and remote communities with varying source water quality. However, the downside of this finding is likely overdosing at lower DOC concentrations. The second implication is that if a water treatment system enforced a *total* DOC concentration limit (e.g., less than 4.0 mg/L DOC), EC as a standalone process may not successfully treat raw waters extremely affected by NOM (>20 mg/L DOC).

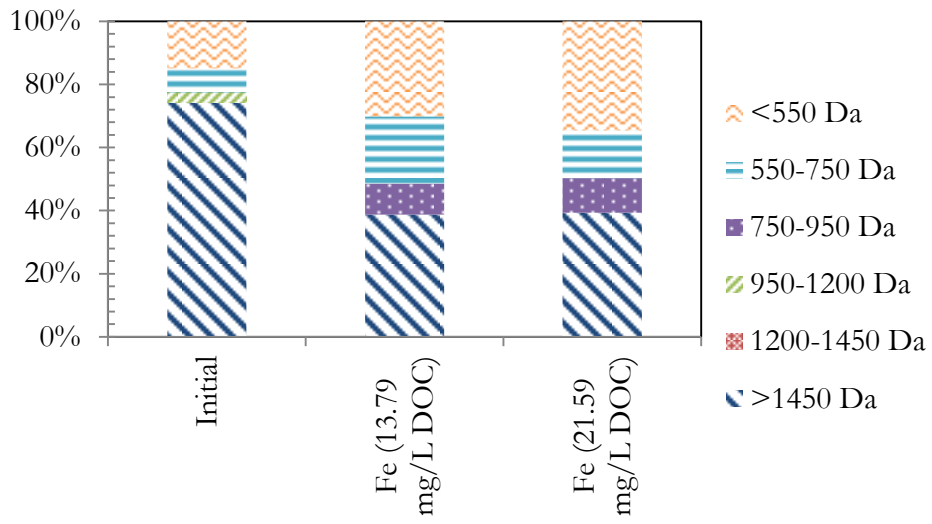

Figure 2-8: HPSEC molecular size distribution for different initial NOM concentrations. NOM = Suwannee, i=2.43 mA/cm^2, Electrolyte= Na_2SO_4

2.3.4. Effect of Co-occurring Solutes

Four solutes (carbonate, calcium, phosphate, and chloride) dosed as Na_2CO_3, $CaSO_4$, Na_2HPO_4, and NaCl, were compared, shown in Figure 2-9 (only iron anode and Suwannee NOM shown). Each solute was added in addition to the 150 mg/L Na_2SO_4 needed for conductivity enhancement. EC removal performance was not extremely affected by any of these solutes, except for higher carbonate concentrations of 200 mg/L, which caused effluent DOC and UV-abs-254 to be twice as high as without carbonate. Carbonate has been seen to negatively affect EC (Vasudevan et al., 2009), and was suggested to increase the formation of an anodic passivation layer, which was likely the case in this chapter's experiments. Calcium increased coagulation efficiency compared to the baseline, which has also been reported elsewhere for EC (Shen et al., 2003), and benefits of calcium have been discussed for chemical coagulation (Van Benschoten, 1990). Correspondingly, total alkalinity was shown to only marginally increase EC pollutant removal efficiency (Zhao et al., 2009), likely due to the fact that alkalinity is generated *in-situ* in EC. Phosphate did not have as detrimental effect as expected from previous EC studies (Moreno-Casillas et al., 2007), where milky colloid residuals were formed, although concentrations tested here were lower. Chloride did not affect the DOC or UV-abs-254 removal greatly, but decreased galvanostatic cell voltage by 1.5 V (to 3.5 V total), likely due to anodic chlorine evolution and subsequent pitting corrosion with less associated ohmic potential loss. Aluminum and zinc electrodes followed similar trends with the same solutes.

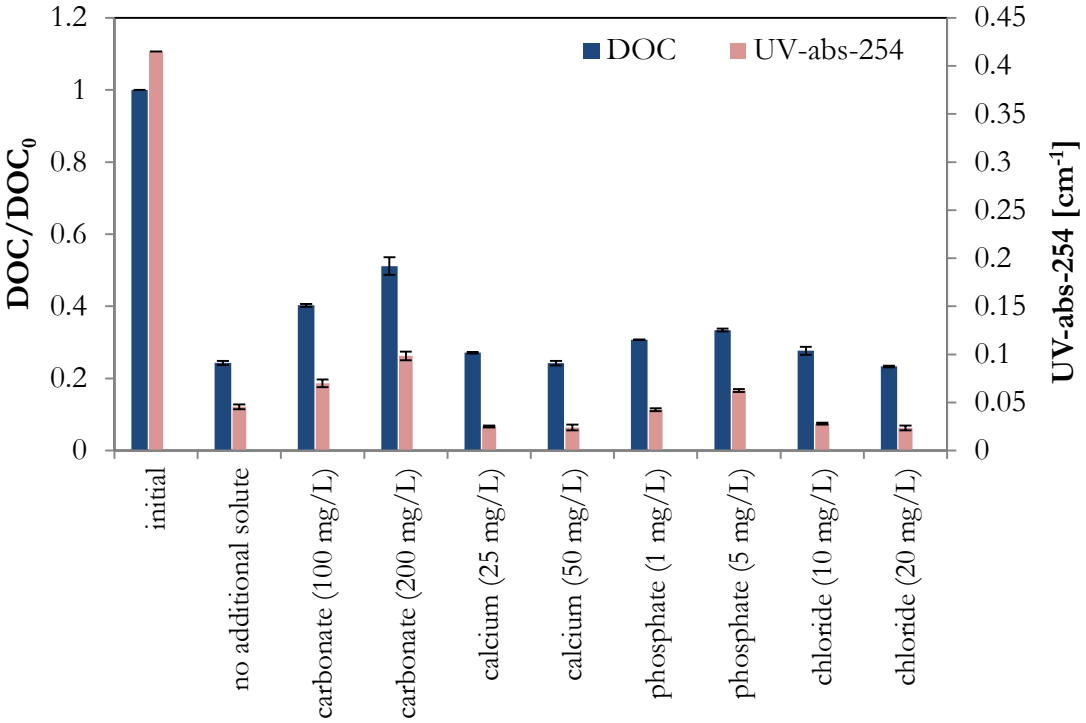

Figure 2-9: DOC and UV-abs-254 removal with different initial electrolyte solutes. NOM = Suwannee, DOC_0=13.79 mg/L, Metal=iron, I=0.5 A, i=2.43 mA/cm^2, t=2 min

Interestingly, after 2 hours post-EC with the iron anode and chloride solute, the UV-abs-254 of the filtered effluent increased to approximately 0.12 cm^{-1}. This was likely dissolved Fe^{2+} which passed through the 0.45 μm membrane and was oxidized by air to the more insoluble Fe^{3+} form, as $Fe(OH)_2$ is 5 orders of magnitude more soluble than $Fe(OH)_3$, as seen in other EC reports (Sasson and Adin, 2010). This could be detrimental to full-scale operation if soluble iron species are not fully oxidized to insoluble ones, as the water could appear deceivingly clear, as previously reported for iron coagulants (Sarin et al., 2004), and iron EC with chloride present should be monitored accordingly, or further oxidized by external

aeration or electro-oxidized. No additional filter fouling was seen with chloride present, filter fouling with all metal types caused a flux decline as expected, comparable to CC.

2.4. Chapter Conclusions

In this chapter, EC was shown to be a viable process for NOM impacted drinking water treatment, meeting 50% removal guidelines for a variety of NOM source waters and solute impacts, providing colourless and potable water without the addition of salts or pH control. Several conclusions can be made from results from this chapter's work:

- Between the three metals tested, iron was the least costly and most available material, it presented greater DOC removal, it showed no passivation layer and linear voltage ramp, and residual metal met guideline values. The iron waste stream also has less disposal issues than zinc, which may require special processing. Iron is recommended for future work.
- While metal doses were higher in this study compared to other EC studies for the removal of NOM, this chapter shows a compact and timely process of less than one minute total treatment time, without requiring flocculation or sedimentation steps. This "fast" EC may appeal to small and rural community water treatment facilities requiring minimal capital expenditure and reliance on supply chains, where iron anodes may be fabricated on site.

3. Iron Electrocoagulation Reactor Design Parameters for NOM Removal

3.1. Chapter Introduction

Decreasing both metal use and electrical consumption in EC is of paramount importance for it to favourably compare to CC in a life-cycle assessment (LCA) as a "green" chemistry process. Operating parameter optimization is thus key to EC's success. The major disadvantage of EC compared to chemical coagulation (usually ferric or aluminum chloride/sulfate) is that electricity is required. This fact is especially relevant for drinking water treatment, as conductivity cannot be enhanced by salts due to total dissolved solids (TDS) limitations in drinking water, necessitating proper design to minimize electrical consumption. While chemical coagulation has an accepted and time-tested design methodology, EC reactor design has had no such consensus. Fundamentally, EC design requires electrochemically generating a solid-state coagulant in a manner that allows appropriate pollutant-coagulant contact and minimizes both metal consumption and electrical consumption. In some cases, EC designers also wish to harness the electrolytic bubble generation for an EC-flotation process. Electrode configurations vary widely, with most studies using parallel plate electrodes, while cylinders, tubes, perforated plates, and fluidized reactors have shown no significant advantage (Mollah et al., 2001). Even among parallel plate studies, there appears to be no consistent experimental approach among studies, limiting comparability of the results and refinement of EC. EC has thus been left to industry as "trial and error" engineering as noted elsewhere (Holt et al., 2005), leading to

great frustrations among EC developers and researchers. In terms of EC design for drinking water, it is certain that EC will require a large electrode surface area to reduce ohmic voltage loss, recalling that salt addition is not a practical option. Electro-flotation is likewise not practical for drinking water treatment, as the large surface area significantly reduces electrolytic bubble flux (Holt et al., 2005). Thus, parallel plate designs are likely to dominate reactor designs for drinking water, with associated key operating parameters required greater definition and evaluation.

Several parameters have been investigated *individually* in parallel plate EC reactor design, including: current density (*i*) (Chen et al., 2000; Larue et al., 2003; Holt et al., 2005; Golder et al., 2007; Zhu et al., 2007; Mouedhen et al., 2008; Addy, 2009), coagulant dosing rate (Holt et al., 2005; Addy, 2009), and flocculation strategy (Pouet and Grasmick, 1994; Jiang et al., 2002; Bagga et al., 2008), although a complete multi-variable investigation into these reactor design parameters has not yet been reported. Differences in *i* greatly affect the overall reactor footprint due to the electrode area, and total power consumption due to ohmic voltage drop. Increasing electrode surface area decreases *i*, which has generally shown better pollutant removal (Holt et al., 2005; Zhu et al., 2007; Mouedhen et al., 2008; Addy, 2009). The charge loading rate (*CLR*) [C/L/min], or dosing rate [mg/L/min], is defined here as the rate of coagulant generation standardized by the solution volume. This is a unique property of EC compared to chemical coagulation (CC), since a slow "release" of coagulant is possible electrochemically, possibly allowing less overall coagulant use, while the dose in CC is effectively immediately dosed and mixed. *CLR* can either be expressed in units of [C/L/min], or [A/L], but [C/L/min] was chosen to better relate to the metal dose (*CL*)

measured in [C/L]. The flocculation strategy for EC generally falls into one of two categories: a "slow" process with a low *CLR*, long flocculation times, and reactor residence times up to 4 hours (Holt et al., 2005; Addy, 2009), and a "fast" process with a higher *CLR*, little or no flocculation, and reactor residence times as low as 15 s, as seen in Chapter 2.

NOM was again the focus of this chapter, and EC has been investigated previously for its removal (Vik et al., 1984; Jiang et al., 2002; Vepsäläinen et al., 2009); however, these studies use aluminum anodes, and residual metal concentrations have generally exceeded the AWWA guideline limits of 0.05 mg/L which was also seen in Chapter 2. Previously, iron EC showed marginally greater DOC and UV-abs-254 reduction in a direct filtration EC unit compared to aluminum or zinc EC (Chapter 2), and has shown to be advantageous to chemical coagulation in surface water pre-treatment (Bagga et al., 2008). Iron EC has also shown 4-log *E.coli* disinfection (Mills, 2000), and 4-log MS2 bacteriophage virus inactivation (Zhu et al., 2005). However, EC reactor design has never been investigated for NOM removal, thus, iron EC was further investigated in this chapter with regards to *i*, *CLR*, pH adjustment, and mode of operation. Investigating and optimizing iron EC with regards to metal and electrical consumption at these differing parameters was thus the focus of this chapter's work.

3.2. Materials and Methods

3.2.1. Operating Variables of Interest

Five current densities in the range of 2.43 to 26.8 mA/cm^2 were compared, while maintaining the same total current by scaling electrode surface area. To be clear, *i* is defined in this chapter as the total current (*I*) divided by the nominal electro-active anode surface area (*A*). Five *CLR* values in the range of 100 to 1000 Coulombs/L/min [C/L/min] were selected to determine the impact of coagulant addition rate, while maintaining a constant *i* by scaling electrode area. For example, a charge loading of 200 C/L is delivered in 2 and 0.2 minutes for a *CLR* of 100 and 1000 C/L/min, respectively. Two dosing and flocculation modes, "slow" and "fast" were compared to determine the effect of pollutant-coagulant contact time and overall process time. The "fast" mode was a high *CLR* (500 C/L/min) where the coagulant was dosed effectively immediately without *in-situ* flocculation, used elsewhere in on-demand EC applications in wastewater (Weintraub et al., 1983; Sanfan, 1991) and previously in Chapter 2. The "slow" mode was a slower *CLR* (100 C/L/min) where flocculation took place *in-situ*, a treatment methodology typical of conventional water treatment facilities and utilized in some EC studies (Holt et al., 2002; Addy, 2009). For pH adjustment, NaOH or H_2SO_4 (Laboratory Grade, Fisher Scientific) was added immediately after electrolysis until the desired pH value was attained.

3.2.2. Synthetic Water

Synthetic water was composed of Milli-Q deionized water and standardized NOM isolate (Suwannee River RO standard, International Humic Substances Society). Conductivity was increased to a nominal value of ~300 μS/cm, typical of surface waters, attained by the addition of 150 mg/L Na_2SO_4 (Laboratory Grade, Fisher Scientific). In several separate tests 150 mg/L NaCl (Laboratory Grade, Fisher Scientific) was used instead. The solution was well mixed, and filtered to 0.45 μm on a new PTFE membrane to target only dissolved NOM species. Batches were made as needed, and used immediately. Initial pH was adjusted before DOC analysis by NaOH or H_2SO_4 (Laboratory Grade, Fisher Scientific) to attain a pH of 7.00 ± 0.05. Temperature did not change significantly with the given parameters, and all experiments were conducted at 20 ± 1 °C.

3.2.3. Analytical Methods

Filtrate was analyzed for remaining DOC by a UV/persulfate oxidation TOC analyzer (Shimadzu TOC-VCPH). Temperature, pH (Denver Instruments ATC UB-10), and conductivity (YSI-3200) were monitored. Absorbance measurements were determined using a UV-Vis spectrophotometer (Shimadzu UV-mini 1240) with a cell path of 1 cm. Iron concentrations were measured by inductively coupled plasma optical emission spectroscopy (ICP-OES) with a wavelength of 238.204 nm for iron (PerkinElmer Optima 7300 DV).

3.2.4. Electrocoagulation

The EC reactor, iron electrode grades, and procedure were the same as described in Chapter 2. After electrolysis, the electrodes were removed, and the solution was either immediately filtered on a new 0.45 μm PTFE membrane filter for DOC and UV-abs-254 analysis, or transferred to a flocculation and settling tank for UV-abs-254 analysis only. All experiments were performed in duplicate. The relationship between *CL* and *ML* followed Faraday's Law as described previously in equation (2-4). Experimental *ML* was determined by ICP-OES analysis of samples acidified with a 3:1 HCl to HNO_3 (Laboratory grade, Fisher Scientific) solution of *aqua regia*. Due to variability in φ, most results are reported with *CL* as the independent variable.

3.3. Results and Discussion

3.3.1. Effect of Current Density

DOC and UV-abs-254 reductions were noticeably different between high and low i (Figure 3-1). At i=26.8 mA/cm^2, DOC and UV-abs-254 reductions were 67% and 66%, respectively, while i in the range of 2.43 to 13.4 mA/cm^2 had average removals of 73% and 88% for DOC and UV-abs-254, respectively, with no significant difference in either DOC or UV-abs-254 between them (95% confidence).

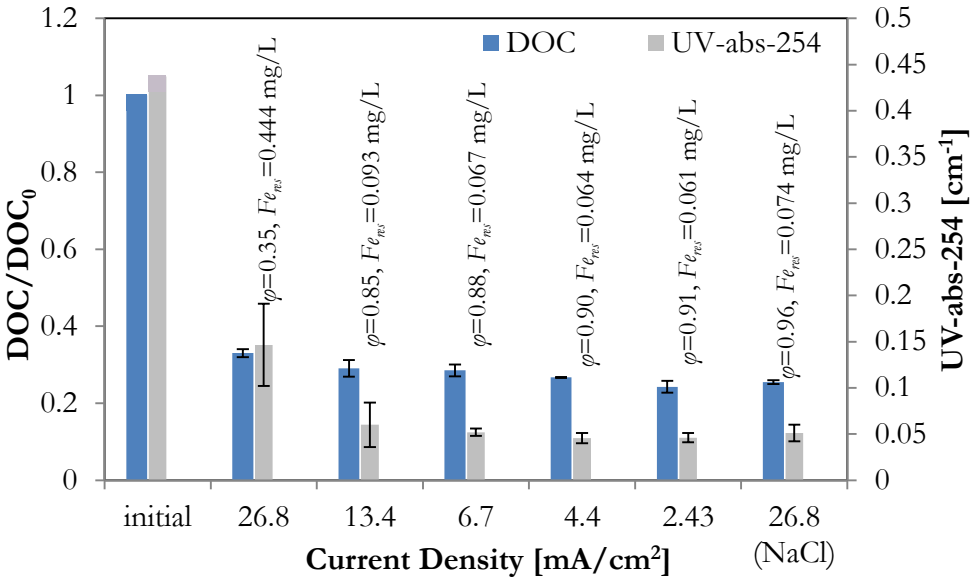

Figure 3-1: DOC and UV-abs-254 reduction with differing *i*, φ and Fe_{ris} for each *i*. DOC_0=13.79 mg/L, *I*=0.5 A, t=2 min, *CLR* = 500 C/L/min, E_{cell} ≈ 1.9 V (2.43 mA/cm^2), 4.8 V (26.8 V, 26.8 mA/cm^2)

It is obvious that current density is a key EC variable affecting the overall electrode area, total reactor footprint, and total power consumption; however; many studies in the literature unfortunately do not control between current (*I*) and *i* ($i=I/A$). For instance, some studies (e.g., Aber et al., 2009) consistently reported that a higher *i* was associated with better pollutant removal, without stating that it was actually due to the increase in total current (and thus *CL*), not just due to an increase in *i*. Relatively few studies (Table 3-1) investigated the actual relationship between *i* and pollutant removal, likely because it requires keeping several variables constant: electrolysis time, pollutant-coagulant contact time, total current, and solution volume; while varying the electro-active surface area. Results here show a

notable effect of *i* on NOM removal when controlled for pollutant-coagulant contact time, suggesting different conclusions than those of Chen et al. (2000) and Golder et al. (2007), where identical removal at differing *i* is shown in italics in Table 3-1.

Table 3-1: Previous investigations of pollutant removal at different current densities

Study, electrode metal, pollutant	Volume [L]	Surface Area [cm^2]	Current Density [mA/cm^2]	Current [A]	Electrolysis Time [min]	Metal Loading [g/L]	C_i [ppm]	Removal [%]
(Chen et al., 2000) Aluminum,COD	0.3	320.0	1.25	0.4	9.5	0.071[a]	1910	*77*
	0.3	36.73	10.89	0.4	9.5	0.071[a]	1910	*77*
(Golder et al., 2007) Iron, Cr^{3+}	0.8	61.5	16.26	1.0	60	1.302	1000	*78*
	0.8	30.74	32.52	1.0	60	1.302	1000	*78*
(Holt et al., 2005) Aluminum,Clay	6.97	732	0.34	0.25	240	0.048[a]	0.8	**99.1**
	6.97	732	1.4	1.0	60	0.048[a]	0.8	95.1
(Zhu et al., 2007) Aluminum, F^-	0.3	54	0.46	0.025	20	0.009[a]	5	**72**
	0.3	54	9.26	0.5	1	0.009[a]	5	48
(Mouedhen et al., 2008) Aluminum,Cu^{2+}	0.9	54	5.0	1.08	75	0.124[a]	59	**99.9**
	0.9	54	20.0	0.025	19	0.124[a]	59	98
(Addy, 2009) Iron, As	0.85	27.27	1.10	0.03	75	0.051	0.590	**98.9**
	0.85	2.7	100.0	0.27	9	0.051	0.570	97.7

[a] – indicates that dose was back-calculated with Faraday's Law

Higher removal at lower current densities shown in this investigation was in accordance with several other reports (Holt et al., 2005; Zhu et al., 2007; Mouedhen et al., 2008; Addy, 2009), where greater removal at lower *i* is shown in bold in Table 3-1. The discrepancy may be explained by any of the following reasons: *i*) decreased φ at higher *i*, ii) better mixing (i.e., pollutant-coagulant contact) properties at lower *i*, or iii) different speciation or smaller

coagulant hydr(oxides) generated at higher *i*, as seen elsewhere (Pascal et al., 1999). The results here show lower φ at higher *i* (Figure 3-1), showing that less total iron, had a significant effect on NOM removal. When NaCl replaced Na_2SO_4 as the supporting electrolyte (Figure 3-1 – far right column), a higher *i* had no impact on φ or NOM removal. This was likely due to electrochemical chlorine gas evolution causing pitting corrosion (Mechelhoff, 2009), preventing a passivation layer build-up at greater *i*. Since NaCl dosing would be a significant disadvantage for drinking water treated by EC, *i* remains a significant parameter in EC design for drinking water treatment. An optimized EC reactor should operate at the highest *i* possible without showing adverse effects, which would allow for the smallest electrode area and reactor footprint. Thus, EC for drinking water treatment should operate at no higher than $i \sim 10$ mA/cm^2, while *i* of 6.7 mA/cm^2 and less show diminishing NOM removal for greater electrode area.

3.3.2. Effect of Charge Loading Rate

The effect of differing *CLR* on NOM removal (Figure 3-2) clearly demonstrates that a lower *CLR* led to greater DOC and UV-abs-254 reduction. A *CLR* of 1000 C/L/min led to DOC and UV-abs-254 reductions of 61.8% and 40.1%, respectively, while reductions were an average of 67.3% and 85.1%, respectively, for *CLR* values from 200 to 500 C/L/min.

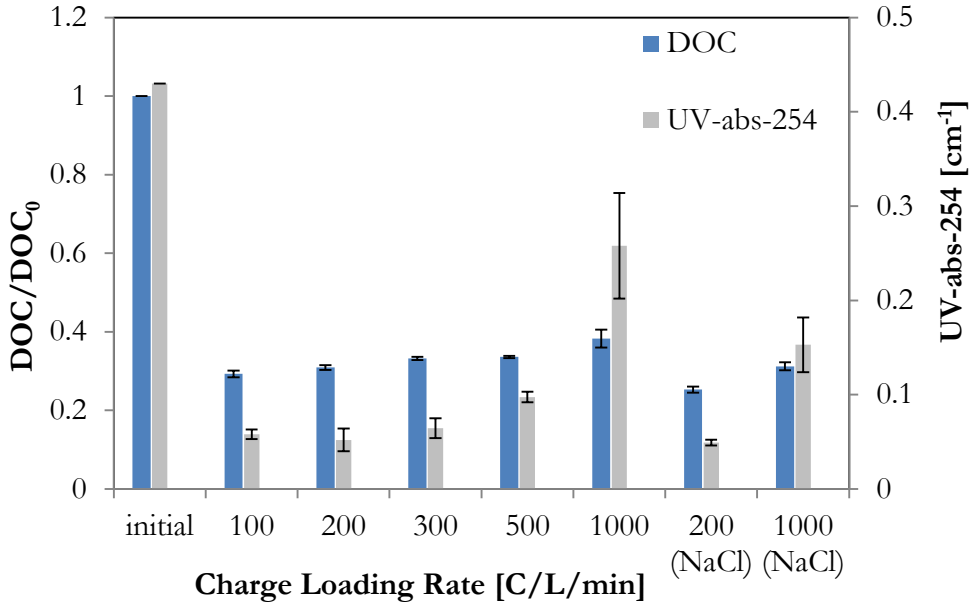

Figure 3-2: DOC and UV-abs-254 reduction with differing charge loading rates. DOC_0=13.79 mg/L, *CL* = 1000 C/L, *i* = 5.36 mA/cm^2, $E_{cell} \approx$ 2.3 V

UV-abs-254 removal was more significant than DOC removal at a slower *CLR* due to lower residual iron concentrations. However, it is worth noting that UV-abs-254 was reduced by 85% with a *CL* of 250 C/L at 500 C/L/min, about 40 times faster for similar reductions in Holt et al. (2005) for a similar *CL*. Greater *CLR* did not change φ as may have been expected, which remained at 0.65±0.03 for all *CLR* tested. This was because *i* (5.36 mA/cm^2) and coagulant flux (7.69 mmol Fe/cm^2·s) were maintained constant by modifying electrode surface areas. When NaCl replaced Na_2SO_4 for 200 or 100 C/L/min, φ increased to > 0.95 (Figure 3-2 – far right columns). However, DOC removal was still low for high *CLR*, irrespective of φ. Thus, higher *CLR* was associated with lower DOC removal due to: *i*) less pollutant-coagulant contact time (see section 3.3.3: Effect of Dosing Mode), or ii) the

sharp pH increase with higher values of *CLR*. pH increased immediately after EC from 7.0 to 8.6 at 100 C/L/min, while it increased to 9.3 at 1000 C/L/min. The pH increase was only temporary, as seen elsewhere (Holt et al., 2005), but may have been high enough to cause temporary increased solubility of iron species and lower coagulation, reducing EC effectiveness.

These results have valuable implications for EC as a process, since industrial EC units generally operate at high *i* (up to 1000 mA/cm^2) and *CLR* (up to 30 000 C/L/min), to minimize reactor footprint for economic purposes. While *i* has a relationship between total current and electrode area, *CLR* has a relationship between total current and electrolysis time. There are thus three basic operational variables between the inter-related *i* and *CLR*: total current, electrode area, and electrolysis time. For a constant *CL* in either batch or continuous mode, EC units would normally operate at one of four different combinations or "classes" of these three basic operational variables, shown in Table 3-2.

Table 3-2: Operational classes for EC systems for constant charge loading

	Operational Variables			**Resulting Parameters**	
EC Operating Classes	Current	Electrolysis Time	Electrode Area	*i*	*CLR*
Class I	High	Short	Small	High	High
Class II	High	Short	Large	Medium	High
Class III	Low	Long	Small	Medium	Low
Class IV	Low	Long	Large	Low	Low

To optimize the EC process, operating classes II, III, and IV will have a lower *i* and thus lower electrical power consumption, especially important for drinking water treatment where

conductivity enhancing salts cannot be added. The difference between classes II and III/IV is a high or low *CLR*, which becomes a matter of application appropriateness. If total process time or total volume processed per day is more important, operating an EC unit at a high current and short electrolysis time is preferable (class II EC), although may require flocculation (post-electrolysis) at lower *CL* (see section 3.3.3:Effect of Dosing Mode). If cost per volume treated is more important than total volume treated, a low current and long electrolysis time is preferable (class IV EC), but will lead to a longer total process time, up to 4 hours in some EC reports (Holt et al., 2002).

3.3.3. Effect of Dosing Mode

Previous studies on the effect of flocculation time for EC showed conflicting results, some reporting no benefit (Ryan et al., 2008; Essadki et al., 2009) and others reporting greater pollutant removal with greater flocculation time (Linares-Hernandez et al., 2007; Sasson et al., 2009). The effect of post-EC flocculation times for the "fast" mode at two different *CL* values is shown in Figure 3-3.

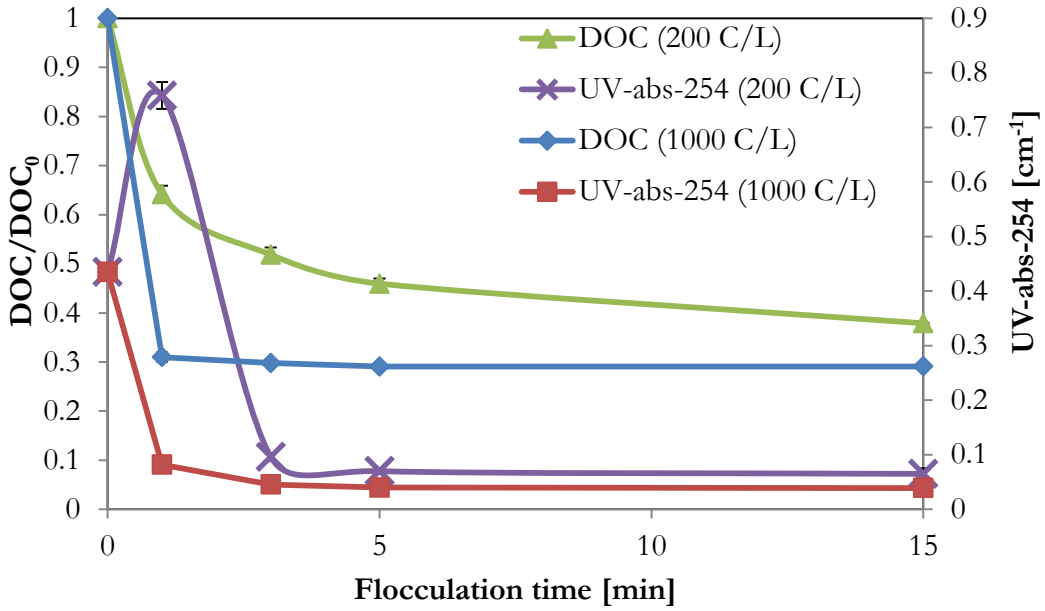

Figure 3-3: Effect of flocculation time on DOC and UV-abs-254 reduction with the "fast" dosing mode and two different *CL*. DOC_0=13.79 mg/L

Flocculation time had a significant effect for 200 C/L, with 46% reduction in DOC with a mixing time of 1 minute and 63% DOC reduction after 15 minutes of mixing. For 1000 C/L, there was little benefit of post-EC flocculation, times greater than one minute showed no additional DOC or UV-abs-254 reduction. Floc growth and pollutant removal likely took place during electrolysis; the higher *CL* caused almost instantaneous coagulation. This was likely the case for the other studies reporting similar results (Ryan et al., 2008; Essadki et al., 2009), these studies operated at a high *CLR* and high *CL*, where no significant effect of flocculation time would be observed. For 200 C/L, the increase in UV-abs-254 after one minute of flocculation is explained by higher residual iron that did not have enough time to coagulate, passing through filtration. For the "slow" dosing mode, results followed a similar

trend, with no benefit of post-EC flocculation at 1000 C/L, and only an additional 8% in DOC removal with 200 C/L and 15 minutes of post-EC flocculation.

These results suggest that at a lower *CL*, post-electrolysis flocculation is critical for high *CLR* values ("fast" mode), and only slightly beneficial for low *CLR* values ("slow" mode), while at a higher *CL*, post-electrolysis flocculation has little benefit regardless of *CLR*. This finding explains the higher residual DOC at higher *CLR* seen earlier; higher *CLR* requires either greater total dose (*CL*) or greater post-EC flocculation time for maximum NOM removal. Consequently, the major difference between dosing modes is that the "fast" mode requires post-EC flocculation at lower *CL*, while flocculation in the "slow" mode can be done either externally or *in-situ* within the EC reactor. There is thus a trade-off between total process time and total coagulant dose.

To assess sedimentation for floc removal, the "fast" and "slow" modes with a high and low *CL* were compared with either 0.45 μm filtration or 2 hr sedimentation (Figure 3-4). For settling, UV-abs-254 rose significantly with the "fast" mode, due to suspended flocs mixed with a blanket of cathodically evolved hydrogen gas. This was a similar finding to other reports (Holt et al., 2005), that a lower *CLR* and hydrogen flux allowed for better settling. Thus, for applications where flotation or direct filtration are not feasible, operating EC only in a "slow" dosing mode will allow for settling, whereas operating in the "fast" mode will make settling almost impossible.

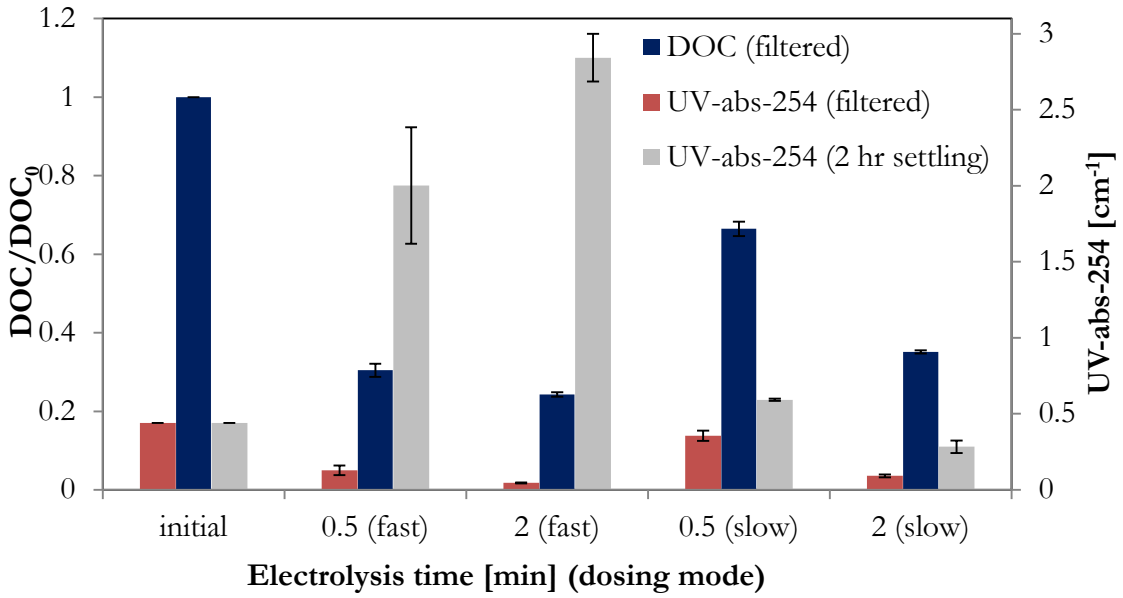

Figure 3-4: DOC and UV-abs-254 reduction with different flocculation modes with 0.45 µm filtration and UV-abs-254 with 2 hr settling. DOC_0=13.79 mg/L

Classes II and IV are both used currently in industry in both batch and continuous operations, with no apparent distinction between them. For drinking water, low conductivity suggests that *i* should be minimized to reduce ohmic drop, and prevent the system from operating at high voltages, suggesting a preferable operational class IV. For wastewater treatment, where conductivity enhancing salts can be added, it makes more sense to operate class II EC, treating higher flow rates with a shorter reactor residence time, as the voltage difference and electrical cost at higher *CLR* values would likely be minimal. This distinction is not-trivial and greatly affects metal and electrical consumption, affecting total cost as well as environmental impact.

3.3.1. Effect of pH adjustment

Post-EC pH was adjusted to values of 6.0 and 7.0 immediately after EC for both the "fast" and the "slow" dosing modes, results are shown in Figure 3-5.

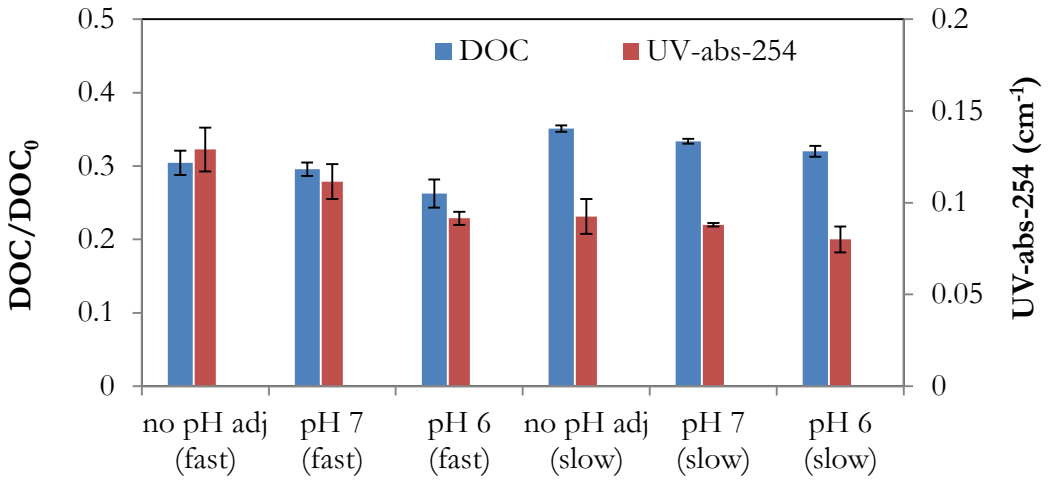

Figure 3-5: DOC and UV-abs-254 reduction with different pH adjustment and dosing modes. t=0.5 min (fast), 2 min (slow), DOC_0=13.79 mg/L, UV-abs-254_0=0.439 cm^{-1}.

For both modes, an adjustment to pH 6.0 led to slightly greater DOC and UV-abs-254 removal than with pH 7.0 or unadjusted pH. Adjustment to pH 6.0 with the "fast" mode gave 13.8% greater DOC and 29.1% greater UV-abs-254 removal compared to the baseline without pH adjustment, while pH 6.0 and the "slow" mode gave an only 8.8% and 13.5% greater removal for DOC and UV-abs-254 than the baseline, respectively. These show different findings than Larue et al. (2003), who found an optimum coagulation pH of 7.0-7.6

for iron EC. Instead, results show similar conclusions to iron chemical coagulation studies, which indicate optimum pH of 4.0-6.0 for both drinking water (Lefebvre and Legube, 1990) and wastewater (Adin et al., 1998). Interestingly, pH adjustment had a more significant effect with the "fast" mode than with the "slow" mode, likely caused by the greater pH increase with the "fast" mode. This is explained by the higher pH increase with a larger CLR, as described earlier, the very short period between electrolysis and filtration in the "fast" mode did not allow for pH to return to its initial (lower) value, explaining the greater reduction with pH adjustment in the "fast" mode.

3.4. Chapter Conclusions

In this chapter, iron EC was shown to effectively remove NOM, and operating parameters were investigated for optimization of metal and electricity consumption. Several conclusions are made from results from this chapter's work:

- A general correlation was found between increased i and decreased current efficiency (φ), affecting NOM removal. Optimum NOM removal was found at i ~10 mA/cm^2.
- A lower *CLR* showed greater total DOC removal, while a higher *CLR* led to less reactor residence time and required either longer post-electrolysis flocculation or greater coagulant dose for similar NOM removal.

- Four general EC "classes" of operation were defined that have implications on several important measures of success: coagulant dose, electrical consumption, process speed, volumetric footprint, and post-EC flocculation requirements. These classes are expected to standardize reactor design for EC, in the hopes of greater comparability and more streamlined research within the academic and industry EC community.
- Two of these classes were further examined for DOC removal, showing that a "fast" EC mode without flocculation is more appropriate for smaller applications, while a "slow" EC mode is more effective for large permanent applications, where flocculation and settling can reduce coagulant and electrical consumption
- pH adjustment showed differing results for both of these classes, showing greater effect on NOM removal for the "fast" mode, due to the larger pH increase seen in the "fast" mode. This suggests that pH adjustment may not be necessary for "slow" EC, distinguishing it completely from CC as a technique not requiring this complex step, which is often difficult for small rural communities due to the handling, dilution, and dosing of acids and bases.

4. *In-situ* Identification of EC Iron Speciation in Natural Water

4.1. Chapter Introduction

In Chapter 2, iron EC showed greatest NOM removal in local water. Chapter 3 showed that NOM removal differed with differing EC parameters, specifically *i* and *CLR*. This chapter aims to investigate if iron speciation could be a cause for the differing NOM removals seen at differing parameters. EC operating parameters, e.g., *i*, *CLR*, pH, anodic oxygen generation, current efficiency, and dosing rate, are known to affect iron speciation (Cañizares et al., 2007; Moreno et al., 2007; Lakshmanan et al., 2009), directly affecting pollutant removal due to the properties and crystal sizes of different species (Yavuz et al., 2006; Bagga et al., 2008; Addy, 2009). However, the role between iron speciation and subsequent pollutant removal has not yet been investigated. Iron speciation in EC is a complex phenomenon similar to corrosion that depends on several contributing factors: anode potential, pH, temperature, dissolved oxygen (DO), $[Fe^{2+}]$:$[Fe^{3+}]$ ratio, rate of reactant addition, and co-occurring solute concentration (Cornell and Schwertmann, 2003). It has only been superficially explored in EC, and end-products have generally been determined to be a mixture of iron oxides, hydroxides, and oxide-hydroxides, collectively referred to as the iron hydr(oxides). Specific compounds have been identified, usually by an *ex-situ* X-ray analytical technique, including: magnetite (Tsouris et al., 2000), hematite, goethite, lepidocrocite (Moreno et al., 2009), green rusts (GR) (Moreno et al., 2007), and ferrihydrite (van Genuchten et al., 2011). However, no study to this author's knowledge has looked at

the impact of differing hydr(oxide) generation on pollutant removal with iron EC, likely due to the difficulty of their real-time, *in-situ* identification. Wet-objective Raman spectroscopy is an *in-situ* technique uniquely suited to this task for several reasons: water does not interfere with Raman scattering, area mapping and depth profiling can give a three-dimensional characterization map, each iron hydr(oxide) has a unique Raman scattering spectra, identification is non-destructive and fast (resolve spectra in less than one minute), and low-laser strengths do not alter the compound structure by thermal or photon effects (de Faria et al., 1997). The combination of *in-situ* Raman and NOM characterization techniques, such as HPSEC, would give quantitative evidence of the impact of differing EC operating parameters on iron speciation, total DOC removal, and AMW NOM fraction removal in local water. The objective of this chapter was to not only identify *in-situ* the iron species generated in NOM-containing waters, but to determine the impact of the different species on NOM removal.

4.2. Materials and Methods

4.2.1. Waters

Stanley Park (SP) local water, as in Chapter 2, was collected from Lost Lagoon, Stanley Park, raw water characteristics are shown in Table 4-1.

Table 4-1: SP water properties.

DOC_0 [mg/L]	13.31
UV-abs-254_0 [cm^{-1}]	0.560
$SUVA_0$	4.21
pH_0	6.1
Conductivity [µS/cm]	990
Chloride [mg/L]	220
Dissolved Oxygen [mg/L]	5.2
Alkalinity [mg/L $CaCO_3$]	28

Local natural water was chosen over synthetic water in this work for real-world application and to explain findings of Chapter 2. Temperature did not change significantly (< 2 °C) with the given EC parameters, and all waters were allowed to equilibrate to 20 ± 1 °C before use.

4.2.2. Electrocoagulation

EC was studied in two different reactor configurations for NOM removal, one for bulk property measurement, and the other for *in-situ* Raman. For bulk NOM removal, a custom 50 mL parallel plate electrochemical batch reactor was manufactured from acrylic for combined electrolysis/flocculation. The anode was a 99.9% pure iron foil of 1 mm thickness (Goodfellow), precision cut to differing nominal area dimensions of 10-250 mm^2, connected via glass-insulated copper wire. The cathode was a 20 mm x 20 mm 99.99% pure platinum foil of 0.2 mm thickness (Goodfellow), the inter-electrode gap was 10 mm. A DC

power supply (Instek PSP-603) supplied DC current in galvonostatic mode. The *in-situ* Raman reactor was identical, but scaled down by an order of magnitude to fit in the Raman spectroscopy unit. Before each experiment, electrodes were wet-polished with P200 SiC, P1500 SiC, and emery paper, rinsed with 1% sulphuric acid, and double rinsed with Milli-Q water. Electrolysis took place directly after polishing to avoid surface film formation. Two EC operational parameters, *i* and *CLR* were established in Chapter 3 as the most important affecting NOM removal. Three *i* values in the range of 1-25 mA/cm^2 and three *CLR* values of 12-300 C/L/min were investigated for impact on pH, DO, iron speciation, and NOM removal. After electrolysis, the electrodes were removed, and the system underwent slow flocculation (60 rpm) with a magnetic stir-bar for 10 minutes under a blanket of 99.99% N_2 gas (Praxair) to maintain DO concentration. The solution was then immediately filtered without sedimentation on a new 0.45 μm PTFE membrane filter for analysis. The relationship between charge loading (*CL*) and metal loading (*ML*) is described by Faraday's Law, equation (2-4). *ML* doses in the range of 3.6-57.6 mg Fe/L were calculated for z=2, and φ was determined experimentally for an *i* range of 1-125 mA/cm^2 and a *CLR* range of 12-600 C/L/min. Samples for φ investigation were acidified with 1 mL of a 3:1 HCl to HNO_3 (Laboratory grade, Fisher Scientific) solution of *aqua regia,* and a further 10 mL of 5% *aqua regia* solution was used to rinse the electrodes of remaining iron precipitate. Initial SP water iron concentrations were subtracted from determined values for φ determination.

4.2.3. *in-situ* Raman

A Raman spectroscopy system (InVia, Renishaw) equipped with a 785 nm laser and 160 mW (at 1-10% = 1.6-16 mW) excitation laser was employed with a 40x wet-objective (Leica HCX APO 40x) immersed directly above the iron anode. A 12.7 mm diameter thin gold mirror (ThorLabs Inc.) was immersed in solution directly underneath. Electrode areas were scaled to 1-25 mm^2, maintaining relative dose, *i* and *CLR* as above. The laser was focused in the median plane immediately adjacent to the perpendicular anode, and directly above the gold mirror, and kept irradiated during the entire electrolysis, shown in Figure 4-1.

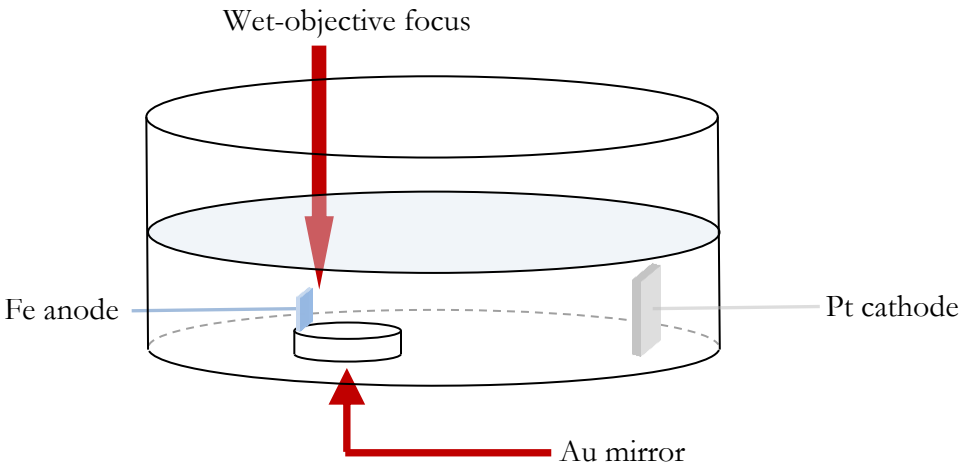

Figure 4-1: Scaled EC system for *in-situ* Raman characterization

Occasionally, the laser had to be repositioned and refocused for higher spectra resolution. This method allowed the identification of predominate oxide forms being generated, *i*.e., formed less than a few millimeters from the anode surface within a 60s timeframe, although did not capture intermediate transformations. To reduce collection times, spectra were obtained only for the iron hydr(oxide) fingerprint region from 200 to 1400 cm^{-1}. Background spectra were obtained for SP water, and found to have no significant peak contributions from NOM. Raman spectra are thus presented as raw data, normalized over total peak intensity, with fluorescent light interference removed.

4.2.4. Analytical Methods

Filtrate was analyzed for remaining NOM by a UV/persulfate oxidation TOC analyzer (Shimadzu TOC-VCPH). Temperature, pH (Denver Instruments ATC UB-10), DO (YSI-52), and conductivity (YSI-3200) were monitored. pH and DO measurements took place in bulk solution directly above the electrode couple. UV-abs-254 was taken after filtration, determined using a UV-Vis spectrophotometer (Shimadzu UV-mini 1240) with a cell path of 1 cm. Iron concentrations were measured by inductively coupled plasma optical emission spectroscopy (ICP-OES) with a wavelength of 238.204 nm (PerkinElmer Optima 7300 DV).

For HPSEC analysis, 100 μL samples were filtered to 0.45 μm, and injected into a HPLC system (Waters 2696 Separation Module, Waters 2487 dual λ absorbance detector at 260 nm,

Waters Protein-Pak 125 Å column) as described in Chapter 2. All analytical measurements were performed within 2 hours of each experiment, or were kept for a maximum of 8 hours at 5°C before analysis, and all experiments were performed in duplicate. Standard error is reported as vertical error bars in all figures.

4.3. Results and Discussion

4.3.1. EC Current Efficiencies

Theoretical and experimental iron doses for differing *CLR* (Figure 4-2) and *i* (Figure 4-3) show evidence for a current efficiency of essentially unity and a charge transfer coefficient of z=2 at all *i* and *CLR*.

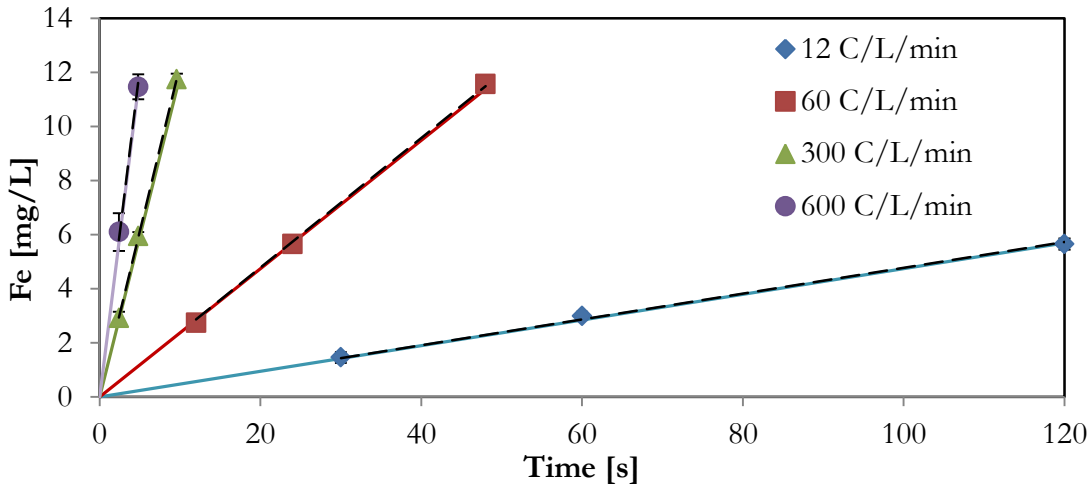

Figure 4-2: Experimental and theoretical Fe dissolution: impact of *CLR* (*i*= 12.5 mA/cm^2). Solid markers are experimental values, solid lines are Faradaic values with *z*=2, dashed lines in A are linear regression of experimental data.

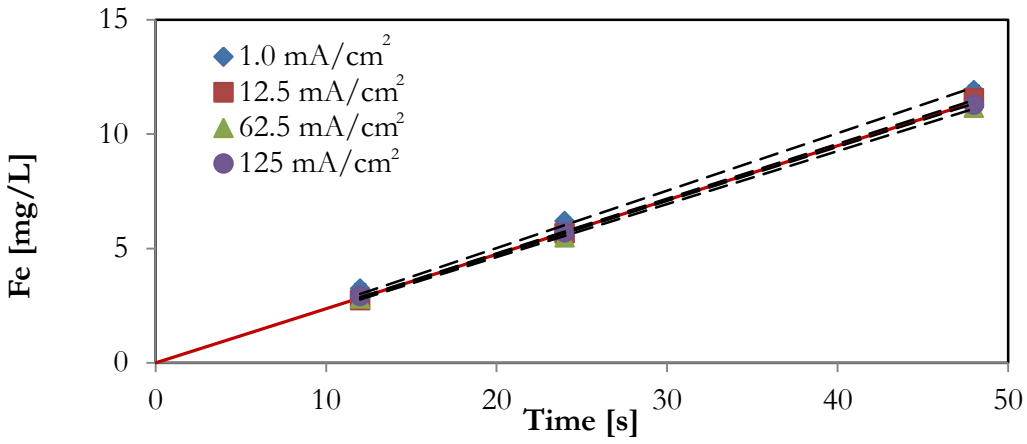

Figure 4-3: Experimental and theoretical Fe dissolution: impact of *i* (*CLR* = 60 C/L/min). Solid markers are experimental values, solid lines are Faradaic values with *z*=2, dashed lines in A are linear regression of experimental data.

While some studies have reported z=3 (Pascal et al., 1999; Moreno et al., 2009), results here are in very good agreement with recent evidence (Lakshmanan et al., 2009; Tanneru et al., 2012). All *CLR* and *i* values showed an average of φ=0.96 ± 3%. High linearity ($R^2_{average}$=0.997) was also observed, allowing appropriate interpolation. Only a *CLR*=600 C/L/min showed higher variability (Figure 4-2) with φ=1.03 ± 10%, likely due to greater sensitivity at faster step inputs. There was no statistical difference between all *i* values tested and the effect on φ (95% confidence using Student's t-test). A current efficiency of essentially unity was likely a result of three simultaneous experimental conditions being met: *i*) polished electrodes, whereas unpolished electrodes can decrease current efficiency (Cañizares et al., 2007; Lakshmanan et al., 2009), ii) rinsing the electrodes in dilute acid, as flocs can be bound to electrode surfaces, and iii) appreciable chloride content of the raw

water (220 mg/L), causing pitting corrosion (Mechelhoff, 2009), as previously reported in Chapter 3 to increase φ for iron EC. While the possibility of other reactions occurring with no change in net current has been explored previously in EC (Mechelhoff, 2009), such as anodic oxygen evolution and subsequent cathodic reduction, anodic oxygen was not seen at any conditions in this study.

4.3.2. Impact of *i* and *CLR* on pH and DO

A distinct pH increase was seen at higher *CLR* values (Figure 4-4), increasing from 6.1 to 7.2 at 300 C/L/min, and to 6.5 and 6.2 for 60 C/L/min and 12 C/L/min, respectively.

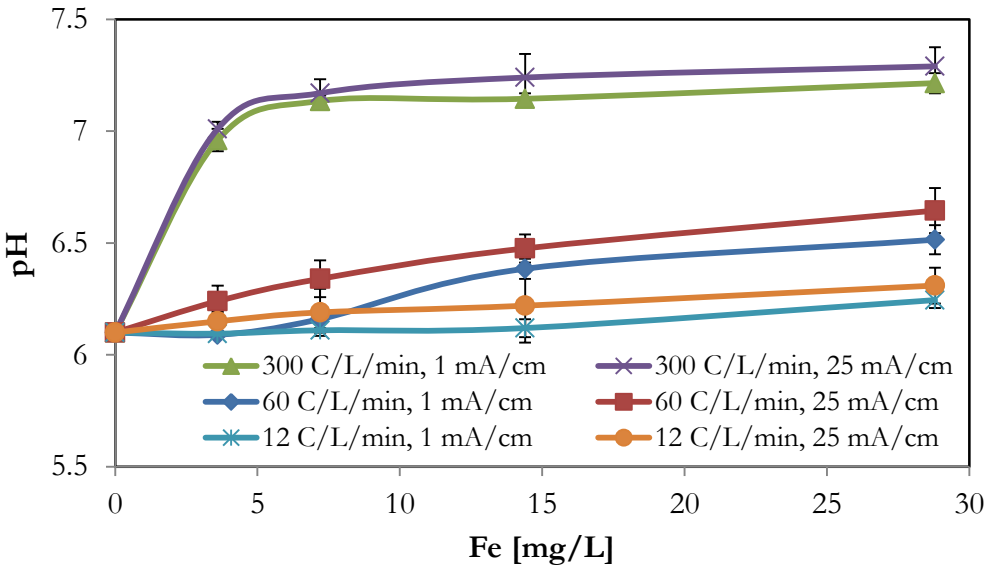

Figure 4-4: Impact of *i* and *CLR* on pH.

The increase in pH associated with EC is well documented, and has been explained as a consequence of cathodic hydroxide generation (Vik et al., 1984, Lakshmanan et al., 2009), with subsequent non-stoichiometric and/or incomplete hydr(oxide) precipitation. The greater pH increase at higher *CLR* has been seen elsewhere (Holt et al., 2002), although remains to be explained. This phenomenon was likely due to a faster rate (mol/s) of Fe^{2+} and OH^- generation at a higher *CLR*, with less total time of active electric field ($\nabla\Phi$). As $\nabla\Phi$ was present for less time, as was the case for the short electrolysis periods at higher *CLR*, there was less mass transfer of cathodically generated OH^- towards the anode, and more OH^- diffused to bulk solution. This arises from the fact that migration (first term) in the Nernst-Planck and substituted Nernst-Einstein equations for ionic motion would dominate diffusion under the applied $\nabla\Phi$, seen in equation (4-1):

$$N_i = -D_i \frac{zF}{RT} c_i \nabla\Phi - D_i \nabla c_i + c_i \vec{v} \tag{4-1}$$

where N_i is molar flux, c_i is species concentration, D_i is the species diffusion coefficient, and $\vec{v}$ is local fluid velocity. This assumes that H^+ remained in the anodic region, which has been shown for iron EC elsewhere (Mechelhoff, 2009; Moreno et al., 2009), and that $\nabla\Phi$ was equivalent at different *CLR* values, which was likely, since *i* was equivalent for different *CLR* values due to changes in electrode surface area. A slight pH increase at higher *i* was also observed, likely a cause of the same effects as with *CLR*, but at higher concentration due to less electrode surface area and a smaller control volume. The difference in pH at differing *i* was not statistically significant (95% confidence) with the small data sample size, but the trend highlights the effect. Higher *i* also caused greater N_{Fe2+}, creating a higher

localized concentration of Fe^{2+} ions closer to the anode, driving hydrolysis forward, seen in reaction (4-2):

$$4\,Fe^{2+} + 8\,H_2O \rightleftharpoons 4\,Fe(OH)_2 + 8\,H^+ \quad (4\text{-}2)$$

Similarly to higher *CLR*, this caused a greater proton imbalance with acidic pH near the anode, and higher basicity closer to the cathode. The pH increase was temporary, as seen elsewhere (Lakshmanan et al., 2009; Holt et al., 2002), and pH returned to approximately 6.3 for all *CLR* and *i* after several minutes, dictated in part by the solubility of the specific Fe^{2+} or Fe^{3+} iron compounds generated. Still, the important finding is the difference in localized pH in the region between the electrodes, where speciation takes place.

EC caused a distinct drop in DO (Figure 4-5), although ΔDO varied greatly depending on *i* and *CLR* conditions. Intermediate *CLR* and low *i* (60 C/L/min, 1 mA/cm^2) caused the greatest DO reduction with ΔDO=3.4 mg/L, while a high *CLR* and high *i* caused minimal DO reduction, ΔDO < 1 mg/L.

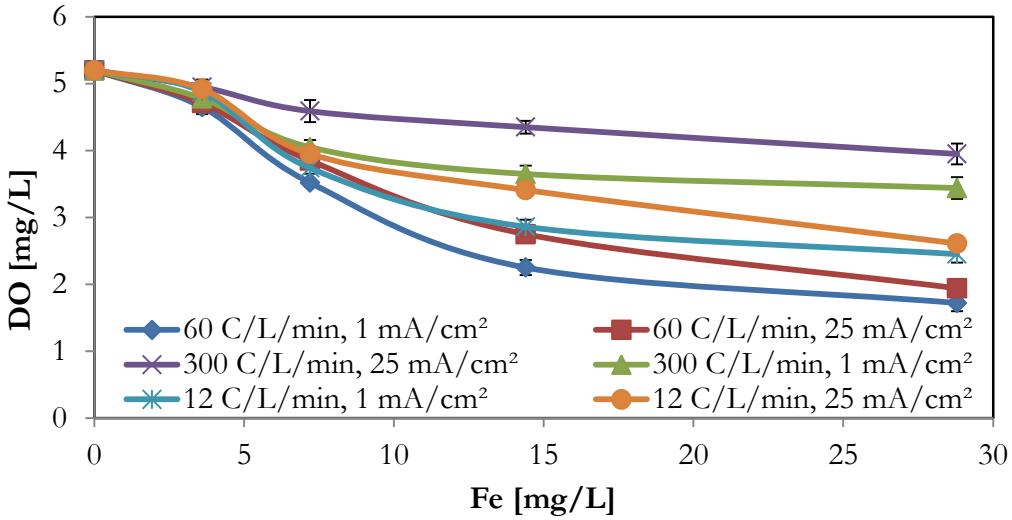

Figure 4-5: Impact of *i* and *CLR* on dissolved oxygen (DO).

The decrease in DO by EC has been noted previously (Lakshmanan et al., 2009; Addy, 2009), although has not been examined mechanistically. Consumption of DO has two primary mechanisms in Fe EC, Fe^{2+} oxygenation in reaction (4-3), and cathodic reduction in reaction (4-4), assuming neutral to basic conditions near the cathode as shown elsewhere (Moreno et al., 2009) and four electron transfer without H_2O_2 intermediate since the cathode was platinum (Fischer and Heitbaum, 1980):

$$4\,Fe^{2+} + O_2 + 4\,H^+ \rightleftharpoons 4\,Fe^{3+} + 2\,H_2O \qquad (4\text{-}3)$$

$$2\,H_2O + O_2 + 4\,e^- \rightleftharpoons 4\,OH^- \qquad (4\text{-}4)$$

It is certain that reaction (4-3) took place to some extent, as Fe^{2+} oxidation was evident from observation of Fe^{3+} in final hydr(oxide) products, even under N_2, and is known to be accelerated by the presence of NOM (Liang et al., 1993). It is also assumed that Fe^{2+}

oxidation by $Fe^{2+} \rightarrow Fe^{3+} + e^-$ does not occur in EC on the anode surface as seen by the high φ and elsewhere (Lakshmanan et al., 2009). However, the bulk of DO consumption was likely governed by operational parameters that affected the mass transfer limitations of reaction (4-4), demonstrated by the significant difference in residual DO at differing *i* and *CLR* (Figure 4-5) for identical iron *ML*. At higher *CLR* (300 C/L/min), there was less time for uncharged O_2 to diffuse from bulk solution to the cathode surface, leading to greater residual DO. At higher *i*, the smaller electrode surface area and associated greater H_2 flux ($mol/m^2/s$) also prevented O_2 from reaching the cathode surface, leading to greater residual DO. Higher $[OH^-]$ near the cathode likely retarded reaction (4-4) by unfavorable concentration gradients. At very low *CLR* (12 C/L/min), residual DO was not minimized due to inadequate mass transfer to the electrode surface due to negligible mixing from diminished H_2 bubble flux. These two extreme cases offer an explanation of why the intermediate *CLR* (60 C/L/min) led to the lowest residual DO. Regardless of the mechanism of either reaction (4-3) or reaction (4-4), DO consumption did not significantly affect bulk pH: as H^+ was consumed by Fe^{2+} oxidation in (4-3), OH^- was consumed in equal proportion as Fe^{2+} was oxidized to Fe^{3+} and hydrolyzed to a form of $Fe(OH)_3$. Likewise, if O_2 was reduced by four electron transfer on the cathode in reaction (4-4), a stoichiometric four OH^- species were equally consumed with the two Fe^{2+} ions generated on the anode and their subsequent hydrolysis to a form of $Fe(OH)_2$.

4.3.3. Impact of *i* and *CLR* on Iron Speciation

In-situ Raman spectroscopy at different *i* and *CLR* showed evidence for three different iron species: GR (Figure 4-6), Fe_3O_4 (Figure 4-7), and γ-FeOOH (Figure 4-9). Spectra were obtained continuously both during and after electrolysis, although better spectra were obtained approximately 60s after electrolysis had ended, likely due to greater particle agglomeration within the focused laser plane. Since iron speciation in corrosion is influenced by pH, DO, and $[Fe^{2+}]$:$[Fe^{3+}]$ ratio and rate of addition (Cornell and Schwertmann, 2003), and *i* and *CLR* directly affected pH and DO (Figure 4-4 and Figure 4-5), iron speciation was likewise influenced by EC operating conditions. A higher bulk pH at higher *CLR* (Figure 4-5) led to a lower localized pH close to the anode, as described earlier. Localized DO reductions near the electrodes were assumed to follow the same trend as bulk DO reduction, only to a greater extent; low bulk DO signified even less localized DO near the electrode surfaces and speciation region, assuming DO was not generated by electrochemical reactions or speciation, and was only affected by concentration diffusion in equation 2. Low bulk DO (< 2.5 mg/L) predominately generated a localized GR compound (Figure 4-6), seen at intermediate and higher *ML* (>14.4 mg Fe/L) at 60 C/L/min, 1 mA/cm^2 and 60 C/L/min, 25 mA/cm^2.

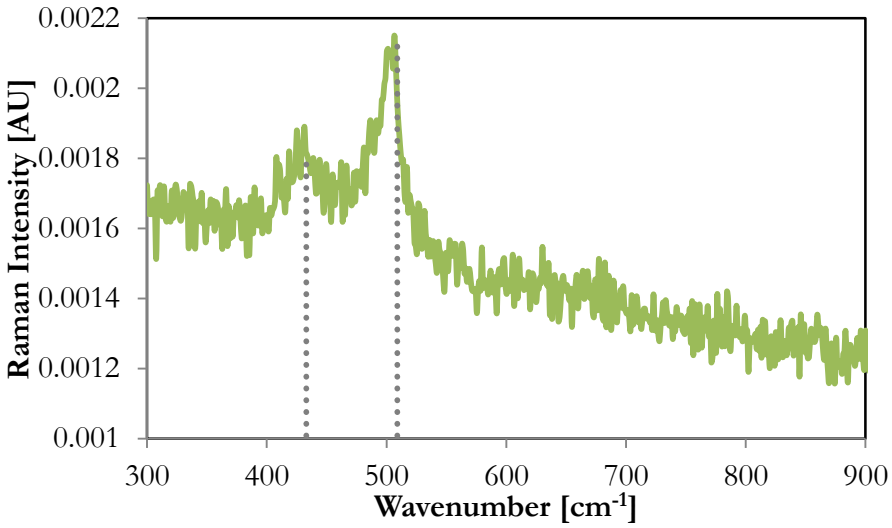

Figure 4-6: *in-situ* Raman spectra, dashed vertical lines are reference peaks for GR.

The role of pH in GR speciation was in mediating the rate of Fe^{2+} oxidation (4-3); a low *CLR* (12 C/L/min) led to a higher localized pH, a high Fe^{2+} to Fe^{3+} oxidation rate, and no GR formation. GR may have formed at higher *CLR* (300 C/L/min), but was likely oxidized by the greater DO at this condition before any identification could take place. A peak at 433 cm^{-1} is associated with the Fe^{2+}-OH stretch, and a peak at 509 cm^{-1} is associated with the Fe^{3+}-OH stretch (Bonin et al., 2000), showing some oxidation of Fe^{2+} to Fe^{3+} (and thus some residual DO) was necessary for GR formation. Peaks were seen for EC-GR compounds at 433 cm^{-1} and 505 cm^{-1}, identifying them as primary EC products without detection of intermediate species, although species such $Fe(OH)_2$ may have been generated but transformed faster than Raman capture times. Differentiation between GR1(Cl^- or CO_3^{2-}) and GR2(SO_4^{2-}) was not possible, secondary peaks were too small to distinguish from noise.

Intermediate *CLR* and high *i* (60 C/L/min, 25 mA/cm^2) caused a slightly higher DO (Figure 4-5), leading to favourable conditions for Fe_3O_4 generation (Figure 4-7) at high *ML* (28.8 mg Fe/L).

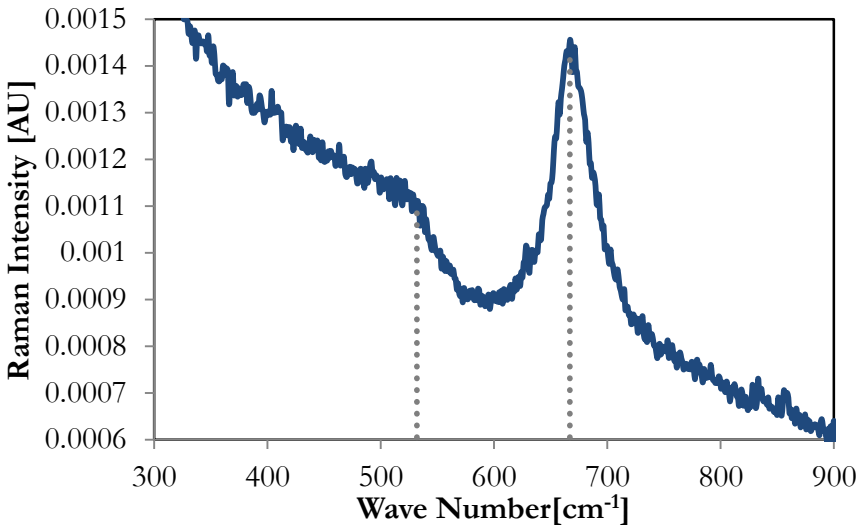

Figure 4-7: *in-situ* Raman spectra, dashed vertical lines are reference peaks for Fe_3O_4.

Raman peaks for Fe_3O_4 are known at 532 cm^{-1} and 667 cm^{-1} (Odziemkowski et al., 1994), which fit the obtained spectra precisely. The lack of any peak at 381 cm^{-1} or 718 cm^{-1} suggests direct evidence for Fe_3O_4, and not γ-Fe_2O_3 (maghemite), which has been identified in EC products (Moreno et al., 2009). This is valuable since Fe_3O_4 and γ-Fe_2O_3 are typically difficult to distinguish by traditional infra-red (IR), UV, or X-ray techniques. Stoichiometric Fe_3O_4 ($Fe^{2+}O{\cdot}Fe^{3+}{}_2O_3$) requires a 2:1 ratio of Fe^{3+}:Fe^{2+} and its precipitation is favorable only under slow Fe^{2+} oxidizing conditions (Cornell and Schwertmann, 2003), explaining why Fe_3O_4 was only seen with the slower Fe^{2+} generation at high *ML*, when some DO and Fe^{3+}

remained in solution. Greater *i* had a smaller electrode area and thus a higher Fe^{2+} and OH^- flux, also favouring Fe_3O_4 generation. Favourable Fe_3O_4 formation conditions (intermediate DO, 2:1 [Fe^{3+}:Fe^{2+}] ratio) were also expected at longer electrolysis periods at a slower *CLR*, and Fe_3O_4 was indeed confirmed at these conditions (12 C/L/min, 25 mA/cm^2; 60 C/L/min, 1 mA/cm^2), but only at very high *ML* (57.6 mg Fe/L) as a mixture of GR and Fe_3O_4 (Figure 4-8). Fe_3O_4 artifact peaks were also generated when higher laser strength (>16 mW) was used for extended periods on GR species, limiting laser strength in most samples to 1.6 mW.

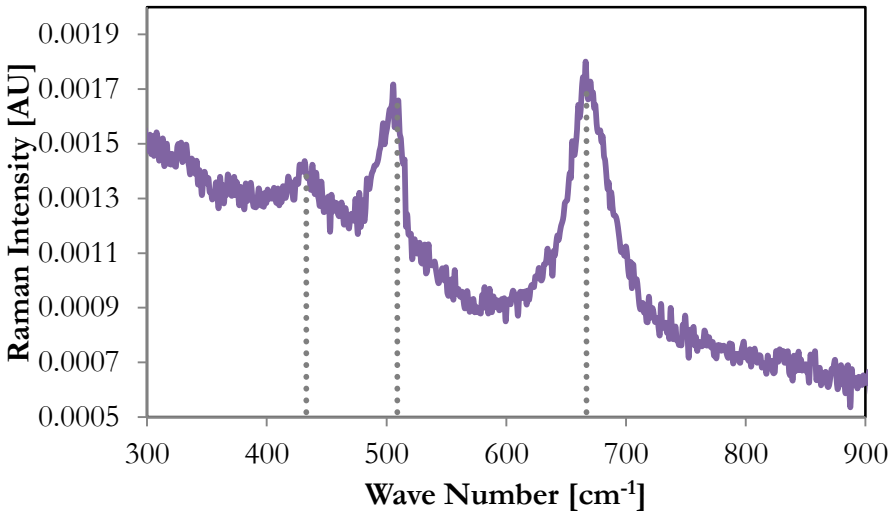

Figure 4-8: *in-situ* Raman spectra, dashed vertical lines are reference peaks for GR and Fe_3O_4 mixture.

At all other conditions which produced higher DO and/or higher localized pH near the anode, the only EC product captured on Raman spectra was γ-FeOOH (Figure 4-9).

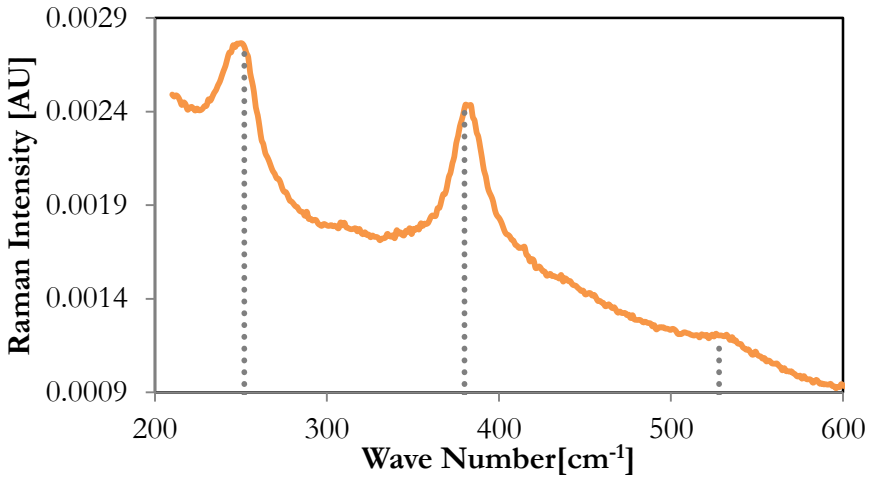

Figure 4-9: *in-situ* Raman spectra, dashed vertical lines are reference peaks for γ-FeOOH.

Raman peaks were observed at 248 cm^{-1}, 380 cm^{-1}, and 525 cm^{-1}, very close to tabulated peaks at 252 cm^{-1}, 379 cm^{-1}, and 528 cm^{-1} (Gui and Devine, 1995) which uniquely identify γ-FeOOH. γ-FeOOH was identified at both very high and very low *CLR* for all *ML*, making it the most commonly observed species in all tests. At high *CLR* (300 C/L/min, 1 or 25 mA/cm^2), DO was not significantly consumed (Figure 4-5), leading to greater Fe^{2+} oxidation. At low *CLR* and low *i* (12 C/L/min, 1 mA/cm^2), localized pH in the speciation region was likely higher due to low bulk pH increase (Figure 4-4). This also led to greater Fe^{2+} oxidation, as reaction (4-3) is inverse second order with pH, with a 100-fold faster reaction for every pH increase of 1 (Stumm and Lee, 1961). Both of these operating conditions (very high or very low *CLR*) led to a low $[Fe^{2+}]$, favouring γ-FeOOH generation over GR or Fe_3O_4. Noisier spectra were also obtained showing other known γ-FeOOH peaks at 660 cm^{-1}, 1054 cm^{-1} and 1307 cm^{-1} (Gui and Devine, 1995), clearly defining, for the

first time *in-situ*, the predominate "orange" compound in iron EC as γ-FeOOH, and not the typical amorphous iron (III) hydroxide product or ferrihydrite (Baltpurvins et al., 1996). This further suggests that the "orange" rusts are generated via the Fe^{2+} oxidation and precipitation pathway, and not necessarily the deprotonation pathway (Cornell and Schwertmann, 2003). Anode potential likely played some role in speciation in the current study, however; all electrochemical products at any anode potential (*i*.e., at any i) attempted in the current investigation were found to be Fe^{2+} (φ=1 for z=2) and not Fe^{3+} which is known to be possible at higher anode potentials, generating only Fe^{3+} compounds such as γ-Fe_2O_3 (Pascal et al., 1999). The only species identified by *in-situ* Raman were similar to chemical product speciation end-product identification (Williams and Scherer, 2001). Other species may have evolved during the 60s before a clear spectra emerged, e.g., an unstable $Fe(OH)_2$ intermediate, but spatiotemporal resolution in this chapter was not high enough to capture any EC products or transformations other than those reported here.

4.3.4. Impact of Iron Speciation on NOM removal

Figure 4-10A shows the DOC removal under the conditions of differing species generation (GR - 60 C/L/min, 1 mA/cm^2, Fe_3O_4 - 60 C/L/min, 25 mA/cm^2, and γ-FeOOH - 300 C/L/min, 1 mA/cm^2) as described above. Since $\varphi \approx 1$ for all conditions (Figure 4-2), differences in NOM removal were not due to differing total iron concentrations; they were instead due to either different iron speciation or different mass transfer effects between species and pollutant. All samples were well mixed after Raman identification before

analysis; any mass transfer effects were thus limited to those during coagulant generation. However, it was impossible to determine the separate contribution to NOM removal of differing mass transfer during coagulation and of differing speciation, since ionic mass transfer (localized pH, DO) directly affected speciation, as seen earlier. The assumption was that speciation played the dominant role, since mass transfer effects during generation suggest minimal interaction between NOM and flocs during the short electrolysis time.

The GR speciation conditions led to the greatest NOM removal, with a DOC reduction of 71% for a *ML* of 28.8 mg Fe/L, while the Fe_3O_4 condition led to the lowest NOM removal, 10% lower than GR, a reduction of 61% for the same *ML*. γ-FeOOH speciation caused an reduction of 65% for the same *ML*, intermediate between the two. UV-abs-254 reduction followed a similar trend (Figure 4-10B), with maximum reductions at 28.8 mg Fe/L of 87% with GR and 77% with Fe_3O_4.

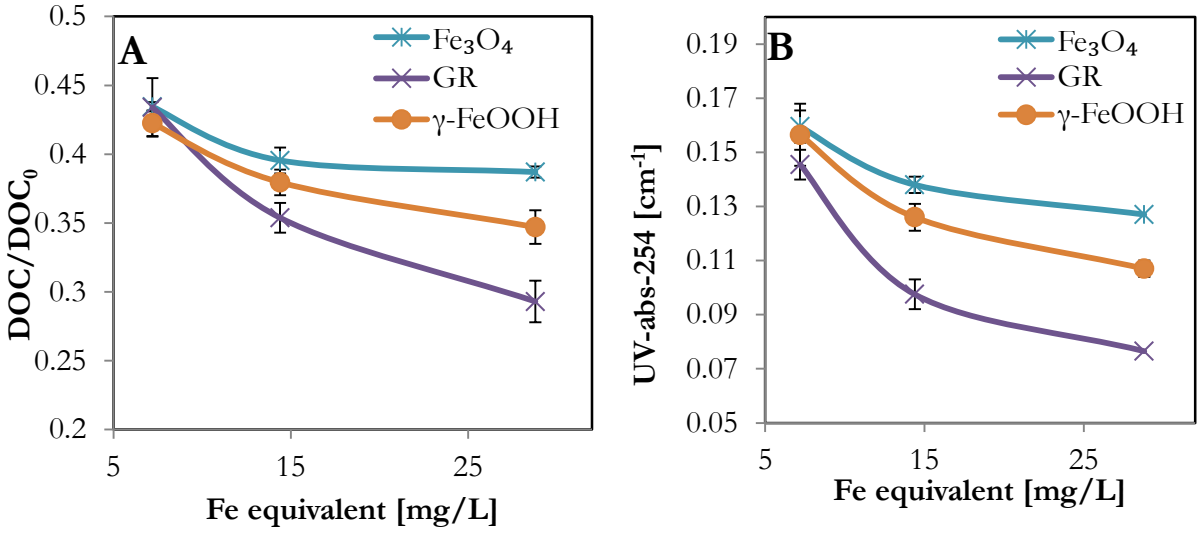

Figure 4-10: Impact of iron speciation on NOM removal A) DOC B) UV-abs-254

Interestingly, similar NOM removal was seen for all three species at lower *ML* (7.2 mg Fe/L) with an average of 58% DOC reduction and 72% UV-abs-254 reduction. This was likely since Fe_3O_4 and GR were only identified at higher *ML* (> 14.4 mg Fe/L) as noted earlier, lower *ML* values always gave a product of γ-FeOOH, explaining the similar DOC removal, and reinforcing the assumption that speciation played a greater role in NOM removal than mass transfer effects during coagulant generation. Higher *ML* showed very different NOM removals, since speciation was well differentiated. GR had the greatest DOC and UV-abs-254 removal, possibly due to the highly redox-active Fe^{2+} fraction causing localized reductions (Williams and Scherer 2001), the high edge density of hexagonal GR crystals (Wander et al., 2007), inducing coagulation mechanisms, or a preferential sorption/reduction of smaller NOM AMW fractions. HPSEC results showed significant differences in AMW NOM fractionation with differing speciation (Figure 4-11).

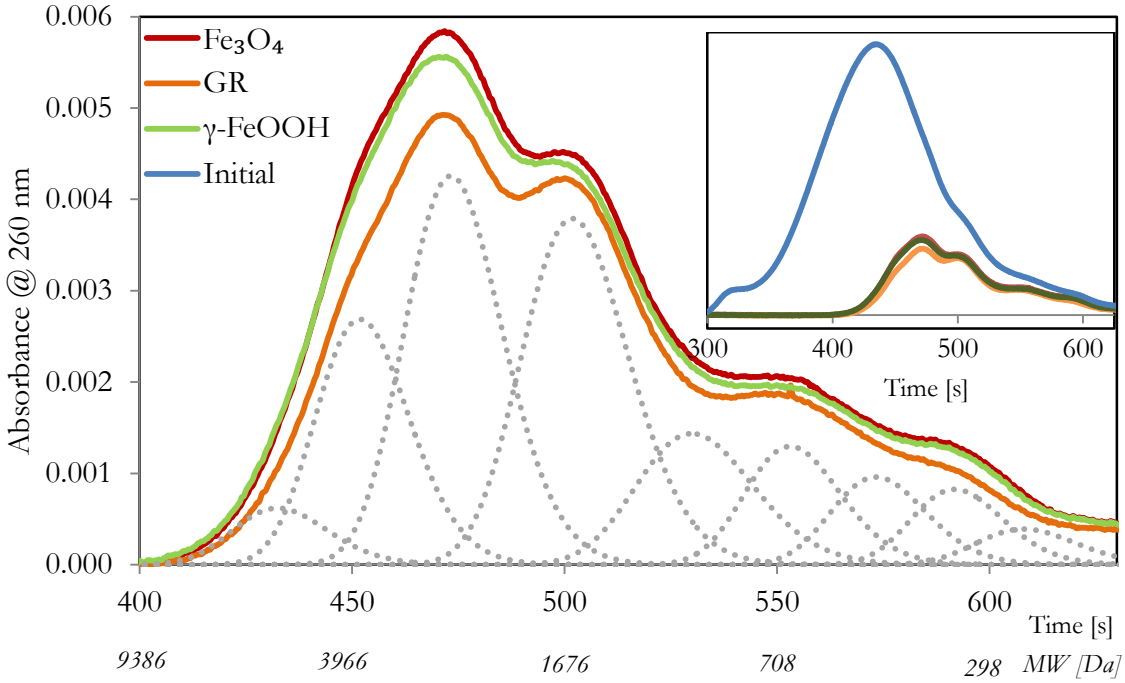

Figure 4-11: DOM HPSEC chromatographs of SP water treated with differing iron speciation. *ML* = 14.4 mg Fe/L. Italicized x-axis values are MW values determined by polysulfonate standard calibration. Dotted lines are resolved peaks by Peakfit® for GR species. Inset: showing relationship to initial DOM chromatograph.

The large MW CNOM fraction (>9000 Da) of the initial NOM (Figure 4-11-inset) was completely removed in all cases. Peakfit® software resolved CNOM chromatographs into twelve smaller peaks, shown as dotted lines for the GR species. Figure 4-12 shows the grouped and normalized total peak areas, divided into six AMW group fractions for each species. Reductions in AMW group fractions show 37% reduction of initial high MW fraction (>1450 MW) with GR, compared to 23% and 21% removal at γ-FeOOH and Fe_3O_4, respectively.

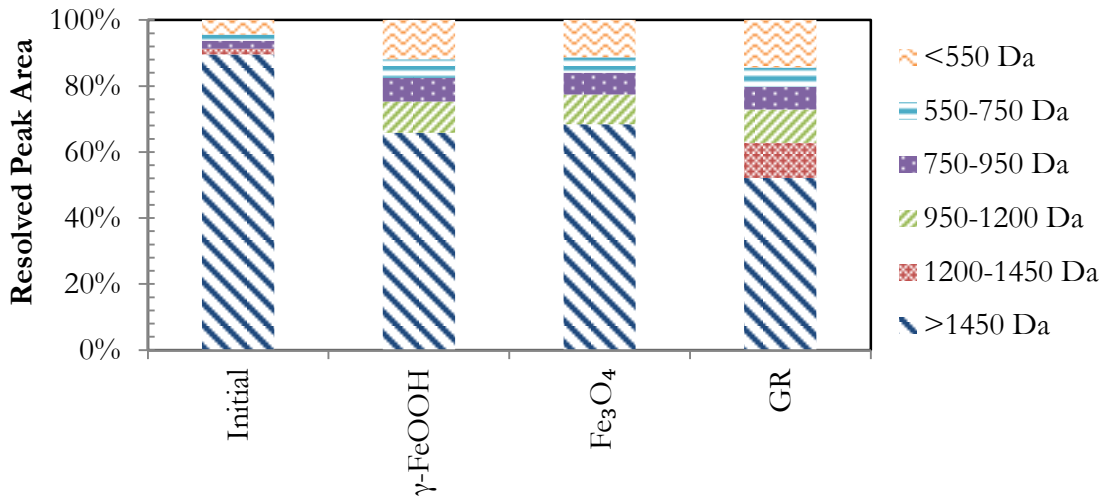

Figure 4-12: HPSEC chromatograph peak-resolved normalized areas for different Fe speciation. *ML*= 14.4 mg Fe/L.

The small, hydrophilic NOM fraction (<550 Da) is known to be less affected by coagulation (Edzwald, 1993), and increased as a percentage of end-products due to the high removal of the large fraction. GR showed slightly higher removal, calculated from total peak area (not AMW relative fraction), which was 29% less than the average of γ-FeOOH and Fe_3O_4 removal. The greater removal of the smaller portion of the CNOM fraction by GR does not completely explain the greater total NOM removal seen earlier, but it does signify that GR has the ability to remove smaller organic compounds, due to either higher charge density increasing coagulation, direct reductive mechanisms, or greater sorption site density.

4.4. Chapter Conclusions

In this chapter, the effect of EC operating parameters on iron speciation and NOM removal was investigated. Several conclusions can be made:

- For Local SP water, low *i* and intermediate *CLR* increased bulk pH slightly, and reduced bulk DO significantly. At lower pH and DO, GR speciation predominated.
- Higher *i* and *CLR* leads to Fe_3O_4 formation, while all other conditions led to increased DO and/or increased pH, with subsequent observation of only γ-FeOOH.
- EC is recommended to be operated, if possible, at conditions (intermediate *CLR*, low *i*) that are favourable to high mass transfer of DO to the cathode surface, leading to a low DO and minimal bulk pH increase. If sufficient DO is consumed in the speciation region near the electrodes, and anodic oxygen evolution does not occur, GR will be generated as a primary EC product, which has general applicability in reduction/sorption processes.
- More work is required elucidating the fraction of NOM removal by synthetic higher purity GR, and determining conditions that allow a more stable GR for pilot work.

5. Iron Speciation in Electrocoagulation

5.1. Chapter Introduction

In Chapter 3, iron was selected as the best candidate for NOM removal, and in Chapter 4, different iron speciation showed different NOM removal capabilities. The low cost and general ubiquity of iron, the current acceptance of iron salt coagulation, and the potential for magnetic separation, combine to make iron an excellent candidate material for EC in general. An idea of the general speciation mechanisms in iron EC would thus be greatly valuable. Iron corrosion products are well documented under typical environmental conditions and time-scales, since passive electrochemical dissolution of iron is one of the most common electrochemical phenomena, the corrosion of steel. However, the electrochemical generation of solid-phase iron oxides and hydroxides in atypical environmental conditions (applied electromotive force and associated current) for use as an engineering material, in water treatment or otherwise, is not as widely documented. There has been recent interest in nano-scale iron oxides, especially of the ferrimagnetic type, for use in medical drug delivery, cancer therapy, and cell targeting (Gupta and Gupta, 2005). Nano-scale magnetite has been used for arsenic remediation, showing that low-gradient magnetic separation (LGMS) is capable of magnetically removing iron particles in the sub-12 nm size, instead of relying on typically unpractical high-gradient magnetic separation (HGMS) (Yavuz et al., 2006). Furthermore, the size of the iron oxide may play a large role in pollutant removal, as smaller coagulants have a higher surface area per unit mass than larger ones, and nano-scale magnetite (<12 nm) can reduce the iron dose necessary for

arsenic removal by orders of magnitude. Understanding iron as an environmental remediation material requires some knowledge of the different iron species that exist. There are seventeen known iron oxides, hydroxides, and oxyhydroxides, referred to as the iron hydr(oxides) (Cornell and Schwertmann, 2000), Table 5-1 lists them.

Table 5-1: Known iron hydr(oxides)

Hydroxides and Oxyhydroxides	Oxides
Goethite, α-FeOOH	Hematite, α-Fe_2O_3
Akaganeite, β-FeOOH	Magnetite, Fe_3O_4
Lepidocrocite, γ-FeOOH	Maghemite, γ-Fe_2O_3
δ-FeOOH, and feroxyhyte, γ'-FeOOH	β-Fe_2O_3
High Pressure FeOOH	ε-Fe_2O_3
Schwertmannite, $Fe_{16}O_{16}(OH)_y(SO_4)_x \cdot nH_2O$	Wüstite, FeO
Ferrihydrite, 5 $Fe_2O_3 \cdot 9\ H_2O$	
Bernalite, $Fe(OH)_3$	
$Fe(OH)_2$	
Green Rusts, $Fe_x^{III}Fe_y^{II}(OH)_{3x+2y-z}(A^-)_z$, A-=$Cl^-$, ½ SO_4^{2-}	

The hydroxides can be dehydroxylated to their respective oxides by rearrangement of cations and loss of OH^-, of which several conditions affect the transformation (time, pH, temperature, pressure, various anions and cations) (Cornell et al., 1989; Ford, 2002). Several iron hydr(oxides) are of greater relevance to this study, because of their possible formation as end-products or intermediates in EC, and are described in more detail.

- Goethite, α-FeOOH, occurs naturally in soil and other low temperature environments. It is one of the most stable, and is either the first iron hydr(oxide) to form, or a typical end product of many transformations. It is often orthorhombic,

antiferromagnetic, and has a yellowish to reddish to dark brown colour. It has been reported in EC (Parga et al., 2005; Gomes et al., 2007; Moreno-Casillas et al., 2007)

- Lepidocrocite, γ-FeOOH, forms naturally in anoxic rusting conditions. It is often orthorhombic, but can consist of layered iron (III) oxide octahedra bonded by hydrogen bonding via hydroxide layers. It is red to reddish brown in colour and antiferromagnetic. It has been reported as a product in EC (Gomes et al., 2007; Timmes et al., 2010)
- Ferrihydrite, 5 $Fe_2O_3 \cdot 9\ H_2O$, also known as amorphous iron oxide, and hydrous ferric oxide, exists only as highly defective nano-crystals, and unless stabilized, transforms into more stable iron hydr(oxides). It consists of hexagonal closely packed anions, but the structure seems to differ from sample to sample. It is reddish brown in colour. Ferrihydrite has been reported as an EC product (Addy, 2009; Balasubramanian et al., 2009; van Genuchten et al., 2011). It is speromagnetic (essentially antiferromagnetic at typical EC conditions).
- Bernalite, $Fe(OH)_3$, is a rare natural mineral, but chemically identical to the monohydrate of iron(III) oxide-hydroxide, $FeO(OH) \cdot H_2O$, . It is often cited as a product of EC (Mollah et al., 2001; Ghernaout et al., 2008), although it is more likely an intermediate in the formation of other iron hydr(oxides). It is weakly ferromagnetic.
- $Fe(OH)_2$ is unstable and does not exist as a mineral in nature, but has been both reported in EC (Mollah et al., 2001) and disputed (Lakshmanan et al., 2009). It most

likely occurs in EC as an intermediate, as it is readily oxidized into green rusts or other iron hydr(oxides). It is antiferromagnetic.

- Green Rusts (GR), are common corrosion products that consist of layers of Fe^{2+}-OH octahedra, and anions are bound between layers to maintain charge neutrality. They are green to bluish green in colour, and have been only described by colour in EC (Moreno et al., 2007). They are either ferromagnetic, ferrimagnetic, or antiferromagnetic, depending on the structure.
- Hematite, α-Fe_2O_3, also known as iron (III) oxide, is the most commonly mined iron ore. It has a hexagonal close packing of anions, and its stability makes it a typical end product of EC (Gomes et al., 2007; Moreno-Casillas et al., 2007). It is red to black in colour. It is essentially antiferromagnetic at normal EC temperatures.
- Magnetite, Fe_3O_4, is a ferrimagnetic iron oxide containing both Fe^{2+} and Fe^{3+}, and can be thought of as $FeO{\cdot}Fe_2O_3$, or one part wüstite, and one part hematite. It has an inverse spinel structure, is black in colour, and is ferrimagnetic. It has been reported as a product in EC (Tsouris et al., 2000; Gomes et al., 2007)
- Maghemite, γ-Fe_2O_3, is a ferrimagnetic iron oxide, with almost the same structure as magnetite, but containing Fe^{2+} deficient sites. It occurs naturally as a weathering or heating product of some iron hydr(oxides). It is grey to brown in colour. It is ferrimagnetic. It has been reported in EC (Gomes et al., 2007; Timmes et al., 2010)

The benefits of electrochemically generated iron oxides over chemically generated ones have been shown to be a more tightly controlled size distribution, less side product generation, and simplicity and cost effectiveness (Cabrera et al., 2008). Indeed, for water treatment in

decentralized settings, the electrochemical method appears to be very appropriate due to the possibility that the only required inputs may be as simple as a sacrificial iron anode, a supporting electrolyte such as common table salt, and electricity. The interest in the ferrimagnetic iron oxides in this study stems from the possibility of avoiding membrane filters, which have historically been identified as a challenge in rural water treatment due to systematic failure from fouling due to high NOM levels (Hong and Elimelech, 1997). The electrochemically generated iron hydr(oxides) in EC have surprisingly only been superficially examined, generally identified as anti-ferromagnetic amorphous iron hydr(oxides), usually a mixture of hydrated Fe_2O_3 and FeOOH, colloquially known as "orange rust" (Sass and Rai, 1987; Golder et al., 2007; Heidmann and Calmano, 2008). The understanding of EC conditions leading to specific speciations would thus be extremely valuable, but requires an understanding of the mechanisms of formation, since iron has two common oxidation states. The electrochemical dissolution of iron has been suggested by two mechanisms (Mollah et al., 2001):

Mechanism 1:

$$\text{Anode: } 4\ Fe \rightleftharpoons 4\ Fe^{2+} + 8\ e^- \quad (5\text{-}1)$$

$$\text{Cathode: } 8\ H^+ + 8\ e^- \rightleftharpoons 4\ H_2 \quad (5\text{-}2)$$

$$\text{Electrolyte: } 4\ Fe^{2+} + 10\ H_2O + O_2 \rightleftharpoons 4\ Fe(OH)_3 + 8\ H^+ \quad (5\text{-}3)$$

Mechanism 2:

$$\text{Anode: } Fe \rightleftharpoons Fe^{2+} + 2\ e^- \text{ (and possibly } Fe^{2+} \rightleftharpoons Fe^{3+} + 1\ e^-) \quad (5\text{-}4)$$

$$\text{Cathode: } 2\ H_2O + 2\ e^- \rightleftharpoons H_2 + 2\ OH^- \quad (5\text{-}5)$$

$$\text{Electrolyte: } Fe^{2+} + 2\ OH^- \rightleftharpoons Fe(OH)_2 \text{ (possibly } Fe^{3+} + 3\ OH^- \rightleftharpoons Fe(OH)_3) \quad (5\text{-}6)$$

Also, oxygen gas evolution can occur as a parasitic reaction on the anode:

$$\text{Anode: } H_2O \rightleftharpoons \tfrac{1}{2}\, O_2 + 2\, H^+ + 2\, e^- \qquad (5\text{-}7)$$

Recent evidence (Lakshmanan et al., 2009) suggests that formation of $Fe(OH)_2$ (mechanism 2) does not occur, and that $Fe(OH)_3$ is produced by way of Fe^{2+} formation at the anode, followed by a highly pH-dependant oxidation by dissolved oxygen (DO). Other authors (Franger et al., 2004) suggest a different anodic reaction to direct γ-FeOOH, as:

$$\text{Anode: } Fe + 3\, OH^- \rightleftharpoons \gamma\text{-}FeOOH + H_2O + 3\, e^- \qquad (5\text{-}8)$$

High φ for χ=2 in Chapter 3 suggests that either reaction (5-1) or (5-4) by the two electrode step, and not (5-8), also seen in several other EC studies (Lakshmanan et al., 2009; Tanneru et al., 2012). Low φ found at higher i suggests reaction (5-7) does indeed take place, except when NaCl is present. Other studies have only hinted at the parameters affecting the electrochemical generation of differing iron species, including pH (Lakshmanan et al., 2009), i (Heidmann and Calmano, 2007; Addy, 2009; Ibrahim et al., 2009), inter-electrode gap (Franger et al., 2004), temperature (Tsouris et al., 2000), DO (Pascal et al., 1999), and supporting electrolyte (Refait et al., 1997; Liu et al., 1998). No study has done a comparison of factors that affect the electrochemical production of EC iron hydr(oxides). Of specific interest to explain the results from earlier chapters, i and solute composition are particularly significant to this study. Characterizing the differing EC species is possible with novel techniques, such as: *in-situ* Raman (described in Chapter 4), aqueous X-ray diffraction

(XRD), scanning electron microscopy (SEM), and cryogenic transmission electron microscopy (cryo-TEM). The goal of this chapter was to use these techniques to understand the impact of EC parameters , specifically *i* and solute type and concentration, on speciation.

5.2. Materials and Methods

5.2.1. Synthetic Water

Synthetic water was composed of Milli-Q deionized water and differing concentrations of Na_2SO_4 and NaCl (Laboratory Grade, Fisher Scientific). The water was deoxygenated by bubbling N_2 (*g*) (Praxair, 99.99%) through a diffuser for 6 hr. For cryo-TEM analysis, poly-vinyl acid (PVA) (Sigma Aldrich, 31 000-50 000 MW) was added to prevent agglomeration, in a concentration of 1 g/L, heated to 60ºC, and mixed for 24 hr. Solution pH was adjusted by NaOH or H_2SO_4 (Laboratory Grade, Fisher Scientific) to attain a pH of 7.00 ± 0.05. Batches were made as needed.

5.2.1. Electrocoagulation

A custom 50 mL parallel plate electrochemical batch reactor was manufactured from acrylic for EC, similar to that described in Chapter 4. The anode was a 99.9% pure iron foil of 1 mm thickness (Goodfellow), precision cut to a nominal area of 4.0 cm^2, connected via glass-insulated copper wire. The cathode was a 20 mm x 20 mm 99.99% pure platinum foil of 0.2 mm thickness (Goodfellow), the inter-electrode gap was 10 mm. A DC power supply (Instek PSP-603) supplied DC current in galvanostatic mode. Before each experiment,

electrodes were wet-polished with P200 SiC, P1500 SiC, and emery paper, rinsed with 1% sulphuric acid, and double rinsed with Milli-Q water. Electrolysis took place directly after polishing to avoid surface film formation. Two EC parameters, i and solute type and concentration were investigated as to their impact on φ and speciation. Three i values (5, 25, 125 mA/cm^2) and two solutes, Na_2SO_4 (3, 9 mM), and NaCl (0, 0.3, 1, 3 mM) were selected to cover a range seen previously to have an impact in previous chapters. Samples for φ investigation were acidified with 1 mL of a 3:1 HCl to HNO_3 (Laboratory grade, Fisher Scientific) solution of *aqua regia,* and a further 10 mL of 5% *aqua regia* solution was used to rinse the electrodes of remaining iron precipitate. The EC reactor was operated in a deoxygenated glove-box, supplied with N_2 (*g*) (Praxair, 99.99%), with aliquot samples being withdrawn and sealed in an air-tight, darkened glass vial for XRD and SEM analysis. For φ determination, Faraday's Law with z=2 was assumed, as described in equation (2-4). Metal concentrations were measured by inductively coupled plasma optical emission spectroscopy (ICP-OES) with a wavelength of 238.204 nm for iron detection (PerkinElmer Optima 7300 DV). Since all waters were deoxygenated, the effect of DO was not studied here. Each experiment was performed four times identically, twice for φ determination, and twice for speciation analysis. Standard error is shown as vertical error bars in all figures.

5.2.2. *in-situ* Raman Micro-Reactor

A unique micro-reactor was developed to obtain better resolution than that in Chapter 4. An acrylic reactor (Figure 5-1) was drilled to just accommodate the Raman wet-objective. A 1 mm diameter hole was drilled in the center of the reactor, and a 12.7 mm diameter Au

mirror (Thorlabs Inc.) was fixed underneath to capture reflected Raman scattering spectra. A 1 mm diameter, 1 mm height hole was drilled from both sides to accommodate an anode (1 mm diameter x 20 mm length, 99.99% Fe, Goodfellow), and cathode (1 mm diameter x 20 mm length, 99.99% Pt, Goodfellow), and a third hole drilled to accommodate a 1/32″ tube to maintain a N_2 (*g*) blanket (Praxair, 99.99%) and oxygen-free solution. The total solution volume was approximately 1 mL. The volume of the speciation region between the electrodes was ~1 µL, meaning that almost all generated particles accumulated in the laser focus plane, allowing faster spectra capture to characterize species transformations.

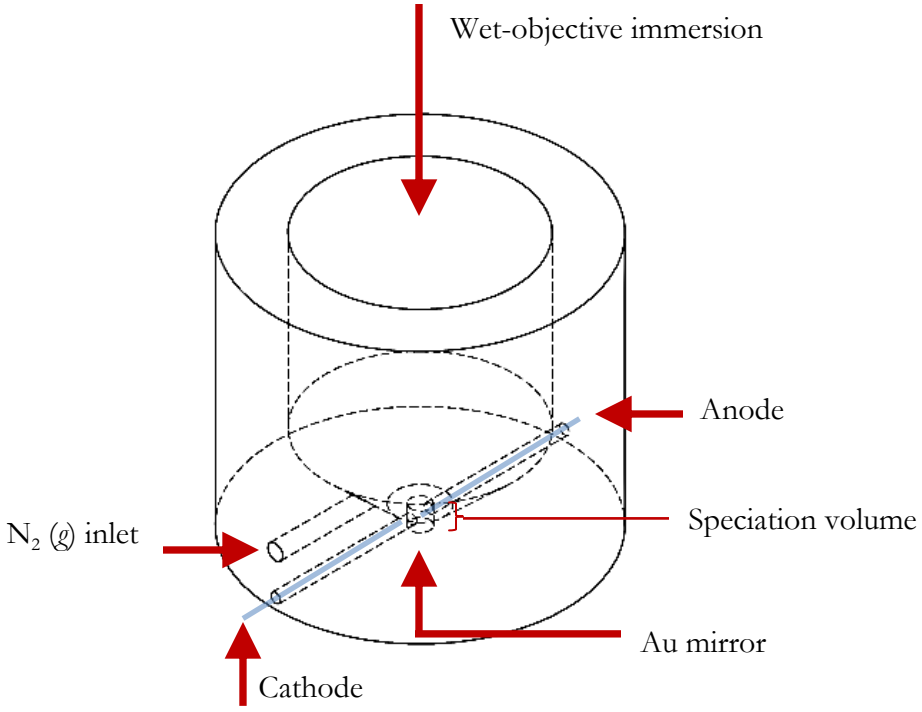

Figure 5-1: micro-reactor for *in-situ* Raman

A Raman spectroscopy system (InVia, Renishaw) equipped with a 785 nm laser and 160 mW (at 1% = 1.6 mW) excitation laser was employed with a 40x wet-objective (Leica HCX APO 40x) immersed directly above the speciation volume. To reduce collection times, spectra were obtained only for the iron hydr(oxide) fingerprint region from 200 to 1400 cm^{-1} and sometimes from 200 to 1200 cm^{-1}. Raman spectra are presented as raw data, normalized over total peak intensity, interference from fluorescent lighting and sulfate peaks were not removed. The total time between species generation and characterization by *in-situ* Raman in the micro-reactor was approximately 15s, far faster than the 60s or longer required in Chapter 4.

5.2.3. Aqueous XRD

A deoxygenated aliquot from the EC reactor was analyzed using capillary aqueous XRD (Bruker D8 - GADDS). This allowed the sample crystals to remain hydrated in solution, but did allow exposure to air, species may have been oxidized to more stable species. The total time between species generation and XRD characterization was 24-48 hr, allowing for determination of bulk end products only, not intermediates.

5.2.4. SEM

Samples were withdrawn from the aliquot and filtered in an oxygen-free glove box on a 0.22 μm PTFE membrane filter. To prevent complete dehydration, only 90% of the liquid was

filtered off. The remaining sample was placed in an oxygen-free flask, immersed in N_2 (*l*) at 77 K and vacuum pumped to sublimate the remaining liquid from the sample and preserve crystal morphology. The samples were kept under N_2 (*l*) until placement in the SEM (Hitachi S-2300) unit. The samples were covered with N_2 (*l*) to minimize exposure to air during vacuum generation. The total time between species generation and vitrification at cryogenic temperatures was approximately 3-5 min.

5.2.5. Cryo-TEM

A novel methodology to determine species structure and size directly after generation was developed to maintain the aqueous composition of the hydr(oxides) with characterization on the order of seconds. The EC micro-reactor system was transported directly adjacent to a cryogenic vitrification unit (FEI Tecnai Vitrobot) to minimize time between sample generation and freezing in N_2 (*l*). Approximately 5 μL was pipetted from the liquid volume during electrolysis in the micro-reactor, and injected into the cryogenic vitrification unit with a blot time of 2s. The samples were then inserted under N_2 (*l*) into a cryogenic-equipped TEM (FEI Tecnai G2 200 kV LaB_6) for characterization. To prevent sample damage from the electron source, the beam was focused ~ 500 nm from the desired image centre, and only the perimeter of this image was analyzed. Otherwise, the irradiated sample was heated to the point of melting, shifting the nanoparticles significantly, and possibly changing their morphology. While this methodology was fast, it had two disadvantages: Firstly, it led to approximately ten-fold less maximum resolution than non-cryo TEM due to risk of sample

damage at higher magnification, and secondly, it led to very dilute samples, meaning accurate particle size distributions were not feasible. The total time between species generation and vitrification at cryogenic temperatures was between 5-30 s.

5.3. Results and Discussion

5.3.1. Effect of Current Density

Figure 5-2 shows the results of φ at 5, 25, and 125 mA/cm^2, for a solution of 3 mM Na_2SO_4. A slope of unity signifies a φ=1 for z=2, and linear regressions for the three i values (dashed lines) represent the average φ.

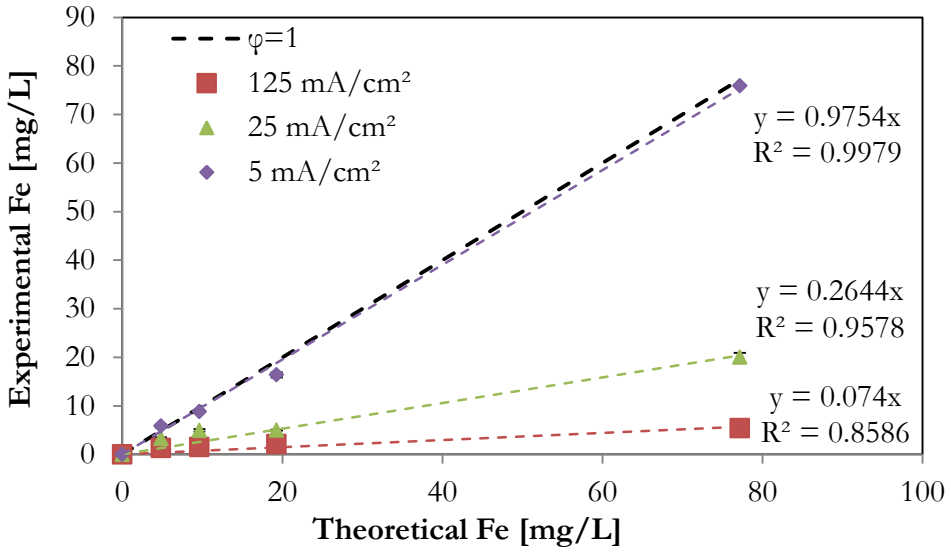

Figure 5-2: Impact of i on φ for [Na_2SO_4]=3 mM, [NaCl] = 0 mM, large dashed line is φ=1 for z=2, thin dashed lines are linear regressions of each i

At i=5 mA/cm^2, φ=0.97, suggesting that only reaction (5-1) occurs, without any parasitic oxygen evolution. At i=125 mA/cm^2, φ=0.07, suggesting that mostly reaction (5-7) occurs,

visually confirmed by oxygen bubbles coming from the anode, and very little colouration in the water after electrolysis. Since there was no NaCl in the solution, anodic Cl_2 (*g*) evolution was impossible. Predictably, the intermediate i=25 mA/cm^2 gave an intermediate φ=0.24, suggesting that both reactions (5-1) and (5-7) occurred, this was a similar φ result to corresponding i seen previously in Chapter 3. The impact of i on speciation followed logically, after determining the effect of DO on speciation in local natural water in Chapter 4. Since the initial water here was deoxygenated, low φ led to oxygen evolution by reaction (5-7) and thus greater DO, which led to Fe^{2+} oxidation to Fe^{3+} via mechanism 1, or more specifically, via reaction (4-3). This led to the typical ferric "orange rust" in EC, seen by the amorphous XRD pattern in Figure 5-3 for 25 and 125 mA/cm^2.

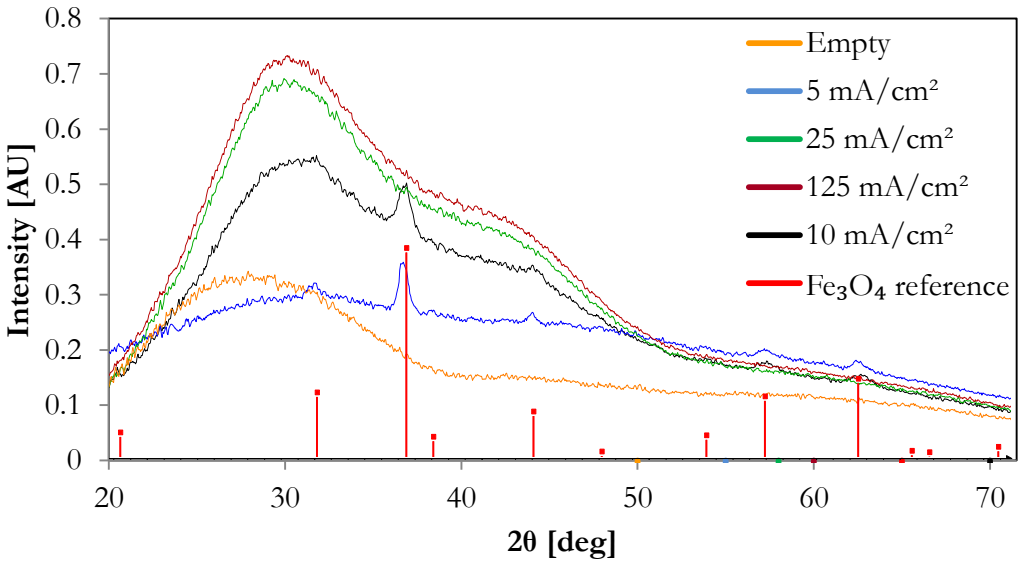

Figure 5-3: *in-situ* XRD showing effect of *i* on speciation for [Na_2SO_4]=3 mM, [NaCl] = 0 mM

For both 25 mA/cm^2 and 125 mA/cm^2, no Fe_3O_4 signal at all was observed in the final product, and only broad peaks demonstrating the poor crystallinity of the "orange rust", confirming earlier reports in iron EC (Sass and Rai, 1987; Golder et al., 2007; Heidmann and Calmano, 2008). 5 mA/cm^2 showed a distinct Fe_3O_4 XRD pattern, matching reference peak location for Fe_3O_4 exactly. This confirmed earlier findings of Fe_3O_4 at lower *i* and *CLR* in Chapter 4 in local natural water. Very little, if any at all, "orange rust" peak is seen in the diffraction pattern, suggesting at least superficially, a somewhat pure Fe_3O_4 substance. To test the ability of aqueous XRD to detect species mixtures, a sample of 10 mA/cm^2 showed broad peaks for both amorphous "orange rust" and narrow peaks for Fe_3O_4, furthering evidence that at low *i* (5 mA/cm^2), a high purity Fe_3O_4 compound results. Unfortunately, the gold-standard Mössbauer spectroscopy was not available for mixture ratio quantification. The amorphous ferric "orange rust" was found by *in-situ* Raman spectroscopy to be γ-FeOOH as in Chapter 4, evidence and transformations are discussed later. The ferric "orange rust" was further characterized by SEM and cryo-TEM. Figure 5-4 shows SEM evidence of agglomerations of ~100-200 nm spherical and platy particles (Figure 5-4A) and ~20-50 nm spherical particles at higher resolution (Figure 5-4B), which occurred for both 25 mA/cm^2 and 125 mA/cm^2.

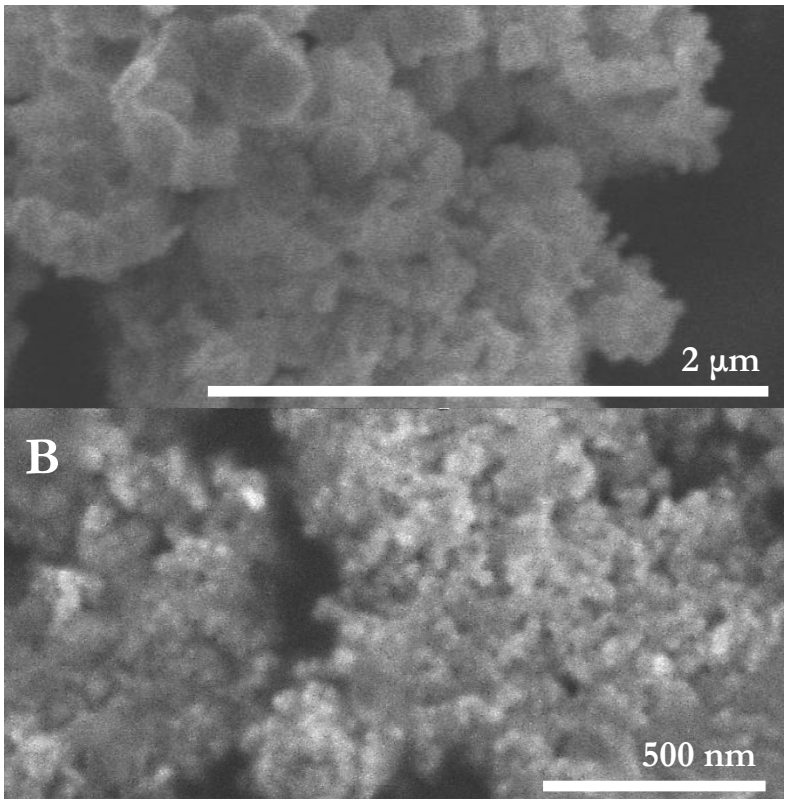

Figure 5-4: SEM showing ~50 nm agglomerations, i = 125 mA/cm^2, [Na_2SO_4]=3 mM, [NaCl] = 0 mM

These agglomerations, which act as the high surface area sorbing sites for NOM and other pollutants in EC, were part of larger floc particles, usually of 3-10 μm size. The small amorphous "orange rust" particles have been identified at similar sizes as EC products (Tsouris et al., 2000, Yang and Tsai, 2006, Addy, 2009). It was assumed that Figure 5-4 showed poorly crystalline γ-FeOOH, although α-Fe_2O_3, ferrihydrite, and Fe_3O_4 can have similar size and shape (Cornell and Schwertmann, 2003). Since SEM required a necessary dehydration step, cryo-TEM was used for higher resolution imaging of the "orange rust" without dehydration, seen in Figure 5-5:

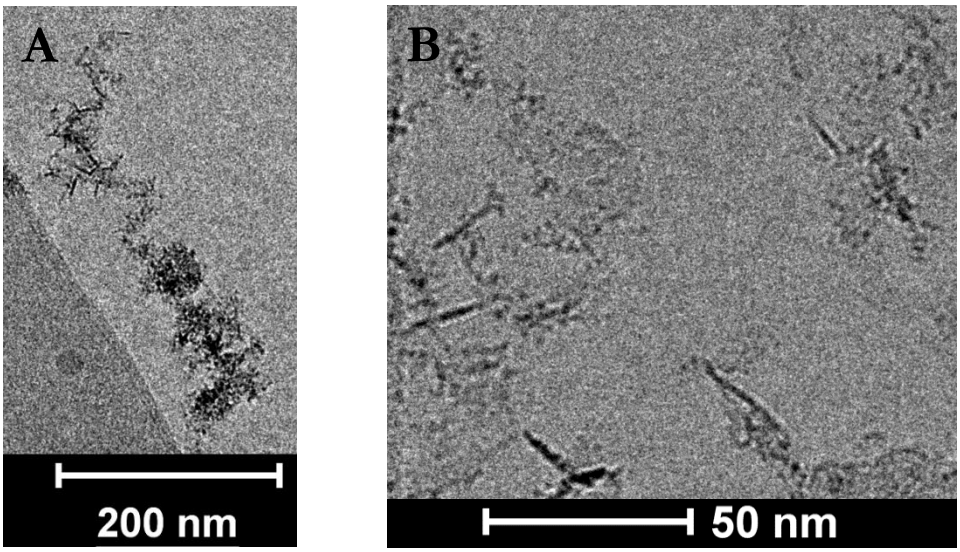

Figure 5-5: cryo-TEM showing 10-20 nm needle-like shape, i = 125 mA/cm^2, [Na_2SO_4]=3 mM, [NaCl] = 0 mM, A) ~300 nm aggregate, B) individual crystals

Cryo-TEM showed ~200 nm aggregates of smaller crystals, seen in Figure 5-5A. This could be an intermediate in the formation of the agglomerated sphere-like particles of similar size seen in Figure 5-4. Figure 5-5B shows 10-30 nm needles, appearing to originate from even smaller 1-5 nm acicular particles. Needles and laths are common in oxide hydroxides, including γ-FeOOH, and they have been shown to grow from 1-5 nm spheres of ferrihydrite elsewhere (Murphy et al., 1976). Elongated needles of γ-FeOOH in spherulites shapes (Figure 5-5A) have also been observed when crystallization is retarded by organic compounds (Brauer, 1982), such as the PVA used in cryo-TEM tests. These results may provide some evidence that 1-5 nm particles of ferrihydrite are a crucial intermediate in EC, as suggested by Addy (2009). This is possible, since ferrihydrite is thermodynamically unstable, and generally transforms to γ-FeOOH, α-FeOOH, or α-Fe_2O_3 in aqueous solution

(Cornell and Schwertmann, 2003). While size and shape of the "orange rust" compounds are not definitive of speciation, they can assist in explaining differing NOM removals found at differing EC operating parameters seen in Chapters 3 and 4. At i=5 mA/cm^2, Fe_3O_4 crystals were seen by SEM, shown in Figure 5-6.

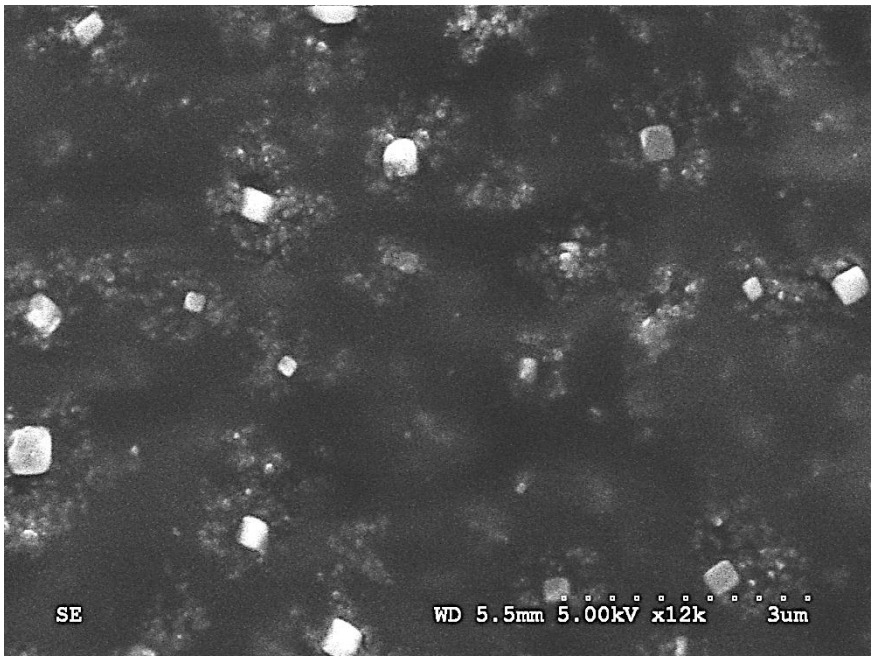

Figure 5-6: SEM showing cubic Fe_3O_4, i = 5 mA/cm^2, [Na_2SO_4]=3 mM, [NaCl] = 0 mM

Fe_3O_4 crystals synthesized chemically under controlled conditions in aqueous systems at temperatures < 100ºC are either rounded, cubic, or octahedral in shape of approximately 100-300 nm in size (Taylor and Schwertmann, 1974; Regazzoni et al., 1981). Fe_3O_4 crystals were seen here by SEM in a range of 100-500 nm, often flanked by smaller agglomerates (~150 nm) of either Fe_3O_4 particles, "orange rust", or intermediates such as ferrihydrite.

This may suggest that impure Fe_3O_4 is initially generated, contrary to previous XRD findings, and that the larger Fe_3O_4 crystals may have absorbed all of the emitted x-rays, preventing identification of the other compounds. Cryo-TEM experiments showed less agglomeration of Fe_3O_4, showing 30-80 nm cubic (or possibly octahedral) particles at i=5 mA/cm^2, seen in Figure 5-7. Note the 10 nm layer of PVA encapsulating the crystals, which temporarily prevented agglomeration before vitrification.

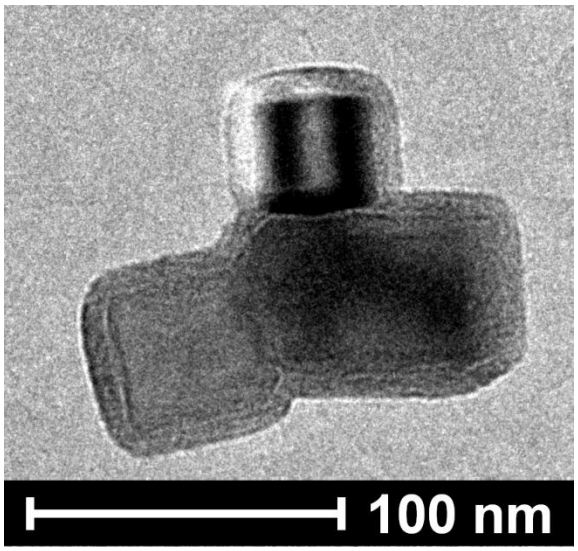

Figure 5-7: cryo-TEM showing cubic or octahedral Fe_3O_4 encapsulated in PVA, i = 5 mA/cm^2, [Na_2SO_4]=3 mM, [NaCl] = 0 mM

Interestingly, cubic/octahedral Fe_3O_4 crystals are usually instead of spherical particles at a higher pH (pH 12) (Sugimoto and Matijevic, 1980), indicating that cubic Fe_3O_4 crystals were not likely formed in the acidic region near the anode, but more likely in the alkaline conditions closer to the cathode, as noted in Chapter 4. Polarization studies would have been helpful to determine why the increased i led to decreased φ in chloride free medium.

Unfortunately, polarization studies could not be performed with a three-electrode cell since the conductivity of the chloride free water was too low to gain meaningful data, and required high E_{cell} (60 V) to obtain the *i* values here, while the maximum E_{cell} available to the author with a three-electrode potentiostatic polarization cell was 10 VDC. Still, conceptual conclusions can be drawn without the knowledge of anodic potential (E_a). Generally speaking, the higher the *i*, the greater the anodic potential, E_a. As E_a increased, it approached the thermodynamic possibility of oxide formation, as shown in the Pourbaix diagram of Figure 5-8 increasing *i* are shown as arbitrary increasingly larger circles:

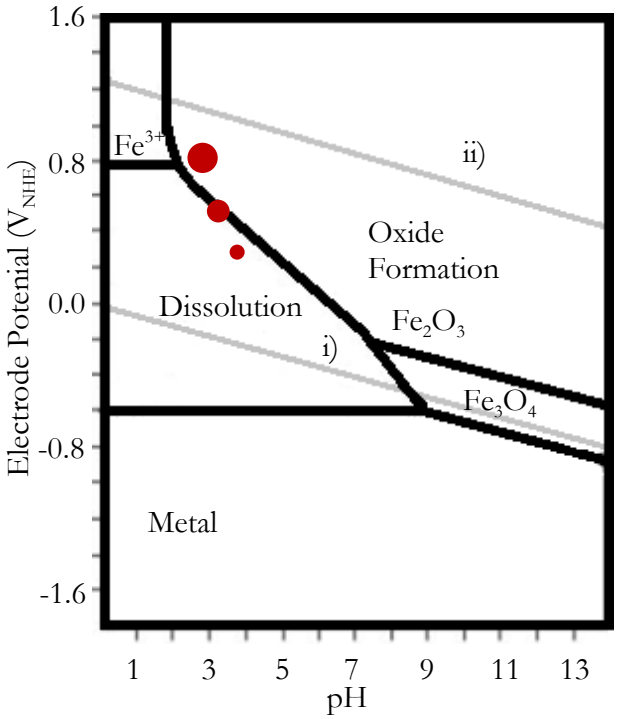

Figure 5-8: Pourbaix diagram for iron water system at 25°C and dissolved iron concentration of 10^{-6} M. Filled circles are arbitrary possible E_a at differing *i*, larger circles indicate larger *i*. Lighter coloured lines are i) water reduction to H_2 and ii) water oxidation to O_2

At lower E_a (i=5 mA/cm^2), thermodynamic speciation likely fell into the dissolution region, demonstrated by $\varphi \sim 1$ for z=2. At greater E_a (i=25, 125 mA/cm^2), oxide formation likely took place, which became thermodynamically possible. Also, at higher i, pH likely decreased to a greater extent near the anode as a higher concentration of Fe^{2+} rapidly hydrolyzed (as described in Chapter 4). The commonly proposed passivation mechanism generally shows an insulating layer of Fe_2O_3 or Fe_3O_4 as an end product of passivation (Bessone et al., 1977):

$$\text{Anode: } Fe(s)[Fe(OH)_3]_{ads} \rightleftharpoons Fe_2O_3 + 3\,H^+ + 3\,e^- \quad (5\text{-}9)$$

$$\text{Anode: } Fe_2O_3 + [Fe(OH)_2]_{ads} \rightleftharpoons Fe_3O_4 + H_2O \quad (5\text{-}10)$$

This passivation layer prevents further Fe^{2+} dissolution, causing oxygen evolution by reaction (5-7) on the Fe_2O_3 or Fe_3O_4 layers, as observed experimentally. Thus, the greater i causes passivation and oxygen evolution, which explains the decrease in φ. Interestingly, the passivation layer seen here for iron EC did not keep growing in thickness, noted by the absence of the typical E_{cell} linear ramp seen in passivating aluminum EC (Mechelhoff, 2009), where a growing passivation layer was found by atomic force microscopy. Likewise, φ was not seen to decrease with greater electrolysis time, as noted by Addy (2009). This suggests relatively slow oxide film growth kinetics, and can be explained due to the fact that the thermodynamic possibility of passivation (Figure 5-8) does not necessarily mean significant kinetic growth of the oxide layer, since the passivation growth rate of iron in neutral solutions is directly dependent on anodic potential (Bockris et al., 1971). . However, tests at

extended electrolysis times might show a decreasing trend in φ, since some growth of the oxide layer over time is likely. This might suggest the periodic addition of chloride for "cleaning" of an EC system during normal operation in very low chloride (or other halide) waters.

5.3.2. Effect of Solute

Solute had a notable impact on φ, the addition of 0.3 mM NaCl increased φ from 0.26 at 25 mA/cm^2 without NaCl present, to φ =0.96. Likewise, φ increased from 0.074 at 125 mA/cm^2 without NaCl present, to φ =0.76 (Figure 5-9A). The addition of 1.0 mM NaCl further increased dissolution to an average of φ =0.90. (Figure 5-9B).

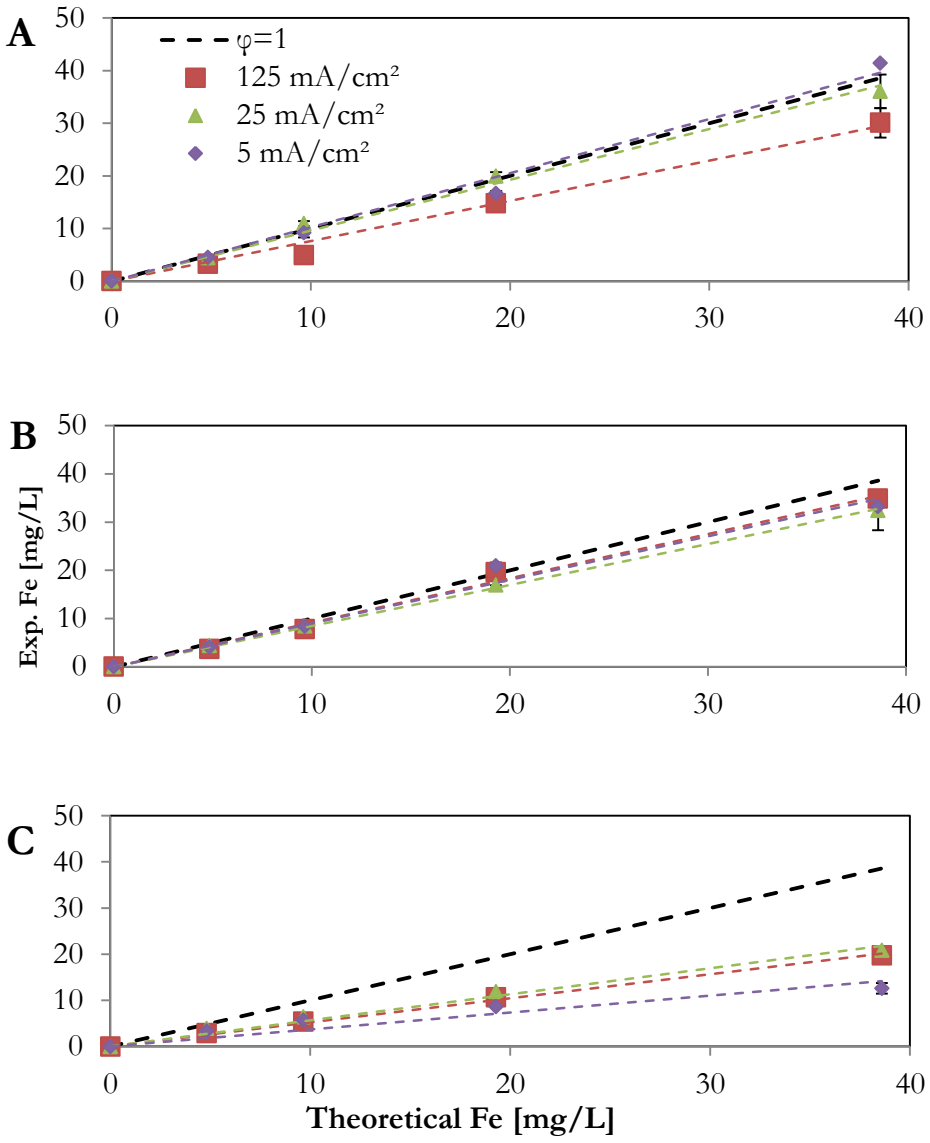

Figure 5-9: φ determination for differing *i*, solute, and concentration, A) [Na_2SO_4]=3 mM, [NaCl] = 0.3 mM B) [Na_2SO_4]=3 mM, [NaCl] = 1 mM, C) [Na_2SO_4]=9 mM, [NaCl] = 3 mM, large dashed line is φ=1 for z=2, thin dashed lines are linear regressions of each *i*

The increase in φ with the addition of NaCl was very likely the result of pitting corrosion. Without going into great detail, pitting corrosion is an incompletely understood

phenomenon that locally dissolves the passivation layer in dispersed pits (approximately 10 nm - 1 mm in diameter), and usually involves halide anions such as chloride. It is autocatalytic; initial dissolution of the passivation layer stimulates further dissolution inside pits, causing hydrolysis and localized H^+ release, drawing more Cl^- into the pit, further driving dissolution and pit growth. A significant voltage decrease did not occur under pitting corrosion conditions, suggesting that metastable pit growth was occurring as noted elsewhere for aluminum EC (Mechelhoff, 2009); as soon as pits formed they were repassivated. To determine if the ratio of sulphate to chloride anions was more important than absolute value in EC passivation, both NaCl and Na_2SO_4 concentrations were increased three fold to determine impact on φ. Figure 5-9C shows a decreased φ of average φ=0.48 for i=5-125 mA/cm^2, suggesting that the absolute sulphate concentration was more important than the anion ratio for passivation. This likely occurred since sulphate is a known pitting corrosion inhibitor (Lee and Pyun, 2000), and a higher concentration would lead to greater anodic surface coverage, regardless of chloride concentration. Interestingly, once pitting corrosion began, the effect of nominal i was less pronounced than seen previously without NaCl, as seen in Figure 5-9A. Since dissolution took place inside pits instead of homogenously across the surface, nominal surface area, and thus i, was less significant in affecting φ. Statistically, the effect of i on φ at increased NaCl concentrations (Figure 5-9B) was not significant (95% confidence).

The impact of solute type and concentration on speciation followed closely that of the impact on φ, similar to previous results without the pitting promoter of NaCl. Species were identified as γ-FeOOH and Fe_3O_4 as before, impacted directly by φ. When φ was 0.95 or

above, end products were Fe_3O_4, without amorphous XRD "orange rust" patterns, as observed earlier. However, Fe_3O_4 generation was possible at increased *i* due to chloride presence and pitting corrosion. Some evidence from cryo-TEM shows smaller Fe_3O_4 generation at higher *i*, showing spherical crystals as small as 15 nm (Figure 5-10), smaller than any Fe_3O_4 crystals observed at lower *i*, which would match findings of smaller electrochemically generated nanoparticles at higher *i* (Pascal et al., 1999), albeit in organic medium. Unfortunately the low concentration of PVA was not able to isolate the particles for a longer time period, and agglomeration is readily seen.

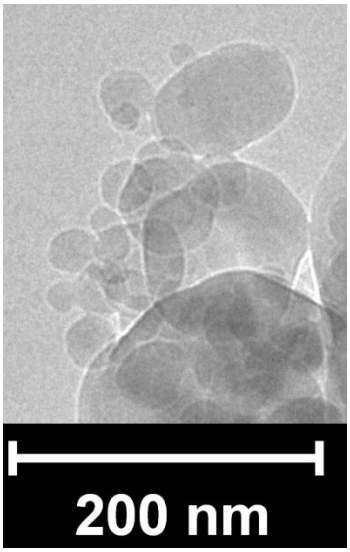

Figure 5-10: cryo-TEM showing acicular Fe_3O_4 crystals from 15-200 nm, *i* = 125 mA/cm^2, [Na_2SO_4]=3 mM, [NaCl] = 1 mM

5.3.3. Species Transformations

At *i*=25 and 125 mA/cm^2 for [Na_2SO_4]=3 mM, [NaCl] = 0.3, 1 mM, crystals of unstable intermediate GR was observed by *in-situ* Raman, SEM (Figure 5-11) and cryo-TEM. Arrows in Figure 5-11 indicate definitive orthogonal hexagonal morphology.

Figure 5-11: SEM showing ~100 nm GR orthogonal hexagonal plates, *i* = 25 mA/cm^2, [Na_2SO_4]=3 mM, [NaCl] = 1 mM

SEM captured orthogonal hexagonal plates, typical of GR (McGill et al., 1976; Refait et al., 1998; Refait et al., 2003), and only seen elsewhere at elevated temperatures hydrothermally produced hematite (Cornell and Schwertmann, 2003). The hexagonal morphology suggests EC products of hexagonal GR2 (sulphate) instead of the rhombohedral GR1 (chloride) (Génin et al., 2001). GR species were seen only as intermediates, as in Chapter 4, and as in previous experiments, end products were either γ-FeOOH or Fe_3O_4. GR is known to be the

intermediate between these two products, with a slower oxidation producing Fe_3O_4 and faster oxidation producing γ-FeOOH (Misawa et al., 1974), and a higher pH, higher *T*, and higher [Fe^{2+}] favouring Fe_3O_4 (Cornell and Schwertmann, 2003). This transformation was observed by *in-situ* Raman (Figure 5-12) over the course of several minutes, GR Raman intensity diminishes while Fe_3O_4 increases.

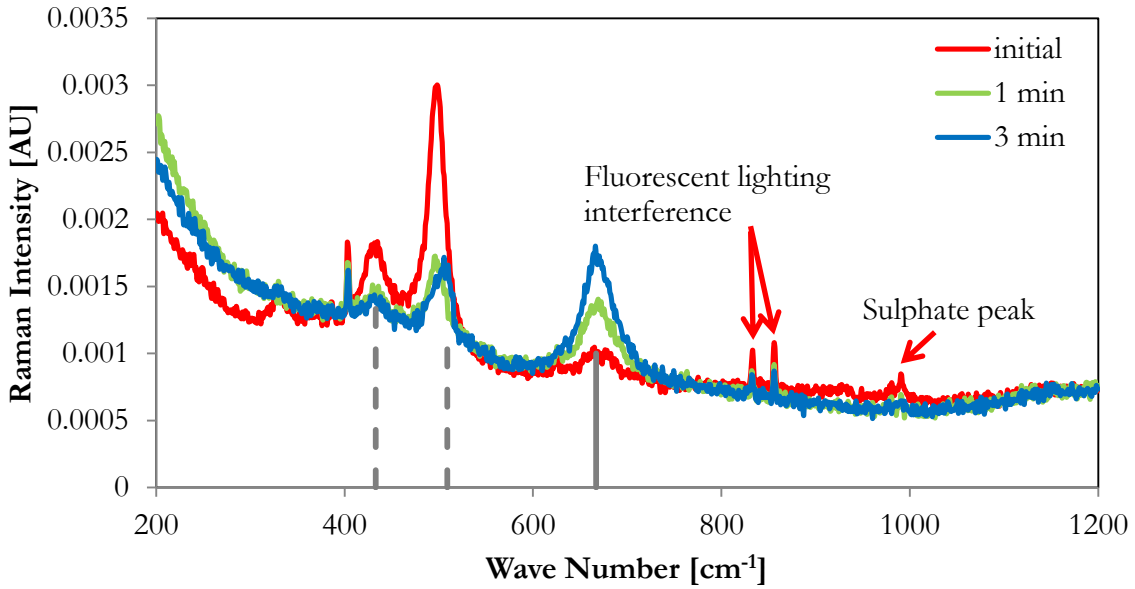

Figure 5-12: *in-situ* Raman showing GR transformation to Fe_3O_4, dashed vertical line is reference peak for GR (Bonin et al., 2000), solid vertical line is reference peak for Fe_3O_4 (Odziemkowski et al., 1994), *i* = 25 mA/cm^2, [Na_2SO_4]=3 mM, [NaCl] = 1 mM

The above spectra are likely the first Raman series showing direct transformation of GR to Fe_3O_4. The peak at 319 is a sub-peak of Fe_3O_4 (Odziemkowski et al., 1994), and the peak at 990 was not identified in the literature. The transformation was also captured by cryo-TEM, which is also likely the first TEM image of GR transformation to Fe_3O_4, where a 180 nm

hexagonal crystal is agglomerating, and likely transforming, onto a 400 nm Fe_3O_4 particle in Figure 5-13.

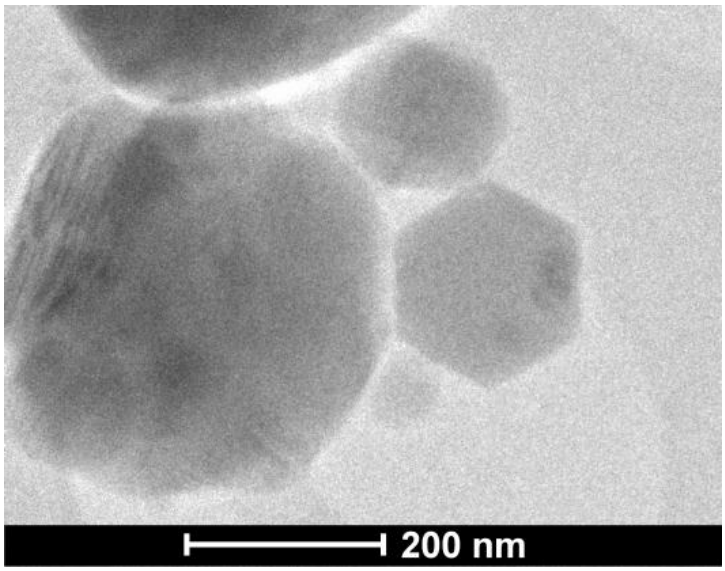

Figure 5-13: cryo-TEM showing possible GR transformation to Fe_3O_4

The exact mechanism of GR to Fe_3O_4 transformation is not known, but it is known that slow oxidation is necessary (Cornell and Schwertmann, 2003), which would take place only when minimal DO is present in solution at high φ, explaining why Fe_3O_4 was only found either at low i in the absence of chloride, or high i with chloride present. GR usually has a Fe^{2+}/Fe^{3+} ratio of between 1:1 and 2:1 (LeGrand et al., 2001), while Fe_3O_4 has a stoichiometric ratio of 1:2. Thus, Fe_3O_4 still requires some amount of GR Fe^{2+} oxidation for transformation to take place, regardless of the Fe^{2+}/Fe^{3+} ratio of GR. The source of the additional Fe^{3+} required may be either due to small amounts of anodic oxidation of Fe^{2+}, the possibility of anodic generation of Fe^{3+}, or small amounts of oxidation by DO from anodic

O_2 generated by reaction (5-7) since φ was not exactly unity. Regardless of the source of Fe^{3+}, it would have rapidly hydrolyzed to form an iron (III) hydr(oxide), and oxidation of Fe^{2+} is known to be autocatalytic in the presence of iron (III) hydr(oxides) (Tamura et al., 1980; Williams and Scherer, 2004). Thus, Fe_3O_4 formation likely required some amount of iron (III) hydroxides present, suggesting that rarely an entirely pure Fe_3O_4 is formed. However, γ-FeOOH is known to transform to Fe_3O_4 in the presence of Fe^{2+} (Belleville et al., 1992; Pedersen et al., 2005), which could explain the apparently pure Fe_3O_4 seen by XRD. This could also allow the exciting possibility of magnetic separation of EC products. This process has been termed "magneto-EC", and is the current subject of a $1M U.S. Department of Energy research proposal (DE-FOA-0000560) and UBC collaboration with Lawrence Berkeley National Laboratory and the University of California, Berkeley.

The final EC species transformation seen was γ-FeOOH aged for seven days in solution, seen to transform to α-FeOOH, shown in Figure 5-14. A pure α-FeOOH substance is doubted, since γ-FeOOH aging takes over thirty days at 293 K to reach full conversion to α-FeOOH (Cornell and Schwertmann, 2003). as Also seen was a small peak at ~ 245 cm^{-1} belonging to α-FeOOH after aging. This aging process is important for adsorption studies, since NOM or other pollutants (e.g., heavy metals) could be released upon aging, suggesting pH adjustment or faster drying may be a necessary step for EC sludge disposal.

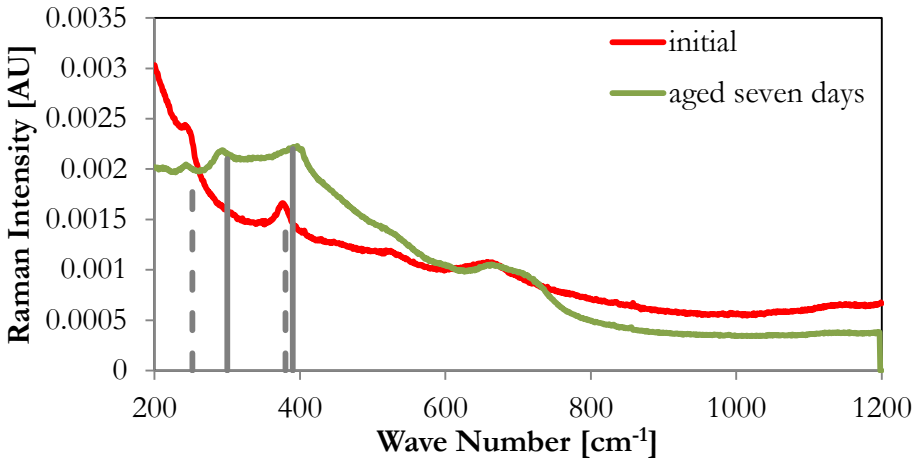

Figure 5-14: *in-situ* Raman showing γ-FeOOH transformation to α-FeOOH, dashed vertical line is reference peak for γ-FeOOH (Gui and Devine, 1995) solid vertical line is reference peak for α-FeOOH (Dunswald and Otto, 1989)

The transformation of γ-FeOOH to α-FeOOH may explain why some EC studies have shown α-FeOOH as an EC product; it may have actually been only the result of aging between generation and characterization.

To summarize the reactions seen in this chapter, a mechanism scheme (Figure 5-15) shows the likely intermediates and conditions for specific species generation. Solid lines show confirmed reactions, such as those with *in-situ* Raman spectra transformation, dashed lines are observed but unconfirmed reactions, such as the transformation of ferrihydrite to γ-FeOOH possibly seen with SEM, and dotted lines are suspected but unconfirmed reactions, such as the $Fe(OH)_2$ intermediate between Fe^{2+} and GR. Double parallel lines indicate that both reactions must occur together to form the product. One reaction that was not included in Figure 5-15 was the direct generation of Fe_3O_4 without a GR intermediate.

While XRD and SEM showed that it may have occurred, cryo-TEM and in-situ Raman showed distinct transformations, suggesting the GR intermediate likely always occurs in the electrochemical generation of Fe_3O_4, but is not always observed by techniques which do not have the temporal resolution to detect it.

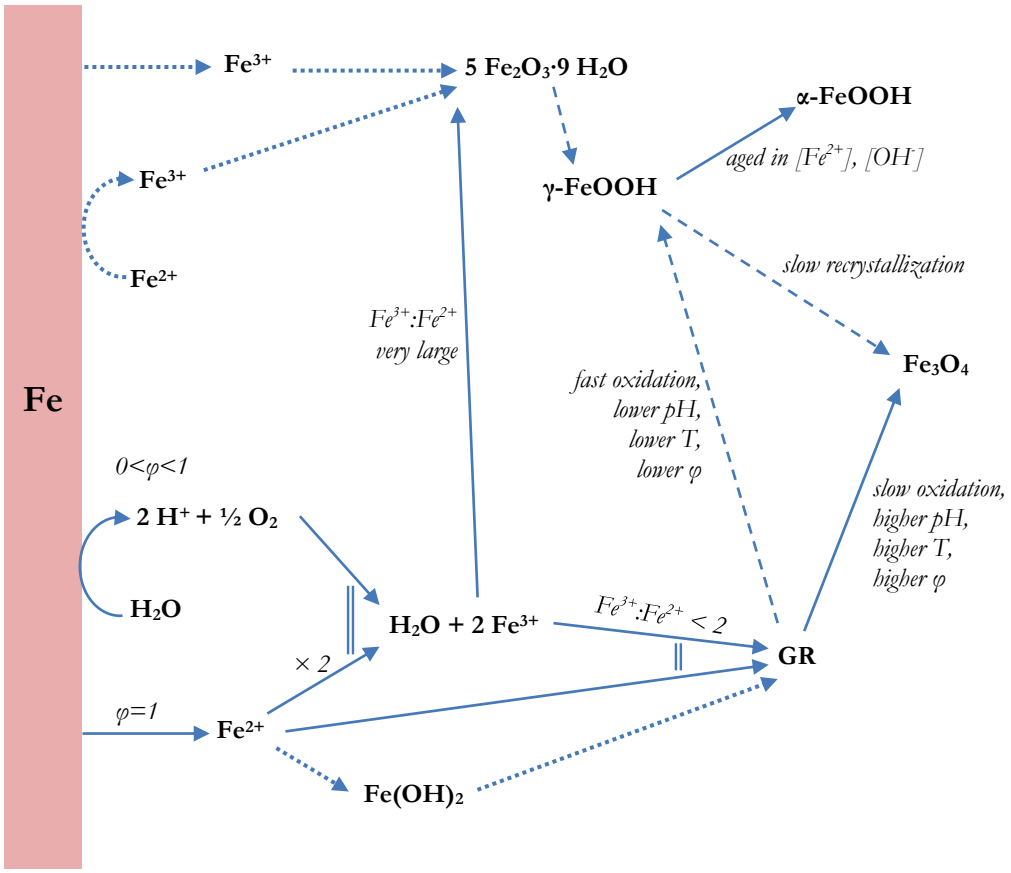

Figure 5-15: Iron EC mechanism scheme. Solid lines are confirmed reactions, dashed lines are observed but unconfirmed reactions, dotted lines are suspected but unconfirmed reactions. Double lines indicate that both reactions are required to form product.

5.4. Chapter Conclusions

In this chapter, novel techniques were used to characterize the products in iron EC and describe a mechanism scheme. Several conclusions can be made:

- Fe^{2+} was generated with low φ at high i without the presence of pitting corrosion promoters. This led to O_2 evolution, Fe^{2+} oxidation, and only γ-FeOOH as an end product, with a possible ferrihydrite intermediate.
- Fe^{2+} was generated with high φ at one of two conditions:
    i. low i without the presence of pitting corrosion promoters, leading to slow Fe^{2+} flux, and a general end product of Fe_3O_4.
    ii. higher i with pitting promoters present (e.g. 1 mM NaCl). This led to higher Fe^{2+} flux, a GR intermediate, and an end product of Fe_3O_4.
- At high i, and low concentrations of pitting promoters, an intermediate φ led to a mixture of γ-FeOOH and Fe_3O_4, depending on pH, $[Fe^{2+}]$, T, and DO.
- γ-FeOOH can age into either α-FeOOH or Fe_3O_4, depending on $[Fe^{2+}]$ and pH. This may allow a pure Fe_3O_4 species after aging, suitable for magnetic separation.
- The GR intermediate is likely always present in EC with sulphate (GR2) or chloride (GR1) present, and transforms into Fe_3O_4 under slow oxidation or γ-FeOOH under fast oxidation conditions.

6. General Potential-Current Model and Validation for Electrocoagulation

6.1. Chapter Introduction

In previous chapters, EC was shown to be effective in NOM removal, with some significant advantages including: ubiquity of reactants (industrial grade iron or aluminum), no chemical addition, no moving parts, and no pH control requirement due to *in-situ* stoichiometric alkalinity generation. However, the major disadvantage of EC is still the requirement of electricity. This can make the process uneconomical for treating drinking either water or wastewater, since both have limitations on κ or TDS, preventing significant additions of salts (usually industrially available NaCl or Na_2SO_4), the simplest method of electrical power reduction. EC has generally been studied as a pollutant-centric technology, without considerable attention to the underlying electrochemistry (Holt et al., 2005). This has likely been due to the electrochemical complexity of EC, involving several inter-related phenomena, including: the cell potential (E_{cell})-current density (i) relationship, the effect of the E_{cell} on EC products, the effect of the electric field ($\nabla\Phi$) on electric double-layer compression in the coagulation process, and the effect of reactor inter-electrode distance (d) and solution flow rate ($\dot{V}$) on local ion concentrations. The "trial-and-error" engineering is apparent in the wide range of electrochemical operating parameters (E_{cell}, i, and $\dot{V}$) reported in continuous EC systems (Table 6-1), where previous studies have shown E_{cell} ranges of 2-300 V and i ranges of 2.5-140 A/m^2.

Table 6-1: Continuous EC systems for drinking water treatment

Study	Pollutant	i [A/m^2]	E_{cell} [V]	Electrode material	Configuration	$\dot{V}$ [L/min]
Vik et al., (1984)	Humic substances	-	6-12	Al	Serpentine parallel plates	0.17
Mills, (2000)	Municipal wastewater	11-62.5	3	Fe	Parallel cylinders	4.5-23
Jiang et al., (2002)	DOC, colour	2.5-10	-	Al	Single parallel plate	0.17
Chen et al., (2002)	No pollutant	0-140	0-20	Al	Single parallel plate	0.05-0.25
Parga et al., (2005)	Arsenic	-	20-40	Fe	Multiple parallel plates	0.60
Mechelhoff, (2009)	Humic substances	0-67	0-300	Al	Two parallel plates	16.6
Emamjomeh and Sivakumar, (2009)	Fluoride	12.5-50	2-9	Al	Single parallel plate	0.15 – 0.40

All studies in Table 6-1 used parallel plate electrochemical reactor (PPER) configurations, as more complex reactor designs have shown no significant improvement (Mollah et al., 2004). Modeling of PPERs has included both ionic distribution modeling (Parrish and Newman, 1969; White et al., 1983) or industrially relevant specific energy and yield information (Kelsall, 1984). The E_{cell}-i relationship has great significance in EC, since it directly impacts EC's greatest disadvantage, electrical consumption, and has been investigated previously: Vik et al. (1984) used a simplified electrochemical potential balance, summing overpotential (η) as a sum of kinetic, mass-transfer, and ohmic resistance terms, but offered no experimental evidence; Chen et al. (2002) formed a complex potential balance that grouped all unknown variables, including Tafel parameters and overpotential terms, into experimentally derived constants, rendering the model inapplicable to other studies;

(Mechelhoff, 2009) constructed a two-dimensional finite element model which simultaneously solved the Navier-Stokes and Nernst-Plank equations for current density distribution, although no experimental validation was attempted; Zongo et al., (2009) experimentally fitted the E_{cell}-i relationship find $E_{cell} = 0.1 + (d/\kappa)i + 0.20 \ln(i)$ for both Al and Fe electrodes in a recirculating continuous system, but again the model is not appropriate for other geometries; Izquierdo et al., (2010) experimentally determined a "corrected" equilibrium voltage (E^0) by assuming a constant ohmic overpotential (η_{ohmic}), which only applied to the author's experimental cell. Most of these prior studies ignored the effects of cathodic H_2 generation and temperature rise due to joule heating, and reduced the η terms and Butler-Volmer relationship to experimental constants. This, unfortunately, has prevented these models from being generalized for scale-up or validation in other systems. A general PPER EC E_{cell}-i relationship, including the impact of cathodic H_2 generation and heat generation, derived from only tabulated dimensions and arbitrary dimensions would thus be extremely valuable. The objectives of this chapter were to derive a general E_{cell}-i relationship, and to test the robustness of the model by comparing numerical solutions to experimental data for several geometric and operating variables. The model could then be applied to any research or industry setting for accurate E_{cell}-i determination.

6.2. Mathematical Model Development

Iron was used as the model anode, since it was the focus of previous chapters, with tabulated E^0 at 298 K (reduction form) for iron oxidation and water reduction as:

Anode: $Fe^{2+} + 2\ e^- \rightleftharpoons Fe$	E_a^0 = - 0.41 V (SHE)	(6-1)
Cathode: $2\ H_2O + 2\ e^- \rightleftharpoons H_2 + 2\ OH^-$	E_c^0 = - 0.83 V (SHE)	(6-2)
Electrolyte: $Fe^{2+} + 2\ OH^- \rightleftharpoons Fe(OH)_2$		(6-3)

The model assumes only reactions (6-1)-(6-3) take place; however, parasitic reactions can occur as well, notably H_2O oxidation:

Anode: $\frac{1}{2}\ O_2 + 2\ H^+ + 2\ e^- \rightleftharpoons H_2O$	E_a^0 = 1.23 V	(6-4)

The ratio of desired or experimental current ($I_{Fe,exp}$) for (6-1) over the theoretical current ($I_{Fe,th}$) were described with a current efficiency (φ) term as:

$$\varphi = I_{Fe,exp}/I_{Fe,th} \quad (6\text{-}5)$$

E^0 for both anode and cathode were adjusted for small changes in temperature (T) by:

$$E_a^T = E_a^0 + \Delta S_a/(z \cdot F) \cdot (T - 298) \quad (6\text{-}6)$$

$$E_c^T = E_c^0 + \Delta S_c/(z \cdot F) \cdot (T - 298) \quad (6\text{-}7)$$

where E_a^T and E_c^T were the electrode equilibrium potentials at temperature T at the anode and cathode, respectively, and ΔS_a and ΔS_c were the changes in entropy and tabulated as $\Delta S_a/(z \cdot F)$ and $\Delta S_c/(z \cdot F)$ for reactions (6-1) and (6-2), respectively, where F was Faraday's constant (96 485 C/mol). E_a^T and E_c^T were adjusted for differing electrolyte concentrations by the Nernst equation:

$$E_a = E_a^T - \frac{2.303 \cdot R \cdot T}{z \cdot F} \log\left(\frac{[1]}{[Fe^{2+}]}\right) \quad (6\text{-}8)$$

$$E_c = E_c^T - \frac{2.303 \cdot R \cdot T}{z \cdot F} \log\left(\frac{p_{H_2}[OH^-]^2}{[1]}\right) \quad (6\text{-}9)$$

where E_a and E_c were the non-equilibrium electrode potentials at the anode and cathode, respectively, R was the universal gas constant (8.314 J/(K·mol)), p_{H_2} was the partial pressure of hydrogen gas at the cathode, and the electrochemical charge transfer number (z) has been shown conclusively as z=2 for iron EC (Lakshmanan et al., 2009; Tanneru et al., 2012; Dubrawski & Mohseni, 2012b). The stable existence of the $Fe(OH)_2$ precipitation product for z=2 in (6-3) is disputed (Lakshmanan et al., 2009); however, $Fe(OH)_2$ served as the stoichiometric product in this model, and non-electrochemical speciation transformations were not included for simplicity.

The PPER EC model (Figure 6-1) had a vertically segmented anode and cathode, both of width (w) and height (h), divided vertically into n equal segments as $y_1, y_2, \ldots, y_j, \ldots, y_n$, with the height of each segment being ($dy=h/n$). The volume contained between the electrodes ($dV=dy \cdot d \cdot w$) moved upward with a controlled flow rate $\dot{V}$ and was assumed to consist of only water, precipitated $Fe(OH)_2$, and electrolytic H_2 gas. The superficial velocity of the liquid, $U_0=\dot{V}/(d \cdot w)$, was assumed to be unaffected by H_2 bubble rise velocity, i.e., $U_n=U_0$. The inlet water had known initial conductivity κ_0, temperature T_0, ferrous ion concentration $[Fe^{2+}]_0$, pH_0, and hydrogen gas partial pressure $p_{H_{2_0}}$.

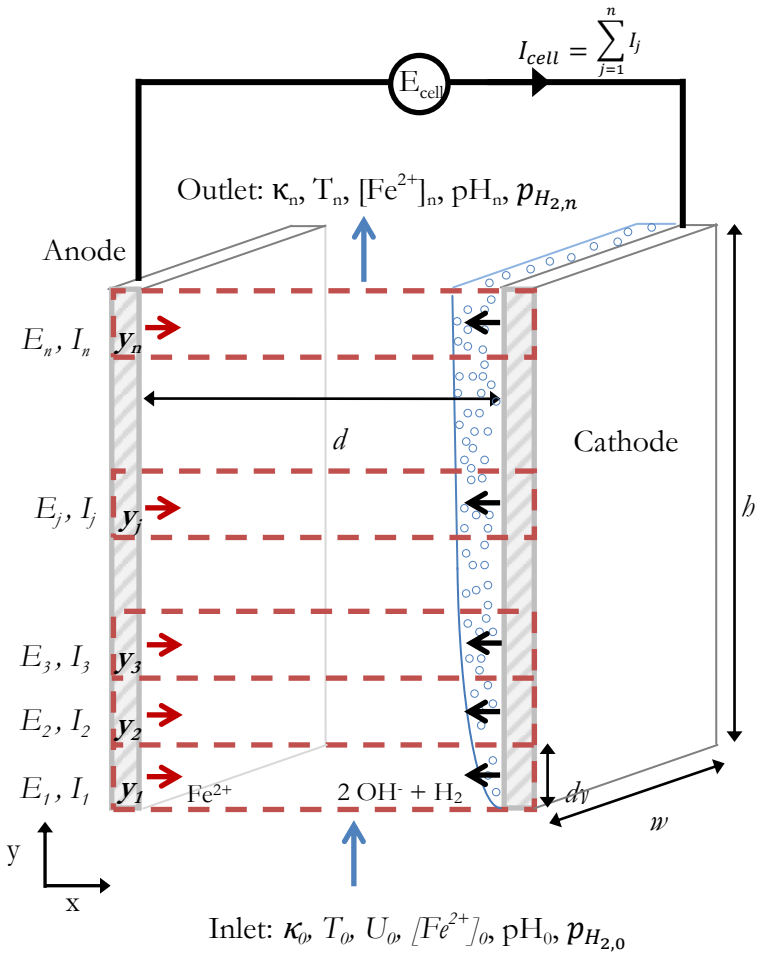

Figure 6-1: Theoretical schematic reactor model

For each *j* segment, a differential electrochemical cell was constructed of electrode area ($dA=dy \cdot w$) with a corresponding potential balance as:

$$E_j = E_{c,j} - E_{a,j} + \eta_{c,j} - \eta_{a,j} - i_j \cdot R_j \qquad (6\text{-}10)$$

Each of the overpotential (η) terms in (6-10) included kinetic (η_k) and mass transfer (η_{Mt}) overpotential as $\eta = \eta_k + \eta_{Mt}$ for both anodic and cathodic reactions, where η_k was given by the Tafel equation for $|\eta| > 0.05$ V as:

$$\eta_{k,c,j} = -\left[b_c \cdot \log\left(-i_{c,j}/i_{0,c}\right)\right] \tag{6-11}$$

$$\eta_{k,a,j} = b_a \cdot \log\left(i_{a,j}/i_{0,a}\right) \tag{6-12}$$

where the Tafel slope was b=2.303·R·T/(α·z·F), i_0 was the exchange current density, and α was the charge transfer coefficient taken to be 0.5. The η_{Mt} term was:

$$\eta_{Mt,c,j} = \frac{2.303 \cdot R \cdot T_j}{z \cdot F} \log\left(1 - \frac{i_{c,j}}{i_{L,c}}\right) \tag{6-13}$$

$$\eta_{Mt,a,j} = \frac{2.303 \cdot R \cdot T_j}{z \cdot F} \log\left(1 - \frac{i_{a,j}}{i_{L,a}}\right) \tag{6-14}$$

where i_L was the limiting current density. Finally, the ohmic resistance term (R_j) in (6-10) took the form:

$$R_j = d/\kappa_j \tag{6-15}$$

where the Bruggeman equation determined the segment conductivity (κ_j) decrease due to H_2 gas generation as:

$$\kappa_j = \kappa_0(\epsilon_{L,j}/\epsilon_{L,0})^{1.5} \tag{6-16}$$

where ϵ_0 was the initial liquid volume fraction, and the liquid volume fraction at segment *j* ($\epsilon_{L,j}$) was calculated with the volume of H_2 produced as an ideal gas in *dV* by Faraday's Law:

$$\epsilon_{L,j} = 1 - \frac{I_j}{z \cdot F}\left(\frac{dy}{U_0}\right)\left(\frac{1}{dV}\right)\left(\frac{R \cdot T_j}{p_{H_2\,j}}\right) \tag{6-17}$$

Equation (6-17) assumes that H_2 bubble rise is instantaneous, this simplification avoided a two-phase flow problem requiring liquid/gas slip velocity (Funk and Thorpe, 1969), discussed later in 6.4.3.

Since κ_j was also affected by joule heating, a linear relationship was assumed for typical solute concentrations in EC as:

$$\kappa_j^T = \kappa_0\left[1 + \alpha_\kappa\left(T_j - 298\right)\right] \tag{6-18}$$

Where the conductivity/temperature coefficient (α_κ) is tabulated and was verified experimentally. To find the temperature at T_j due to joule heating, an energy balance (heat of formations method) on *dV* gave:

$$0 = \dot{H_{in,J}} - \dot{H_{out,J}} + \dot{Q}_J + \dot{W}_J \tag{6-19}$$

Where $\dot{H_{in,J}}$ and $\dot{H_{out,J}}$ were the enthalpy flows at the inlet and outlet of dV at *j*, respectively, relative to elements at standard state and 298K, $\dot{Q}_J$ and $\dot{W}_J$ were the heat and work flows, respectively, entering or exiting *dV* at segment *j*. Assuming an adiabatic reactor ($\dot{Q}_J$=0), and work done to expand electrolytic gases was negligible compared to the electrical work ($\dot{W}_J$) done, the energy balance reduced to:

$$\sum \dot{H_{out,J}} = \sum \dot{H_{in,J}} - (|\eta| + |i_j \cdot R_j|)I_j \tag{6-20}$$

The H_2O, $Fe(OH)_2$ and H_2 reactant and product constituents in each *j* segment were included in the energy balance, giving:

$$\begin{aligned} &\dot{n}_{H_2O,j+1}\left(C_{p,H_2O}\left(T_{j+1}-298\right)+h_{f,H_2O}\right) \\ &\quad+\dot{n}_{Fe(OH)_2,j+1}\left(C_{p,Fe(OH)_2}\left(T_{j+1}-298\right)+h_{f,Fe(OH)_2}\right) \\ &\quad+\dot{n}_{H_2,j+1}\left(C_{p,H_2}\left(T_{j+1}-298\right)+h_{f,H_2}\right) \\ &\quad=\dot{n}_{H_2O,j}\left(C_{p,H_2O}\left(T_j-298\right)+h_{f,H_2O}\right) \\ &\quad+\dot{n}_{Fe(OH)_2,j}\left(C_{p,Fe(OH)_2}\left(T_j-298\right)+h_{f,Fe(OH)_2}\right) \\ &\quad+\dot{n}_{H_2,j}\left(C_{p,H_2}\left(T_j-298\right)+h_{f,H_2}\right)-(|\eta|+|i_j\cdot R_j|)I_j \end{aligned} \tag{6-21}$$

where the enthalpy of formation (h_f) and heat capacity (C_p) for each constituent in the appropriate phase are known and tabulated. The generated products in the (*j*+1) segment included both the molar electrolysis production rates of hydrogen ($\dot{n}_{H_2,gen,j}$) and ferrous hydroxide ($\dot{n}_{Fe(OH)_2,gen,j}$) as:

$$\dot{n}_{Fe(OH)_2,j+1} = \dot{n}_{Fe(OH)_2,j} + \dot{n}_{Fe(OH)_2,gen,j} \tag{6-22}$$

$$\dot{n}_{H_2,j+1} = \dot{n}_{H_2,j} + \dot{n}_{H_2,gen,j} \tag{6-23}$$

The generation terms ($\dot{n}_{H_2,gen,j}$, $\dot{n}_{Fe(OH)_2,gen,j}$) were solved using Faraday's Law and φ=1 at each segment *j*, (6-22) and (6-23) were then substituted into (6-21), which was solved numerically for T_{j+1}. Finally, cathodic and anodic currents were equal and opposite by conservation of charge:

$$i_j = i_{a,j} = -i_{c,j} = I_j/(dy \cdot w) \tag{6-24}$$

and cell potentials were assumed to be equipotential along the vertical, seen elsewhere in EC modeling (Mechelhoff, 2008):

$$E_1 = E_2 = E_j = E_n = E_{cell} \tag{6-25}$$

Substituting (6-11)-(6-18) into (6-10) gave:

$$\begin{aligned} & E_j \\ & = \left[\left[E_c^0 + \frac{\Delta S_c}{z \cdot F}(T_j - 298)\right] - \frac{2.303 \cdot R \cdot T_j}{z \cdot F}\log\left(\frac{p_{H_2\,j}[OH^-]_j{}^2}{[1]}\right)\right] \\ & - \left[\left[E_a^0 + \frac{\Delta S_a}{z \cdot F}(T_j - 298)\right] - \frac{2.303 \cdot R \cdot T_j}{z \cdot F}\log\left(\frac{[1]}{[Fe^{2+}]_j}\right)\right] \\ & + \left[-\left[b_c \cdot \log(i_j/i_{0,c})\right] + \frac{2.303R \cdot T_j}{z \cdot F}\log\left(1 - \frac{-i_j}{i_{L,c}}\right)\right] \\ & - \left[b_a \cdot \log(i_j/i_{0,a}) + \frac{2.303R \cdot T_j}{z \cdot F}\log\left(1 - \frac{i_j}{i_{L,a}}\right)\right] - i_j \\ & \cdot \frac{d}{\kappa_0\left[\left[1 - \frac{i_j(dy \cdot w)}{z \cdot F}\left(\frac{dy}{U_0}\right)\left(\frac{1}{dV}\right)\left(\frac{R \cdot T_j}{p_{H_2\,j}}\right)\right]/\epsilon_0\right]^{1.5} \cdot \left[1 + \alpha_\kappa(T_j - T_0)\right]} \end{aligned} \tag{6-26}$$

Assuming that, upon entry to the PPER, $T_1 \approx T_0$, $p_{H_2\,1} \approx p_{H_2\,0}$, $[OH^-]_1 \approx [OH^-]_0$, and $[Fe^{2+}]_1 \approx [Fe^{2+}]_0$, the full E_j-i_j relationship was defined for any EC geometry, initial temperature, pH, and conductivity. Solving equations (6-21) and (6-26) simultaneously allowed the numerical solving of the system of equations for i_{j+1}, …, i_n etc. The E_{cell}-I_{cell}

relationship, which could be verified experimentally, was determined with equations (6-22), (6-24), and the summation of *n* partial currents as:

$$I_{cell} = \sum_{j=1}^{n} I_j \tag{6-27}$$

The complete numerical model required the following assumptions:

- No passivation occurred on electrode surfaces
- There was negligible internal circuit resistance
- The system was insulated and adiabatic
- Only reaction (6-1) took place at the anode and reaction (6-2) at the cathode, at the cathode at perfect stoichiometry, reaction (6-3) took place instantaneously in solution
- Tafel parameters and limiting current densities were not affected by temperature changes
- No phase changes took place within the system
- Instantaneous H_2 bubble rise compared to electrolyte velocity, and the superficial velocity of the electrolyte was under laminar flow conditions and not affected by H_2 bubble rise

Appendix A shows the complete MATLAB code used in this chapter.

6.3. Experimental Materials and Methods

6.3.1. EC reactor

A custom PPER was manufactured from acrylic (McMaster-Carr) with high tolerance (1/1000 inch) to accommodate a perfectly parallel electrode system (Figure 6-2). Anodes were 99.9% iron foil of 1 mm thickness (Goodfellow), precision cut into twelve separated vertical segments (w=38 mm, dy=20 mm), connected in parallel via insulated low-resistance copper. The cathode (w=38 mm x h=240 mm) was stainless steel grade 304 (McMaster-Carr). A DC power supply (Instek PSP-603 with Fluke 189 data-logger) supplied potential to each anode/cathode couple in potentiostatic mode in a range of E_{cell}=2-20 V.

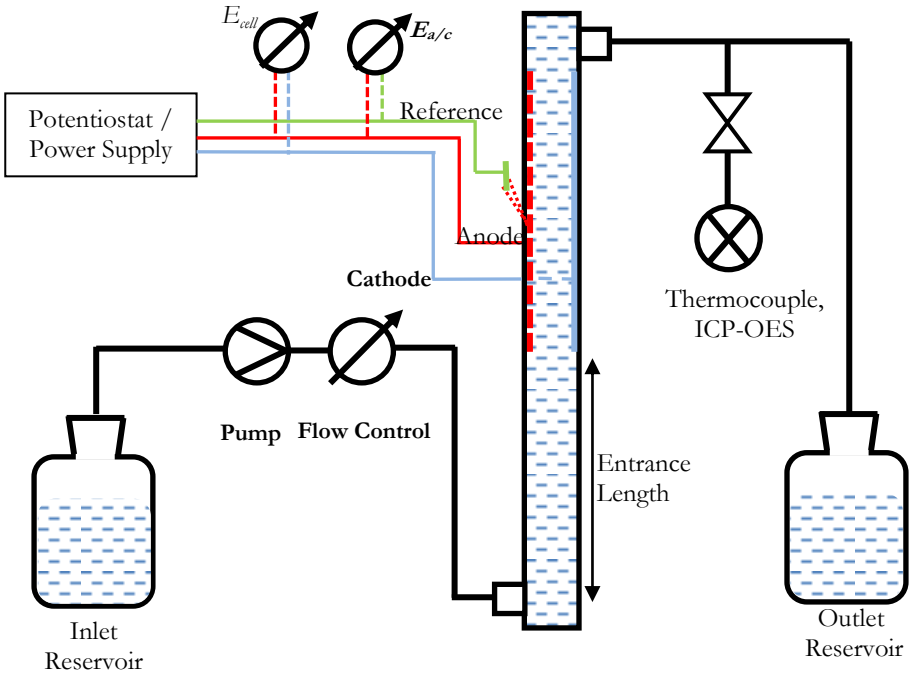

Figure 6-2: Experimental reactor

Synthetic water was composed of pH-neutral Milli-Q deionized water at T_0=20 ºC, and either Na_2SO_4 or NaCl (Laboratory Grade, Fisher Scientific) in concentrations of 50, 150 or 500 mg/L. It was pumped via a peristaltic pump at a flow rate range of $\dot{V}$=0.1-0.3 L/min. An entrance length of 285 mm was added to the acrylic reactor's height to ensure fully developed laminar flow, calculated for $\dot{V}$=0.3 L/min (Pickett and Ong, 1974), and confirmed by numerical flow simulation with Simulink® software for identical geometry (Figure 6-3).

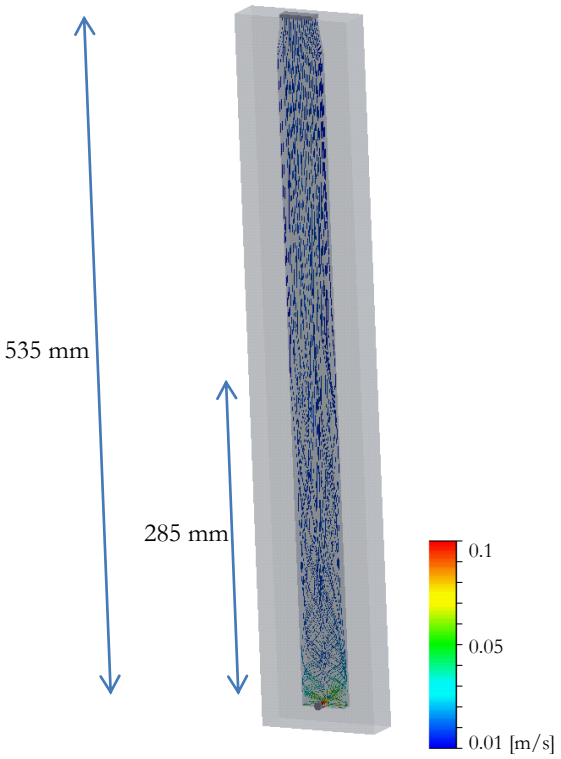

Figure 6-3: Simulink® flow simulation for experimental PPER geometry

A sampling port at the reactor exit allowed non-intrusive sampling for T_n, κ_n, and $[Fe]_n$. Several geometrical parameters were varied to determine the model's robustness to experimental variation: total electrode area (n=6, 12), inter-electrode gap (d=2, 10 mm), and electrode surface conditions (polished or rusted).

6.3.2. Tafel Parameters

Tafel parameters were found *in-situ* for $\dot{V}$=0.1-0.3 L/min with a three-electrode cell system connected to a potentiostat (Princeton Applied Research, Versastat 3). A small borehole was drilled into the acrylic reactor and electrode surfaces, fitted with a Luggin capillary and Ag/AgCl reference electrode (BASi RE-5B). The Luggin tip was placed just at the electrode surface without impeding flow. A Pt counter electrode of 15 mm long and 1 mm diameter (Radiometer Analytical, XM110) was inserted into the opposite borehole as close to the Luggin tip as possible. The scan rate was 0.5 mV/s. Values of $i_{L,a/c}$ were examined *ex-situ* with a rotating disc electrode (RDE) of 5 mm diameter composed of 99.99% Fe (Pine Instruments) attached to a vertical shaft RDE system (Pine Instruments AFMSRCE) in the same synthetic waters at rotation speeds of ω=10-1000 RPM.

Before each experiment, electrodes were wet-polished with P200 SiC, P1500 SiC, and emery paper, rinsed with 1% sulphuric acid, and double rinsed with Milli-Q water. Electrolysis took place directly after polishing to avoid surface film formation. For the investigation of

the impact of surface condition, the electrodes were left exposed to moisture and air for seven days before experiments, without subsequent polishing.

6.3.3. Analytical Methods

Reactor outlet temperature was monitored with a K-type thermocouple attached to a logging voltmeter (Fluke 80AK-A/Fluke 189). Conductivity was monitored (YSI-3200) at the outlet and to determine experimental conductivity temperature coefficient (α_κ) values. Outlet iron concentrations were measured by inductively coupled plasma optical emission spectroscopy (ICP-OES) with a wavelength of 238.204 nm (PerkinElmer Optima 7300 DV). 20 mL aliquot samples were first acidified with 100 μL of a 3:1 HCl to HNO_3 (Laboratory grade, Fisher Scientific) solution of *aqua regia*. All experiments were performed in duplicate. Standard error is shown as vertical error bars in all figures.

6.4. Results and Discussion

6.4.1. Tafel Parameters and Model Inputs

Figure 6-4 shows an example Tafel polarization plot for 500 mg/L NaCl with $\dot{V}$=0.1 L/min, d=2 mm, giving b_a = 93 mV/dec, and $i_{0,a}$ = 0.00025 A/m^2. Repeatability of b_a was moderate under identical conditions (RSE=10%), while $i_{0,a}$ was less repeatable but within a range of 0.0001-0.0005 A/m^2. On the cathode, b_c = 164 mV/dec, and $i_{0,c}$ = 0.0011 A/cm^2 were

found with similar deviations. Tafel parameters were within the range typically reported for reactions (6-1) and (6-2) (West, 1986).

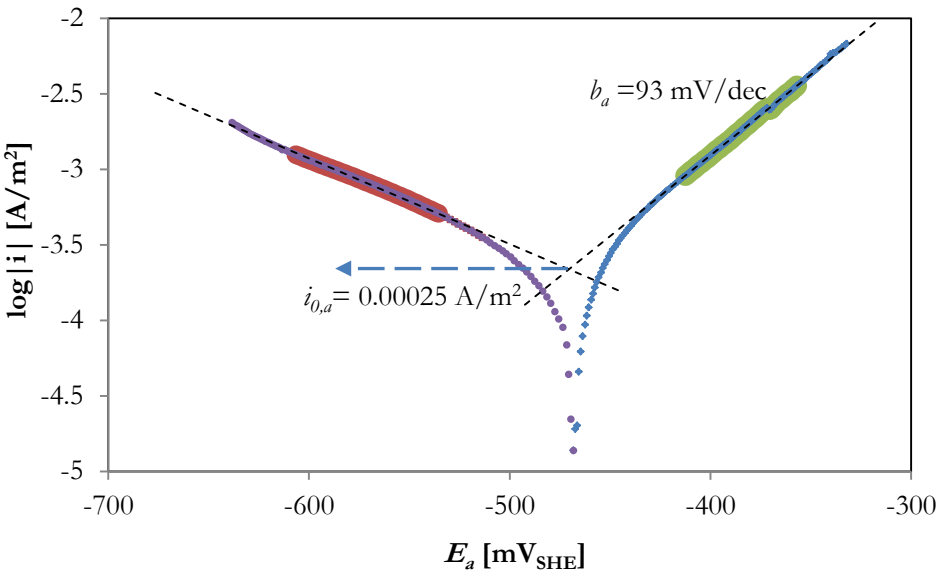

Figure 6-4: Tafel plot for Fe ↔ Fe^{2+} + 2 e^-, 500 mg/L NaCl, 0.1 L/min

Less conductive solutions had a high internal ohmic drop between the counter electrode and the Luggin tip, giving unreliable results. Likewise, Tafel parameters were less repeatable at higher vertical positions due to H_2 gas disturbances. For these reasons, values of b_a = 93 mV/dec, $i_{0,a}$ = 0.00025 A/m^2, b_c = 164 mV/dec, and $i_{0,c}$ = 0.0011 A/m^2 were used for all *j* segment numerical solutions, and recommended for future iron EC work. RDE experiments could not detect any limiting current plateau for either of reactions (6-1) or

(6-2), likely as there was no limit of reactants to the electrode surface (Fe(*s*) and H_2O were in excess) and there was no mass transfer limitation in product removal from the electrode surface due to appreciable $\dot{V}$. For these reasons, $i_{L,a/c} = \infty$ was used. Other relevant model inputs were: T_0=293.15 K, $p_{H_2\,j}$=1 atm (Vogt, 1987); $[OH^-]_j$= 0.001 M and $[Fe^{2+}]_j$= 0.0005 M, based on a relatively constant localized pH at the cathode electrode surface of pH=11 and stoichiometric $[Fe^{2+}]$ (Mechelhoff, 2009); $\Delta S_a/(z \cdot F)$=0.07 mV/K, $\Delta S_c/(z \cdot F)$=-0.836 mV/K (Bratsch, 1989); and α_κ values were determined experimentally and found in a range of α_κ= 0.026-0.033 1/K (RSE=2.7%) for all solute concentrations in a range of *T*=293.15-323.15 K.

6.4.2. Segmentation

Figure 6-5 shows the numerical model results for T_j, and κ_j, along the vertical height for 150 mg/L Na_2SO_4 and 500 mg/L NaCl with *d*=2 mm, $\dot{V}$=0.1 L/min, and E_{cell}=3V, 10V, and 15/20V. For 150 mg/L Na_2SO_4, modeling predicted a temperature rise from 273 K at the reactor entrance to a maximum of 301 K at the reactor exit for 20V (Figure 6-5A). Experimental temperature rise for the same conditions gave an average exit temperature of 299 ± 1 K. The numerical model predicted a rise in κ_n from 0.031 S/m to 0.038 S/m for 20 V (Figure 6-5B), while experimental exit κ_n values were 0.035 S/m ± 0.002 S/m. For 500 mg/L NaCl, the theoretical exit temperature was *T*=294 K for E_{cell}=3V (Figure 6-5C), which was observed exactly in experiment at 294 ± 1 K. For 15V (20V was not attainable experimentally), the theoretical exit temperature was *T*=312 K, while the experimental

temperature was 310 K ± 2 K. Conductivity was numerically predicted to rise from 0.132 S/m to 0.191 S/m for 15 V (Figure 6-5D), but, κ_n only rose to 0.169 S/m ± 0.004 S/m in experimentation.

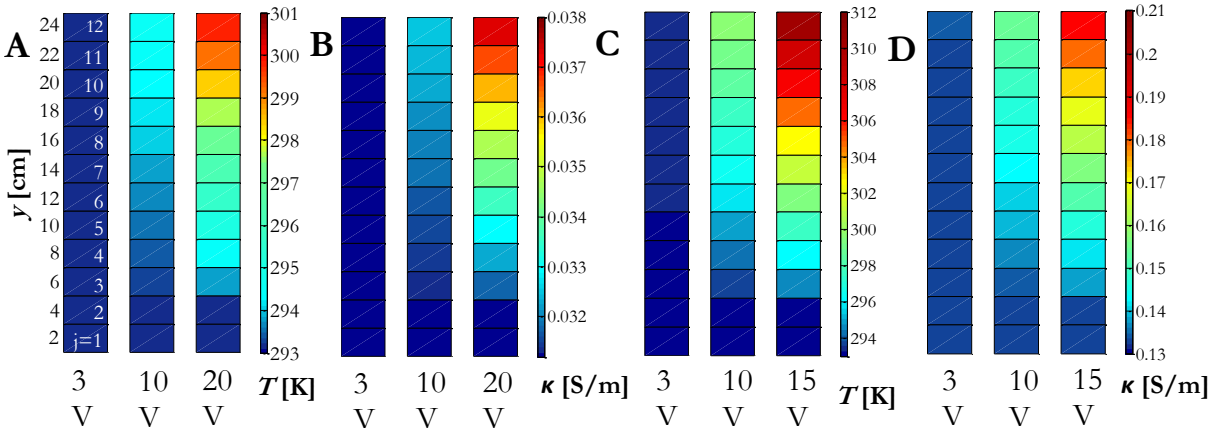

Figure 6-5: Segmentation results for A) T_j, 150 mg/L Na_2SO_4, B) , κ_j, 150 mg/L Na_2SO_4, C) T_j, 500 mg/L NaCl, and D) κ_j, 500 mg/L NaCl

Numerical ΔT solutions were generally quite accurate for either solute with mean relative deviation (ζ) of $\zeta < 9\%$, where $\zeta = 1/n \cdot \sum|\Delta T_{exp} - \Delta T_{th}| / \Delta T_{th}$ (ζ differs from *RSE* in that ζ measures deviation of the differences). Experimental T values were generally lower than model predictions due to the non-adiabatic reality of the reactor; heat was likely lost through the reactor walls or metal electrodes. Numerical solutions for conductivity were not as accurately predicted. This may have occurred since conductivity was measured *ex-situ*, allowing temperature, ionic activity reductions, and gas fractions to equilibrate before analysis.

Figure 6-6 compares the experimentally determined current density distribution with those given by the numerical model in the *y*-direction for E_{cell}=10 V and d=2 mm. For 150 mg/L Na_2SO_4 (Figure 6-6A), model predictions were generally accurate, with maximum deviation from experimental data being 2.5 mA (ζ=2.4%).

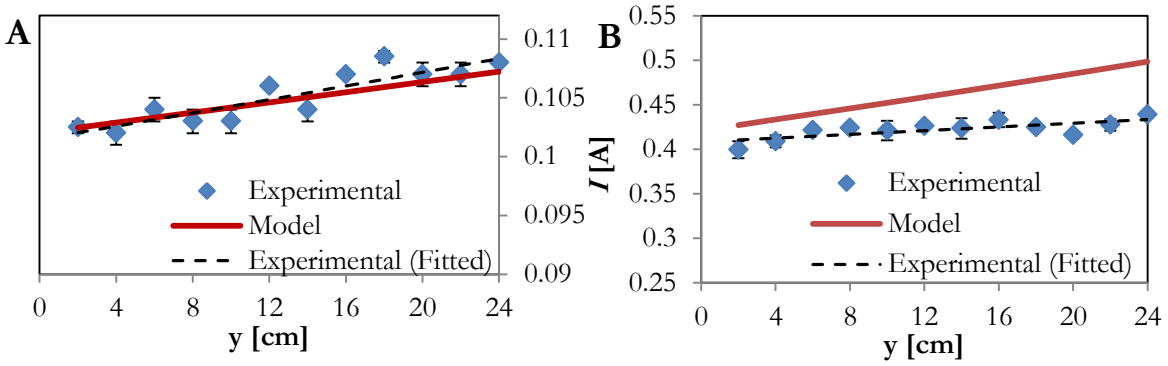

Figure 6-6: Segmentation results for I_j, E_{cell}=10V, d=2 mm for A) 150 mg/L Na_2SO_4 and B) 500 mg/L NaCl

Figure 6-6B shows less accurate numerical solutions for 500 mg/L NaCl, with a maximum deviation of 68.7 mA (ζ =14.2%). This is in part due to greater $\Delta\kappa$ predicted than experimentally observed, as noted above. However, a more likely explanation for why lower concentration solutions were better predicted than higher ones, was that the higher I_j values at higher κ produced more H_2 gas, inducing greater inter-segment axial mixing, inducing a more homogenous κ and i distribution. This is seen in the flatter experimental data in Figure 6-6B, compared to a steeper numerical result.

6.4.3. Impact of Solute Type, Concentration, and Geometric Variables

In Figure 6-7, comparisons between the experimental and numerical E_{cell}-I_{cell} relationship can be seen for differing solutes and concentrations. The model was accurate in predicting I_{cell} in the complete E_{cell} range of 2-20V for 50 and 150 mg/L, the average deviation between the model and numerical results was ζ =9% for 150 mg/L NaCl. The model's accuracy decreased above I_{cell}= 4 A, corresponding to an i_{cell} of 44 mA/cm^2. For 15 V, the model over predicted I_{cell}, with ζ=14% and 12% for 500 mg/L NaCl and Na_2SO_4, respectively. The likely reason was that the ΔT predicted by the model was higher than that experimentally observed at higher E_{cell}, as seen earlier. Also possible was the breakdown of the assumption of independent gas/liquid velocity at the higher H_2 flux above i_{cell} = 44 mA/cm^2. In this case, I_{cell} was more affected by $\Delta\epsilon_{L,j}$ than by ΔT, due to the power relationship of κ to $\epsilon_{L,j}$ in equation (6-16), compared to the linear relationship of κ to ΔT. Thus the current model is generally limited to i_{cell} < 50 mA/cm^2 for d=2 mm. For i greater than this, or for smaller electrode gaps, the model would require a more a complex solution for the gas voidage fraction ($\epsilon_{g,j}$), which takes the general form of $\epsilon_{g,j} = 1/(1 + \dot{V}_j\sigma_j/\dot{H}_{2,j})$, (Funk and Thorpe, 1969). This would essentially require that the volumetric gas flow rate ($\dot{H}_{2,j}$) and slip ratio (σ) be solved for each j segment, using the coalescence barrier model (Kreysa and Kuhn, 1985) or similar (Vogt, 1987) and the segment gas velocity ($u_{H_2,j}$) as $u_{H_2,j} = R \cdot T/(p_{H_2,j} \cdot F \cdot z \cdot d) \cdot \int_0^y i_j \cdot dy$ (Bisang, 1991). However, it is unlikely that EC would (or should) be operating above these limits, since ohmic resistance demands would consume a significant

proportion of E_{cell} due to a high gas fraction. Thus, the current model is acceptable for most cases of EC simulations, without requiring two-phase flow solutions. Furthermore, i_{cell} = 50 mA/cm^2 would give a coagulant dose of 87 mg Fe/L for $\dot{V}$=1 L/min (assuming a φ=1 Faradaic reaction), more than sufficient for successful water treatment at an appreciable flow rate, as seen in Chapter 3 and Appendix B.

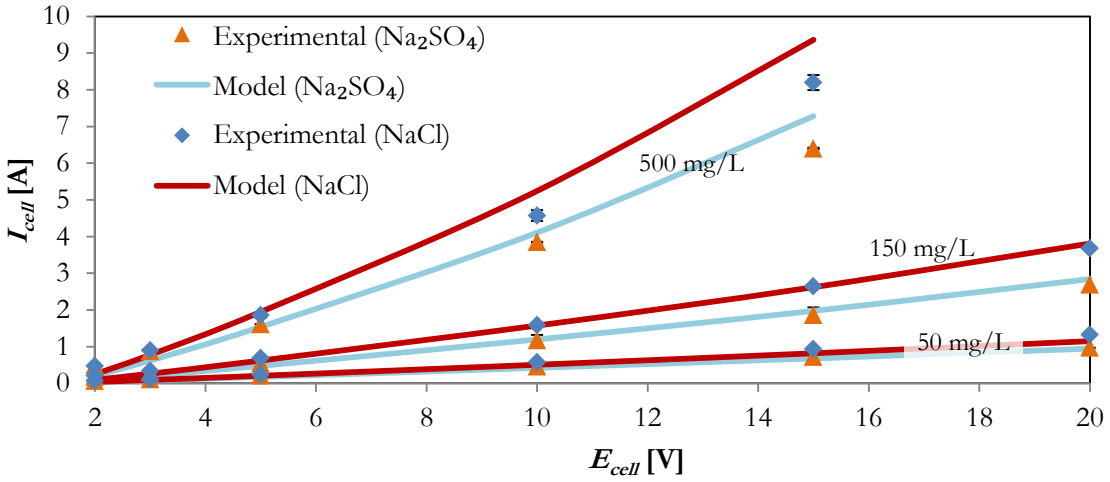

Figure 6-7: Comparison of experimental and modeling results: impact of solute

Figure 6-8 compares experimental and numerical solutions for differing d, $\dot{V}$, and n for 500 mg/L NaCl. The higher $\dot{V}$=0.3 L/min results in a numerical solution of slightly less I_{cell} for higher E_{cell}, since ΔT was less significant due to the higher flow, also seen in experimental results. The effect of the greater d=10 mm was two-fold, an increase in the effect of cell resistance by equation (6-15), and a decrease of the effect of $\epsilon_{L,j}$ by equation (6-17), since

dV was five times greater. The effect of lower electrode area, n=6, had the same numerical result of i_{cell} as for n=12, but half the I_j by equation (6-22). This led to less H_2 production, decreasing the effect of $\epsilon_{L,j}$. Generally speaking, numerical results had good agreement with experimental data, with $\zeta < 8\%$ for E_{cell} = 10V, a safe nominal operating voltage commonly used in EC processes, and an average of ζ=17%, across all variables and including all values of E_{cell}. These results suggest a high robustness of the model and general applicability to variable geometries.

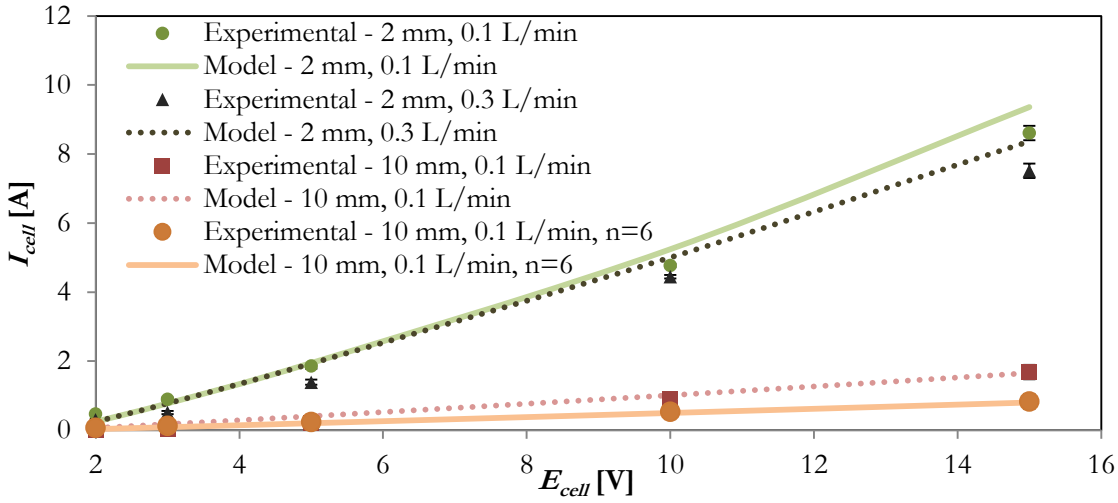

Figure 6-8: Comparison of experimental and modeling results: impact of d, $\dot{V}$, and electrode surface area (n)

The differing κ_0, d, and $\dot{V}$, all affected the ohmic resistance of the cell, causing ohmic contribution to be greater or less than the contribution of the (E_c - E_a) or (η_c - η_a) terms in equation (6-10). These relative ratios are useful for EC design since, generally speaking, only

the ohmic losses can be re-engineered for electrical consumption optimization. Only η_c could be reduced otherwise, with a platinum coating on the cathode material, increasing the $i_{0,c}$ a few orders of magnitude (West, 1986), but likely too expensive and prone to attrition in practical mixed water inlet streams. The lowest contribution from ohmic drop occurred at lower E_{cell} for the higher κ_0 solutions (500 mg/L), but still consumed approximately 50% of E_{cell} as wasted heat. Lower κ_0 (50 mg/L) had even greater ohmic losses, consuming over 90% for E_{cell}=20 V. Clearly, this is too great of electrical waste, which suggests two feasible options for EC: *i*) increase κ_0 to the maximum allowable concentration or ii) increase electrode surface area towards practical limitations. The fallibility of option *i*) is that it cannot prevent the drop in κ associated with gas fractions, a contribution which can decrease κ by greater than 50% (Bisang, 1991), whereas option ii) can do both. Both option *i*) and ii) are currently performed in industry applications of EC, but the model described in this study allows numerical solving of the fraction of consumption of E_{cell} for each element of the potential balance.

6.4.4. Impact of Electrode Surface Condition

Figure 6-9A shows the impact of a polished versus unpolished (rusted) electrode surface finish. It is immediately apparent that there was a significant difference in experimental data; the polished electrode had a low numerical model deviation of ζ=9% from the experimental results, while the rusted electrode showed an average deviation of ζ=44%. Interestingly, the greater I_{cell} was seen in the rusted electrode, which was somewhat

unexpected, since the passivation layer normally acts as an additional ohmic term, *decreasing* current.

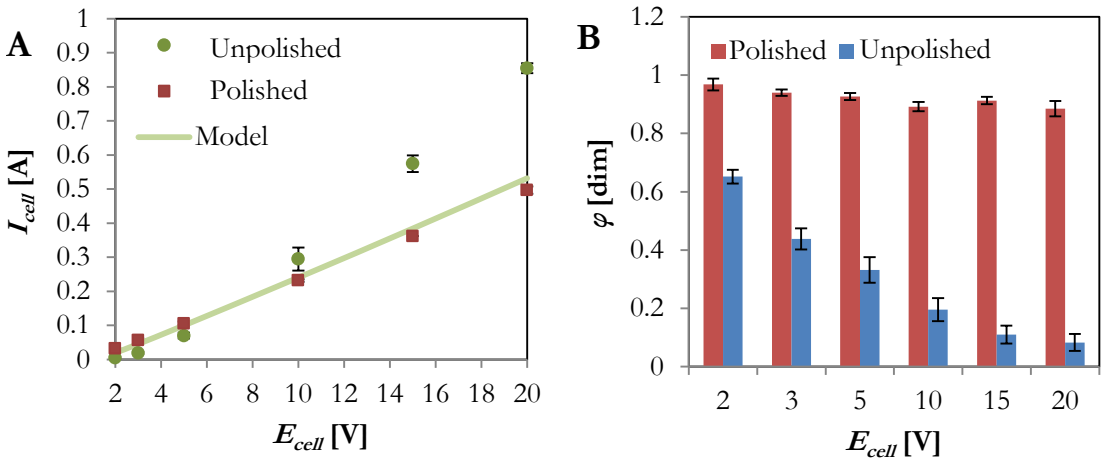

Figure 6-9: Comparison of experimental and modeling results for A) electrode surface conditions and B) φ results, 150 mg/L Na_2SO_4, d=10 mm

The atmospheric corroded oxide layer was likely composed of α-Fe_2O_3, δ-FeOOH, and γ-FeOOH (Keiser and Brown, 1983), and prevented further iron oxidation, instead driving the oxidation of H_2O. To confirm this, samples at the reactor exit were analyzed for total Fe to determine φ. Figure 6-9B shows the results for both the polished and rusted surfaces, and the decline in φ at higher E_{cell} for the rusted surface indicated that other reactions were taking place on the rusted anode surface, likely reaction (6-4). At all E_{cell}, φ was an average of 91.1% for the polished electrode, while it dropped down to a minimum of 8.3% for the rusted electrode at E_{cell}= 20 V. The high φ for the polished case suggests that the single

reaction assumption and χ=2 in the numerical model was valid. Greater I_{cell} was observed on the rusted anode than the polished anode at higher E_{cell}, likely due to anodic O_2 being reduced on the cathode surface, since there was no separating membrane. This occurred since the reverse of equation (6-4) is a spontaneous reaction, supplying more driving force to the system, but overall a waste of system energy. In NaCl solutions, pitting corrosion, as described in Chapter 5, led to normal dissolution regardless of the rust layer. In fact, the rust layers eventually wore away, producing a shiny Fe surface. This suggests that temporary NaCl addition, even in drinking water, can "clean" rusted iron electrode surfaces.

6.5. Model Application and Economic Assessment of EC

A simple cost model of EC was applied combining the potential balance model described in this chapter, and a bench-scale reactor described in Appendix B. The bench-scale reactor operated at a flow rate of 3 L/min, had a CL of 100 C/L and I_{cell} of 5 A, which was sufficient to remove approximately 70% of initial NOM (see Appendix B for NOM removal details). With known geometric variables, equations (6-21), (6-26), and (6-27) were solved numerically to give E_{cell}=2.18 V, which had an approximately 10 % deviation from the measured value of E_{cell}=2.41 V. With E_{cell} and I_{cell}, total power consumption was calculated as P_{cell}= 0.60 kWh/1000 L, corresponding to an electricity cost of \$0.060/1000 L, assuming a nominal electricity cost of \$0.10/kWh (higher cost in rural locations). Coagulant cost estimation assumed iron purchased as sheet metal at \$2/kg, giving costs of \$0.057/1000 L for coagulant. Assuming electrodes require replacement after 80% of total mass is used,

total costs were \$0.146/1000 L for consumables (electricity and metal), without pH adjustment or salt dosing. If conductivity enhancing salts were used to enhance κ to 5000 μS/cm, the model would calculate E_{cell} = 1.68 V, and total costs would be \$0.136/1000 L, saving only \$0.01/1000 L with the conductivity enhancement. At a larger scale (say 4 ML/day), the capital costs of EC are significant, and should be factored into the cost. Assuming electrodes can scale linearly (requiring 125 anodes of 1 m^2, in parallel plate or other electrode configuration), electricity and metal consumption should remain the same. An electrode bank of this size would have a footprint of approximately 7.5 m x 1 m x 1 m, and the electrodes would last approximately six months before requiring replacement. A 5000 A DC power supply, transformer, and electrical connection cost estimation is ~ \$200,000 (Magna Power Inc.). Assuming the most significant difference in capital cost between EC and CC is the DC electrical system, and the power supply cost can be distributed over a 20 year working life, EC operating costs show a total of \$0.152/1000 L. These cost values are conservative, and industrial discounting of raw Fe metal (or possibly recycled Fe scrap material) and electrical costs could potentially decrease the cost to as little as \$0.076/1000 L. These EC costs favour comparably to the cost of chemical coagulation, estimated to be \$0.113 – 0.226/1000L in rural Canada (Braul and Leader, 2001). This costing methodology and model application provide a simplified, but important decision making estimate for future EC evaluations and pilot studies.

6.6. Chapter Conclusions

In this chapter, a numerical model relating potential and current in a continuous PPER iron EC system was developed for application in water treatment systems. Several conclusions can be made:

- The model was robust and generally valid for a range of common solutes, PPER geometries, E_{cell}, κ_0, d, and $\dot{V}$.
- For $i_{cell} > 50$ mA/cm^2, the model would likely require a two-phase solution to account for a higher H_2 (g) electrode surface coverage.
- A simplified version of the model was also used in a pilot parallel plate EC reactor for NOM removal from a local source, with ζ=10%. Results are shown in Appendix B.
- Iron electrodes require polishing for high φ and model accuracy. A rusted Fe electrode has low φ in Na_2SO_4, especially at higher E_{cell}.

7. Thesis Conclusions

7.1. Summary of Results

This thesis aimed to investigate the electrochemical generation of solid-state coagulant, or electrocoagulation (EC), for the removal of natural organic matter (NOM) from highly impacted drinking water sources. This thesis found EC to be a viable process for NOM impacted drinking water treatment, meeting 50% USEPA removal guidelines for a variety of NOM source waters and solute impacts, providing agreeable water without the addition of salts or pH control. Iron electrodes showed the best NOM removal compared to aluminum and zinc electrodes, and had no passivation or ecotoxicity issues, and was thus investigated further.

Different EC operating parameters were seen to have markedly different NOM removal capabilities. Lower i showed increased φ in synthetic water, and it was shown that optimum NOM removal was at i ~10 mA/cm^2, below which it led to unnecessary increases in electrode surface area without significant gains in NOM removal. A lower *CLR* had greater NOM removal, but led to a slower process requiring up to 15 min of flocculation. Higher *CLR* combined with microfiltration led to an almost instantaneous NOM removal process, although required a higher metal dose than lower *CLR* for similar reductions.

These results led to the defining of four general EC "classes" of operation that affect the key costs and sustainability performance measures of EC: coagulant dose, electrical

consumption, process speed, and volumetric footprint. These classes are general, and can be applied to EC of other anode materials, other pollutants, and other scales of operation.

The effect of EC operating parameters on iron speciation and NOM removal was then investigated in local natural water. Low *i* and *CLR* led to lower pH and DO where *in-situ* Raman spectroscopy found predominantly GR species formation. Greater *i* and/or *CLR* led to higher DO, and only γ-FeOOH generation. GR removed NOM slightly better than other generated species.

In synthetic water, *in-situ* Raman spectroscopy, aqueous XRD, SEM, and cryo-TEM led to characterization of products and transformations of several EC species. High φ was found at either low *i* without the presence of pitting promoters (chloride), or high *i* with chloride presence. This led to a higher Fe^{2+} flux, a GR intermediate, and an end product of Fe_3O_4.

Finally, a numerical model relating potential and current was developed for parallel plate EC reactors. The model used no experimental data fitting, and was built from a simple potential balance. It accounted for conductivity changes by temperature and gas fraction changes, and was experimentally validated for several geometric parameters. This model will allow research and industry the ability to predict and optimize electrical consumption in EC *a priori*.

Overall, this thesis achieved what it aimed to do, develop a practical technology for use in low-income and rural communities, and advance the science of EC. I am indebted to those

who inspired me to complete a Ph.D. in disruptive "green" technologies, especially in the water sector, which has become my passion and livelihood.

7.2. Future Work

The future of EC still requires elucidation of several key components. A list of future activities for those who are interested in furthering the scientific advancement of EC might look into the following:

- For NOM removal, a study of the effect of the electric field in EC on enhancing coagulation would be useful in determining if higher cell potentials can induce coagulation. Experiments might include differing concentrations of electrochemically generated coagulant in solution with inert (e.g., stainless steel) electrodes at differing field strengths, determining this effect on NOM removal. If electric fields can indeed contribute to coagulation, a possibility for a high field, non-sacrificial parallel plate electrode system could be tested for NOM removal. This would complement advanced micro-fluidics research, since small gaps would be required to reduce ohmic loss and prevent water electrolysis.
- Since conductivity of drinking water cannot be significantly enhanced, and increasing surface area or reducing inter-electrode gap has practical limitations, the reduction of electrical energy may require novel electrode designs. These might include the investigation of 3-D electrode systems, including porous electrodes or fluidized bed electrodes, greatly increasing surface area and reducing ohmic losses. An interesting and unexplored phenomenon is in bipolar fluidized bed electrodes, where plate

electrodes can be replaced by sacrificial fluidized particles, allowing no electrode waste and higher surface area.

- More work is required elucidating the fraction of NOM removal by higher purity GR. Synthetic GR (chemical generation) should be looked at for definitive analysis of its effect on NOM removal, and fraction of removal. Also, determining EC conditions (electrode potential, dissolved oxygen, solute constituents) in a PPER that allow a more stable GR in pilot work would be helpful in assessment of the potential of an industrial GR EC process.
- Further research into exploting this thesis's findings of conditions leading to Fe_3O_4 generation will allow future EC work to focus on ferrimagnetic particles, allowing for the magnetic separation of pollutants sorbed to nano-particles. Fe_3O_4 generation size was as low as 15 nm, and <12 nm particles will likely exhibit superparamagnetism and the ability to be removed by low gradient magnetic fields. This work is currently being pursued by a joint UBC-UC,Berkeley DOE grant application on "magneto-EC". If approved, Chapter 4 and 5 will aid future researchers on NOM removal and generation conditions.
- An exciting possibility is the EC co-generation of ferrate, an advanced oxidant that occurs during electrochemical magnetite oxidation at high pH. This should be explored as a novel oxidation/coagulation process for both drinking and waste water. The likely best approach would be operating EC at very high current densities (creating very high localized pH) in a contained reactor, and releasing a concentrated slipstream for application. The build-up of magnetite on anode

surfaces, seen as wasteful in industrial EC systesm, may actually be beneficial to ferrate generation.

- The research into the fundamentals of disinfection (both bacteria and viruses) by iron EC should be investigated thoroughly. While some literature shows positive results for disinfection, there appears to be no fundamental explanation whether it is floc enmeshment, free radical damage, electrical effects, or other effects that cause up to 4-log disinfection. If this is solved, a potential replacement for chlorine disinfection is possible, a lucrative and "green" innovation challenge. The best approach would likely be to attempt to investigate the contributing factors independently (e.g., separate experiments investigating electrical effects with inert electrodes and free-radical damage from Fe^{2+} generation). Possible electrochemical mechanisms include the electrochemical generation of ferrate, hypochlorite, or hydrogen peroxide.

Bibliography

Aber, S., Amani-Ghadim, A.R., Mirzajani, V., 2009. Removal of Cr(VI) from polluted solutions by electrocoagulation: Modeling of experimental results using artificial neural network. Journal of Hazardous Materials 171 (1-3), 484–490.

Addy, S.E.A., 2008. Electrochemical arsenic remediation for rural Bangladesh. Ph.D. thesis, University of California, Berkeley.

Adin, A., Soffer, Y., Ben Aim, R., 1998. Effluent pretreatment by iron coagulation applying various dose-pH combinations for optimum particle separation. Water Science and Technology 38, 27–34.

Allen, H.E., Hall, R.H., Brisbin, T.D., 1980. Metal speciation. Effects on aquatic toxicity. Environmental Science and Technology 14 (4), 441–443.

Amy, G.L., 1993. Using NOM characterization for the evaluation of treatment, in. AWWA Proc. Workshop on NOM in Drinking Water.

Anand, P., Etzel, J., Friedlaender, F., 1985. Heavy metals removal by high gradient magnetic separation. IEEE Transactions on Magnetics 21 (5), 2062– 2064.

Asselin, M., Drogui, P., Benmoussa, H., Blais, J.-F., 2008. Effectiveness of electrocoagulation process in removing organic compounds from slaughterhouse wastewater using monopolar and bipolar electrolytic cells. Chemosphere 72 (11), 1727–1733.

Asselin, M., Drogui, P., Brar, S.K., Benmoussa, H., Blais, J.-F., 2008. Organics removal in oily bilgewater by electrocoagulation process. Journal of Hazardous Materials 151 (2-3), 446–455.

Bagga, A., Chellam, S., Clifford, D.A., 2008. Evaluation of iron chemical coagulation and electrocoagulation pretreatment for surface water microfiltration. Journal of Membrane Science 309 (1-2), 82–93.

Balasubramanian, N., Kojima, T., Basha, C.A., Srinivasakannan, C., 2009. Removal of arsenic from aqueous solution using electrocoagulation. Journal of Hazardous Materials 167 (1-3), 966–969.

Baltpurvins, K.A., Burns, R.C., Lawrance, G.A., Stuart, A.D., 1996. Effect of pH and Anion

Type on the Aging of Freshly Precipitated Iron(III) Hydroxide Sludges. Environmental Science and Technology 30 (3), 939–944.

Bard, A.J., and Faulkner, L.R., 1980. Electrochemical methods: fundamentals and applications. Wiley, New York.

Beckett, R., Jue, Z., Giddings, J.C., 1987. Determination of molecular weight distributions of fulvic and humic acids using flow field-flow fractionation. Environmental Science and Technology 21 (3), 289–295.

Belleville, P., Jolivet, J.P., Tronc, E., Livage, J., 1992. Crystallization of ferric hydroxide into spinel by adsorption on colloidal magnetite. Journal of Colloid and Interface Science 150 (2), 453–460.

Bisang, J.M., 1991. Theoretical and experimental studies of current distribution in gas-evolving electrochemical reactors with parallel-plate electrodes. Journal of Applied Electrochemistry 21 (9), 760–766.

Bockris, J.O.M., Drazic, D., Despic, A.R., 1961. The electrode kinetics of the deposition and dissolution of iron. Electrochimica Acta 4 (2-4), 325–361.

Bockris, J.O.M., Genshaw, M.A., Brusic, V., Wroblowa, H., 1971. The mechanism of the passivation of iron in neutral solutions: An ellipsometric and coulometric investigation. Electrochimica Acta 16 (11), 1859–1894.

Bond, D.L., Fendorf, S., 2003. Kinetics and Structural Constraints of Chromate Reduction by Green Rusts. Environmental Science and Technology 37 (12), 2750–2757.

Bonin, P.M.L., Odziemkowski, M.S., Reardon, E.J., Gillham, R.W., 2000. In situ identification of carbonate-containing green rust on iron electrodes in solutions simulating groundwater. Journal of Solution Chemistry 29 (10), 1061–1074.

Bratsch, S.G., 1989. Standard electrode potentials and temperature coefficients in water at 298.15 K. J. Phys. Chem. Ref. Data 18 (1), 1–21.

Braul, L., Leader, A., 2001. Water Quality Matters. Agriculture and Agri-Food Canada. May 2001.

Buchanan, W., Roddick, F., Porter, N., Drikas, M., 2005. Fractionation of UV and VUV pretreated natural organic matter from drinking water. Environmental Science and Technology 39 (12), 4647–4654.

Cabán, R., Chapman, T.W., 1976. Rapid computation of current distribution by orthogonal

collocation. Journal of The Electrochemical Society 123, 1036.

Cabrera, L., Gutierrez, S., Menendez, N., Morales, M.P., Herrasti, P., 2008. Magnetite nanoparticles: Electrochemical synthesis and characterization. Electrochimica Acta 53 (8), 3436–3441.

Cañizares, P., Jiménez, C., Martínez, F., Rodrigo, M.A., Sáez, C., 2009. The pH as a key parameter in the choice between coagulation and electrocoagulation for the treatment of wastewaters. Journal of Hazardous Materials 163 (1), 158–164.

Cañizares, P., Jiménez, C., Martínez, F., Sáez, C., Rodrigo, M.A., 2007. Study of the Electrocoagulation Process Using Aluminum and Iron Electrodes. Industrial Engineering Chemistry Research 46 (19), 6189–6195.

Canizares, P., Martinez, F., Carmona, M., Lobato, J., Rodrigo, M.A., 2005. Continuous electrocoagulation of synthetic colloid-polluted wastes. Industrial Engineering Chemistry Research 44 (22), 8171–8177.

Cañizares, P., Martínez, F., Jiménez, C., Lobato, J., Rodrigo, M.A., 2006. Coagulation and Electrocoagulation of Wastes Polluted with Dyes. Environmental Science and Technology 40 (20), 6418–6424

Carmona, M., Khemis, M., Leclerc, J.P., Lapicque, F., 2006. A simple model to predict the removal of oil suspensions from water using the electrocoagulation technique. Chemical Engineering Science 61 (4), 1237–1246.

CDW, 1998. Guidelines for Canada drinking water quality: Summary table. Prepared by the Federal-Provincial-Territorial Committee on Drinking Water of the Federal-Provincial-Territorial Committee on Health and the Environment, Ottawa.

Chantnija, V. A., Drojchenkova, G.P. 1998. Method of treating natural waters, Inst. Kompleksnogo Osvoenija, RU2721979.

Chen, G., 2004. Electrochemical technologies in wastewater treatment. Separation and Purification Technology 38 (1), 11–41.

Chen, X., Chen, G., Yue, P.L., 2000. Separation of pollutants from restaurant wastewater by electrocoagulation. Separation and Purification Technology 19 (1-2), 65–76.

Chen, X., Chen, G., Yue, P.L., 2002. Investigation on the electrolysis voltage of

electrocoagulation. Chemical Engineering Science 57 (13), 2449–2455.

Chin, Y.P., Gschwend, P.M., 1991. The abundance, distribution, and configuration of porewater organic colloids in recent sediments. Geochimica et Cosmochimica Acta 55 (5), 1309–1317.

Cho, Y., Ji, G., Yoo, P., Kim, C., Han, K., 2008. Comparison of electrocoagulation and chemical coagulation with fiber filters for water treatment. Korean Journal of Chemical Engineering 25 (6), 1326–1330.

Cognot, C., 1995. Electrocoagulation cell for a device for electrolytic purification of waste water, Electricite de France, FR2707282.

Cornell, R.M., Giovanoli, R., Schneider, W., 1989. Review of the hydrolysis of iron(III) and the crystallization of amorphous iron(III) hydroxide hydrate. Journal of Chemical Technology and Biotechnology 46 (2), 115–134.

Cornell, R.M., Schwertmann, U., 2003. The iron oxides: structure, properties, reactions, occurrences, and uses. Wiley, New York.

de Faria, D.L.A., Venâncio Silva, S., de Oliveira, M.T., 1997. Raman microspectroscopy of some iron oxides and oxyhydroxides. Journal of Raman Spectroscopy 28 (11), 873–878.

Dunnwald, J., Otto, A., 1989. An investigation of phase transitions in rust layers using Raman spectroscopy. Corrosion science 29 (9), 1167–1176.

Edzwald, J.K., 1993. Coagulation in drinking water treatment: particles, organics and coagulants. Water Science and Technology 27 (11), 21–35.

Edzwald, J.K., 1994. Coagulation concepts for removal of TOC. In: Proc. AWWA WQTC Conf., San Francisco, CA.

Emamjomeh, M.M., Sivakumar, M., 2009. Fluoride removal by a continuous flow electrocoagulation reactor. Journal of Environmental Management 90 (2), 1204–1212.

Essadki, A.H., Gourich, B., Vial, C., Delmas, H., Bennajah, M., 2009. Defluoridation of drinking water by electrocoagulation/electroflotation in a stirred tank reactor with a comparative performance to an external-loop airlift reactor. Journal of Hazardous Materials 168 (2-3), 1325–1333.

Fischer, P., Heitbaum, J., 1980. Mechanistic aspects of cathodic oxygen reduction. Journal of Electroanalytical Chemistry and Interfacial Electrochemistry 112 (2), 231–238.

Ford, R.G., 2002. Rates of hydrous ferric oxide crystallization and the influence on coprecipitated arsenate. Environmental Science and Technology 36 (11), 2459–2463.

Fouad, Y.O.A., Konsowa, A.H., Farag, H.A., Sedahmed, G.H., 2009. Performance of an electrocoagulation cell with horizontally oriented electrodes in oil separation compared to a cell with vertical electrodes. Chemical Engineering Journal 145 (3), 436–440.

Franger, S., Berthet, P., Berthon, J., 2004. Electrochemical synthesis of Fe_3O_4 nanoparticles in alkaline aqueous solutions containing complexing agents. Journal of Solid State Electrochemistry 8 (4), 218–223.

Franger, S., Berthet, P., Dragos, O., Baddour-Hadjean, R., Bonville, P., Berthon, J., 2006. Large influence of the synthesis conditions on the physico-chemical properties of nanostructured Fe_3O_4. Journal of Nanoparticle Research 9 (3), 389–402.

Frimmel, F.H., Huber, L., 1996. Influence of humic substances on the aquatic adsorption of heavy metals on defined mineral phases. Environment International 22 (5), 507–517.

Funk, J.E., Thorpe, J.F., 1969. Void fraction and current density distributions in a water electrolysis cell. Journal of The Electrochemical Society 116, 48.

Gardner C., 1996. Method for removing contaminants from an aqueous medium. Recra Environmental, US5558755.

Génin, J.-M.R., Refait, P., Bourrié, G., Abdelmoula, M., Trolard, F., 2001. Structure and stability of the Fe(II)–Fe(III) green rust "fougerite" mineral and its potential for reducing pollutants in soil solutions. Applied Geochemistry 16 (5), 559–570.

Ghernaout, D., Badis, A., Kellil, A., Ghernaout, B., 2008. Application of electrocoagulation in Escherichia coli culture and two surface waters. Desalination 219 (1-3), 118–125.

Ghosh, D., Solanki, H., Purkait, M.K., 2008. Removal of Fe (II) from tap water by electrocoagulation technique. Journal of Hazardous Materials 155 (1-2), 135–143.

Golder, A.K., Samanta, A.N., Ray, S., 2007. Removal of Cr^{3+} by electrocoagulation with multiple electrodes: Bipolar and monopolar configurations. Journal of Hazardous Materials 141 (3), 653–661.

Gomes, J.A., Daida, P., Kesmez, M., Weir, M., Moreno, H., Parga, J.R., Irwin, G., McWhinney, H., Grady, T., Peterson, E., 2007. Arsenic removal by electrocoagulation using combined Al–Fe electrode system and characterization of products. Journal of Hazardous Materials 139 (2), 220–231.

Grubisic, Z., Rempp, P., Benoit, H., 1967. A universal calibration for Gel Permeation Chromatography. Journal of Polymer Science (5), 753-759.

Gu, B., Schmitt, J., Chen, Z., Liang, L., McCarthy, J.F., 1994. Adsorption and desorption of natural organic matter on iron oxide: mechanisms and models. Environmental Science and Technology 28 (1), 38–46.

Gu, Z., Liao, Z., Schulz, M., Davis, J.R., Baygents, J.C., Farrell, J., 2009. Estimating Dosing Rates and Energy Consumption for Electrocoagulation Using Iron and Aluminum Electrodes. Industrial Engineering Chemistry Research 48 (6), 3112–3117.

Gui, J., Devine, 1993. Proceedings of the 12th Int. Corrosion Conference. NACE International, Houston. 2052.

Gui, J., Devine, T.M., 1995. A SERS investigation of the passive films formed on iron in mildly alkaline solutions of carbonate/bicarbonate and nitrate. Corrosion Science 37 (8), 1177–1189.

Gupta, A.K., Gupta, M., 2005. Synthesis and surface engineering of iron oxide nanoparticles for biomedical applications. Biomaterials 26 (18), 3995–4021.

Hansen, H.K., Núnez, P., Grandon, R., 2006. Electrocoagulation as a remediation tool for wastewaters containing arsenic. Minerals Engineering 19 (5), 521–524.

Heidmann, I., Calmano, W., 2008. Removal of Cr (VI) from model wastewaters by electrocoagulation with Fe electrodes. Separation and Purification Technology 61 (1), 15–21.

Hem, J.D., 1985. Study and interpretation of the chemical characteristics of natural water. Dept. of the Interior, US Geological Survey.

Holt, P.K., Barton, G.W., Wark, M., Mitchell, C.A., 2002. A quantitative comparison between chemical dosing and electrocoagulation. Colloids and Surfaces A: Physicochemical and Engineering Aspects 211 (2-3), 233–248.

Hong, S., Elimelech, M., 1997. Chemical and physical aspects of natural organic matter (NOM) fouling of nanofiltration membranes. Journal of Membrane Science 132 (2), 159–

181.

Hsing, H.J., Chiang, P.C., Chang, E.E., Chen, M.Y., 2007. The decolorization and mineralization of Acid Orange 6 azo dye in aqueous solution by advanced oxidation processes: A comparative study. Journal of Hazardous Materials 141 (1), 8–16.

Hu, C.Y., Lo, S.L., Kuan, W.H., 2003. Effects of co-existing anions on fluoride removal in electrocoagulation (EC) process using aluminum electrodes. Water Research 37 (18), 4513–4523.

Hu, C.Y., Lo, S.L., Kuan, W.H., 2005. Effects of the molar ratio of hydroxide and fluoride to Al (III) on fluoride removal by coagulation and electrocoagulation. Journal of Colloid and Interface Science 283 (2), 472–476.

Hu, C.Y., Lo, S.L., Kuan, W.H., 2007. Simulation the kinetics of fluoride removal by electrocoagulation (EC) process using aluminum electrodes. Journal of Hazardous Materials 145 (1-2), 180–185.

Ibrahim, M., Serrano, K.G., Noe, L., Garcia, C., Verelst, M., 2009. Electro-precipitation of magnetite nanoparticles: An electrochemical study. Electrochimica Acta 55 (1), 155–158.

Izquierdo, C.J., Canizares, P., Rodrigo, M.A., Leclerc, J.P., Valentin, G., Lapicque, F., 2010. Effect of the nature of the supporting electrolyte on the treatment of soluble oils by electrocoagulation. Desalination 255 (1–3), 15–20.

Jiang, J.Q., Graham, N., Andre, C., Kelsall, G.H., Brandon, N., 2002. Laboratory study of electro-coagulation–flotation for water treatment. Water Research 36 (16), 4064–4078.

Keiser, J.T., Brown, C.W., Heidersbach, R.H., 1983. Characterization of the passive film formed on weathering steels. Corrosion Science 23 (3), 251–259.

Kelsall, G.H., 1984. Hypochlorite electro-generation. I. A parametric study of a parallel plate electrode cell. Journal of Applied Electrochemistry 14 (2), 177–186.

Khataee, A.R., Pons, M.N., Zahraa, O., 2009. Photocatalytic degradation of three azo dyes using immobilized TiO_2 nanoparticles on glass plates activated by UV light irradiation: Influence of dye molecular structure. Journal of Hazardous Materials 168 (1), 451–457.

Khemis, M., Leclerc, J.P., Tanguy, G., Valentin, G., Lapicque, F., 2006. Treatment of industrial liquid wastes by electrocoagulation: Experimental investigations and an overall interpretation model. Chemical Engineering Science 61 (11), 3602–3609.

Kim, J., 2006. Electrochemical oxidation of representative inorganic and organic contaminants in an in situ electrochemical reactor. Ph.D. thesis. University of Washington, Seattle, WA, USA.

Kim, T.H., Park, C., Shin, E.B., Kim, S., 2002. Decolorization of disperse and reactive dyes by continuous electrocoagulation process. Desalination 150 (2), 165–175.

Koparal, A.S., Yildiz, Y.S., Keskinler, B., Demircioglu, N., 2008. Effect of initial pH on the removal of humic substances from wastewater by electrocoagulation. Separation and Purification Technology 59 (2), 175–182.

Kreysa, G., Kuhn, M., 1985. Modelling of gas evolving electrolysis cells. I. The gas voidage problem. Journal of Applied Electrochemistry 15 (4), 517–526.

Kul'skii, L. A., Strokach, P. P., Slipchenko, V. A., and Saigak, E. I. 1978. Water Purification by Electrocoagulation. Kiev, Budivel'nik.

Kumar, N.S., Goel, S., 2010. Factors influencing arsenic and nitrate removal from drinking water in a continuous flow electrocoagulation (EC) process. Journal of Hazardous Materials 173 (1-3), 528–533.

Lakshmanan, D., Clifford, D.A., Samanta, G., 2009. Ferrous and Ferric Ion Generation During Iron Electrocoagulation. Environmental Science and Technology 43 (10), 3853–3859.

Larue, O., Vorobiev, E., 2003. Floc size estimation in iron induced electrocoagulation and coagulation using sedimentation data. International Journal of Mineral Processing 71 (1-4), 1–15.

Larue, O., Vorobiev, E., Vu, C., Durand, B., 2003. Electrocoagulation and coagulation by iron of latex particles in aqueous suspensions. Separation and Purification Technology 31 (2), 177–192.

Lazarevich, K.L. and Isaakovich, M.M., 1967. Purification of waste water by electrocoagulation, Lab biophysiki i isotopov, GB1067746.

Lee, J., Selman, J.R., 1982. Effects of Separator and Terminal on the Current Distribution in Parallel-Plate Electrochemical Flow Reactors. Journal of The Electrochemical Society 129, 1670.

Lee, W.J., Pyun, S.I., 2000. Effects of sulphate ion additives on the pitting corrosion of pure

aluminium in 0.01 M NaCl solution. Electrochimica Acta 45 (12), 1901–1910.

Lefebvre, E., Legube, B., 1990. Iron (III) coagulation of humic substances extracted from surface waters: effect of pH and humic substances concentration. Water Research 24 (5), 591–606.

Legrand, L., Mazerolles, L., Chaussé, A., 2004. The oxidation of carbonate green rust into ferric phases:solid-state reaction or transformation via solution. Geochimica et Cosmochimica Acta 68 (17), 3497–3507.

Legrand, L., Sagon, G., Lecomte, S., Chausse, A., Messina, R., 2001. A Raman and infrared study of a new carbonate green rust obtained by electrochemical way. Corrosion Science 43 (9), 1739–1749.

Levich, V. G., 1962. Physicochemical Hydrodynamics. Prentice-Hall, Englewood Cliffs.

Li, T., Zhu, Z., Wang, D., Yao, C., Tang, H., 2006. Characterization of floc size, strength and structure under various coagulation mechanisms. Powder Technology 168 (2), 104–110.

Li, Y., Wang, J., Zhao, Y., Luan, Z., 2010. Research on magnetic seeding flocculation for arsenic removal by superconducting magnetic separation. Separation and Purification Technology 73 (2), 264–270.

Liang, L., McNabb, J.A., Paulk, J.M., Gu, B., McCarthy, J.F., 1993. Kinetics of iron (II) oxygenation at low partial pressure of oxygen in the presence of natural organic matter. Environmental Science and Technology 27 (9), 1864–1870.

Liang, L., Singer, P.C., 2003. Factors Influencing the Formation and Relative Distribution of Haloacetic Acids and Trihalomethanes in Drinking Water. Environmental Science and Technology 37 (13), 2920–2928.

Linares-Hernández, I., Barrera-Díaz, C., Roa-Morales, G., Bilyeu, B., Ureña-Núñez, F., 2009. Influence of the anodic material on electrocoagulation performance. Chemical Engineering Journal 148 (1), 97–105.

Liu, H., Hihara, T., Sumiyama, K., Suzuki, K., 1998. Magnetic viscosity of fine maghemite clusters prepared by electrochemical method. Physica Status Solidi (a) 169 (1), 153–160.

Malcolm, R.L., 1993. Concentration and composition of dissolved organic carbon in soils, streams, and groundwaters. Special Publication of the Royal Society of Chemistry 135, 19–

30.

Mameri, N., Lounici, H., Belhocine, D., Grib, H., Piron, D.L., Yahiat, Y., 2001. Defluoridation of Sahara water by small plant electrocoagulation using bipolar aluminium electrodes. Separation and Purification Technology 24 (1-2), 113–119.

Mameri, N., Yeddou, A.R., Lounici, H., Belhocine, D., Grib, H., Bariou, B., 1998. Defluoridation of septentrional Sahara water of North Africa by electrocoagulation process using bipolar aluminium electrodes. Water Research 32 (5), 1604–1612.

Marques, R.F.C., Garcia, C., Lecante, P., Ribeiro, S.J.L., Noé, L., Silva, N.J.O., Amaral, V.S., Millán, A., Verelst, M., 2008. Electro-precipitation of Fe_3O_4 nanoparticles in ethanol. Journal of Magnetism and Magnetic Materials 320 (19), 2311–2315.

Martinez-Villafane, J.F., Montero-Ocampo, C., García-Lara, A.M., 2009. Energy and electrode consumption analysis of electrocoagulation for the removal of arsenic from underground water. Journal of Hazardous Materials 172 (2), 1617–1622.

Matilainen, A., Lindqvist, N., Tuhkanen, T., 2005. Comparison of the Effiency of Aluminium and Ferric Sulphate in the Removal of Natural Organic Matter During Drinking Water Treatment Process. Environmental Technology 26 (8), 867–876.

Matteson, M.J., Dobson, R.L., Glenn, R.W., Kukunoor, N.S., Waits, W.H., Clayfield, E.J., 1995. Electrocoagulation and separation of aqueous suspensions of ultrafine particles. Colloids and Surfaces A: Physicochemical and Engineering Aspects 104 (1), 101–109.

Mayer, T.D., Jarrell, W.M., 2000. Phosphorus sorption during iron (II) oxidation in the presence of dissolved silica. Water Research 34 (16), 3949–3956.

McGill, I.R., McEnaney, B., Smith, D.C., 1976. Crystal structure of green rust formed by corrosion of cast iron. , Nature 259 (5540), 200–201.

Mechelhoff, M., 2009. Electrochemical investigation of electrocoagulation reactors for water purification. Ph.D. thesis. Imperial College, London, U.K.

Mills, D., 2000. A new process for electrocoagulation. Journal American Water Works Association 92 (6), 34–43.

Misawa, T., Hashimoto, K., Shimodaira, S., 1974. The mechanism of formation of iron oxide and oxyhydroxides in aqueous solutions at room temperature. Corrosion Science 14 (2), 131–149.

Mollah, M.Y.., Morkovsky, P., Gomes, J.A.., Kesmez, M., Parga, J., Cocke, D.L., 2004. Fundamentals, present and future perspectives of electrocoagulation. Journal of Hazardous Materials 114 (1-3), 199–210.

Mollah, M.Y.., Schennach, R., Parga, J.R., Cocke, D.L., 2001. Electrocoagulation (EC)—science and applications. Journal of Hazardous Materials 84 (1), 29–41.

Moreno C., H.A., Cocke, D.L., Gomes, J.A.G., Morkovsky, P., Parga, J.R., Peterson, E., Garcia, C., 2009. Electrochemical Reactions for Electrocoagulation Using Iron Electrodes. Industrial Engineering Chemistry Research 48 (4), 2275–2282.

Moreno, H.A., Cocke, D.L., Gomes, J.A., Morkovsky, P., Parga, J., Peterson, E., Garcia, C., 2007. Electrochemical Generation of Green Rust using Electrocoagulation. ECS Transactions 210, Cancun, Mexico.

Moreno-Casillas, H.A., Cocke, D.L., Gomes, J.A.G., Morkovsky, P., Parga, J.R., Peterson, E., 2007. Electrocoagulation mechanism for COD removal. Separation and Purification Technology 56 (2), 204–211.

Mouedhen, G., Feki, M., Wery, M.D.P., Ayedi, H.F., 2008. Behavior of aluminum electrodes in electrocoagulation process. Journal of Hazardous Materials 150 (1), 124–135.

Noubactep, C., 2010. The suitability of metallic iron for environmental remediation. Environmental Progress and Sustainable Energy 29 (3), 286–291.

Odziemkowski, M., Flis, J., Irish, D.E., 1994. Raman spectral and electrochemical studies of surface film formation on iron and its alloys with carbon in $Na_2CO_3/NaHCO_3$ solution with reference to stress corrosion cracking. Electrochimica Acta 39 (14), 2225–2236.

Odziemkowski, M.S., Schuhmacher, T.T., Gillham, R.W., Reardon, E.J., February. Mechanism of oxide film formation on iron in simulating groundwater solutions: Raman spectroscopic studies. Corrosion Science 40 (2-3), 371–389.

Oelner, W., Berthold, F., Guth, U., 2006. The iR drop - well-known but often underestimated in electrochemical polarization measurements and corrosion testing. Materials and Corrosion 57 (6), 455–466.

Parga, J.R., Cocke, D.L., Valenzuela, J.L., Gomes, J.A., Kesmez, M., Irwin, G., Moreno, H., Weir, M., 2005. Arsenic removal via electrocoagulation from heavy metal contaminated groundwater in La Comarca Lagunera México. Journal of Hazardous Materials 124 (1-3),

247–254.

Parga, J.R., Cocke, D.L., Valverde, V., Gomes, J.A.G., Kesmez, M., Moreno, H., Weir, M., Mencer, D., 2005. Characterization of Electrocoagulation for Removal of Chromium and Arsenic. Chemical Engineering and Technology 28 (5), 605–612.

Parrish, W.R., Newman, J., 1969. Current distribution on a plane electrode below the limiting current. Journal of The Electrochemical Society 116, 169.

Pascal, C., Pascal, J.L., Favier, F., Elidrissi Moubtassim, M.L., Payen, C., 1999. Electrochemical Synthesis for the Control of γ-Fe_2O_3 Nanoparticle Size. Morphology, Microstructure, and Magnetic Behavior. Chemistry of Materials 11 (1), 141–147.

Pelekani, C., Newcombe, G., Snoeyink, V.L., Hepplewhite, C., Assemi, S., Beckett, R., 1999. Characterization of natural organic matter using high performance size exclusion chromatography. Environmental Science and Technology 33 (16), 2807–2813.

Pickett, D.J., Ong, K.L., 1974. The influence of hydrodynamic and mass transfer entrance effects on the operation of a parallel plate electrolytic cell. Electrochimica Acta 19 (12), 875–882.

Pikkarainen, A.T., Judd, S.J., Jokela, J., Gillberg, L., 2004. Pre-coagulation for microfiltration of an upland surface water. Water Research 38 (2), 455–465.

Pouet, M.-F., Grasmick, A., 1994. Electrocoagulation and flotation: Applications in crossflow microfiltration. Filtration and Separation 31 (3), 269–272.

Pouet, M.F., Grasmick, A., 1995. Urban wastewater treatment by electrocoagulation and flotation. Water Science and Technology 31 (3), 275–283.

Randtke, S.J., 1993. Coagulation of NOM: an overview of the science and US practice. AWWA Proc. Workshop on NOM in Drinking Water.

Ratna Kumar, P., Chaudhari, S., Khilar, K.C., Mahajan, S.., 2004. Removal of arsenic from water by electrocoagulation. Chemosphere 55 (9), 1245–1252.

Reckhow, D.A., Rees, P.L., Nüsslein, K., Makdissy, G., Devine, G., Conneely, T., Boutin, A., Bryan, D., 2008. Long-term Variability of BDOM and NOM as Precursors in Watershed Sources. Water Intelligence Online 7 (1).

Refait, P., Abdelmoula, M., Génin, J.-M.R., 1998. Mechanisms of formation and structure of

green rust one in aqueous corrosion of iron in the presence of chloride ions. Corrosion Science 40 (9), 1547–1560.

Refait, P., Drissi, S.H., Pytkiewicz, J., Génin, J.-M.R., 1997. The anionic species competition in iron aqueous corrosion: Role of various green rust compounds. Corrosion Science 39 (9), 1699–1710.

Refait, P., Memet, J.-B., Bon, C., Sabot, R., Génin, J.-M.., 2003. Formation of the Fe(II)–Fe(III) hydroxysulphate green rust during marine corrosion of steel. Corrosion Science 45 (4), 833–845.

Ryan, D., Gadd, A., Kavanagh, J., Zhou, M., Barton, G., 2008. A comparison of coagulant dosing options for the remediation of molasses process water. Separation and Purification Technology 58 (3), 347–352.

Sanfan, W., 1991. Studies on economic property of pretreatment process of brackish water using electrocoagulation (EC) method. Desalination 82 (1-3), 359–363.

Sarathy, S.R., Mohseni, M., 2007. The Impact of UV/H2O2 Advanced Oxidation on Molecular Size Distribution of Chromophoric Natural Organic Matter. Environmental Science and Technology 41 (24), 8315–8320.

Sarin, P., Snoeyink, V.L., Bebee, J., Jim, K.K., Beckett, M.A., Kriven, W.M., Clement, J.A., 2004. Iron release from corroded iron pipes in drinking water distribution systems: effect of dissolved oxygen. Water Research 38 (5), 1259–1269.

Sass, B.M., Rai, D., 1987. Solubility of amorphous chromium (III)-iron (III) hydroxide solid solutions. Inorganic Chemistry 26 (14), 2228–2232.

Sasson, M.B., Adin, A., 2010. Fouling mitigation by iron-based electroflocculation in microfiltration: Mechanisms and energy minimization. Water Research 44 (13), 3973–3981.

Sasson, M.B., Calmano, W., Adin, A., 2009. Iron-oxidation processes in an electroflocculation (electrocoagulation) cell. Journal of Hazardous Materials 171 (1-3), 704–709.

Schmitt-Kopplin, P., Garrison, A.W., Perdue, E.M., Freitag, D., Kettrup, A., 1998. Capillary electrophoresis in the analysis of humic substances: Facts and artifacts. Journal of Chromatography A 807 (1), 101–109.

Schulten, H.R., Schnitzer, M., 1993. A state of the art structural concept for humic

substances. Naturwissenschaften 80 (1), 29–30.

Schwertmann, U., 1966. Inhibitory Effect of Soil Organic Matter on the Crystallization of Amorphous Ferric Hydroxide. Nature 212 (5062) 645–646.

Shen, F., Chen, X., Gao, P., Chen, G., February. Electrochemical removal of fluoride ions from industrial wastewater. Chemical Engineering Science 58 (3-6), 987–993.

Song, S., Lopez-Valdivieso, A., Hernandez-Campos, D.J., Peng, C., Monroy-Fernandez, M.G., Razo-Soto, I., 2006. Arsenic removal from high-arsenic water by enhanced coagulation with ferric ions and coarse calcite. Water Research 40 (2), 364–372.

Spicer, P.T., Pratsinis, S.E., 1996. Shear-induced flocculation: the evolution of floc structure and the shape of the size distribution at steady state. Water Research 30 (5), 1049–1056.

Stuart, F.E., 1946. Electronic water purification progress report on the electronic coagulator—a new device which gives promise of unusually speedy and effective results. Water Sewage 84, 24–26.

Stumm, W., Lee, G.F., 1961. Oxygenation of ferrous iron. Industrial and Engineering Chemistry 53 (2), 143–146.

Stumm, W., Morgan, J.J., 1962. Chemical aspects of coagulation. Journal of the American Water Works Association 54 (8) 971-974.

Sung, W., Morgan, J.J., 1980. Kinetics and product of ferrous iron oxygenation in aqueous systems. Environmental Science and Technology 14 (5), 561–568.

Tamaura, Y., Ito, K., Katsura, T., 1983. Transformation of gamma-FeO (OH) to Fe_3O_4 by adsorption of iron (II) ion on gamma-FeO (OH). Journal of the Chemical Society., Dalton Transactions (2), 189–194.

Tamura, H., Kawamura, S., Hagayama, M., 1980. Acceleration of the oxidation of Fe^{2+} ions by Fe (III)-oxyhydroxides. Corrosion Science 20 (8-9), 963–971.

Tanneru, C.T., Chellam, S., 2012. Mechanisms of virus control during iron electrocoagulation – Microfiltration of surface water. Water Research 46 (7), 2111–2120.

Theis, T.L., Singer, P.C., 1974. Complexation of iron(II) by organic matter and its effect on iron(II) oxygenation. Environmental Science and Technology 8 (6), 569–573.

Timmes, T.C., Kim, H.-C., Dempsey, B.A., 2009. Electrocoagulation pretreatment of

seawater prior to ultrafiltration: Bench-scale applications for military water purification systems. Desalination 249 (3), 895–901.

Tombacz, E., Dobos, A., Szekeres, M., Narres, H.D., Klumpp, E., Dekany, I., 2000. Effect of pH and ionic strength on the interaction of humic acid with aluminium oxide. Colloid and Polymer Science 278 (4), 337–345.

Tsouris, C., DePaoli, D.W., Shor, J.T., Hu, M.Z.C., Ying, T.Y., 2000. Electrocoagulation for magnetic seeding of colloidal particles. Colloids and Surfaces A: Physicochemical and Engineering Aspects 177 (2-3), 223–233.

United Nations Environment Programme. 2007. Global Environment Outlook 4: Environment for Development. Malta.

USEPA, E.C., Manual, E.P.S., 1998. SDWR Part IV, Federal Register. EPA. Office of Water and Drinking Ground Water, Washington, DC 20–50.

van Benschoten, J.E., Edzwald, J.K., 1990. Chemical aspects of coagulation using aluminum salts–II. coagulation of fulvic acid using alum and polyaluminum chloride. Water Research 24 (12), 1527–1535.

van Genuchten, C.M., Addy, S.E.., Pena, J., Gadgil, A., 2011. Removing arsenic from synthetic groundwater with iron electrocoagulation: An Fe and As K-edge EXAFS study. Environmental Science and Technology 46 (2) 986-994.

van Leeuwen, J., Daly, R., Holmes, M., 2005. Modeling the treatment of drinking water to maximize dissolved organic matter removal and minimize disinfection by-product formation. Desalination 176 (1–3), 81–89.

Vasudevan, S., Jayaraj, J., Lakshmi, J., Sozhan, G., 2009. Removal of iron from drinking water by electrocoagulation: Adsorption and kinetics studies. Korean Journal of Chemical Engineering 26 (4), 1058–1064.

Vasudevan, S., Lakshmi, J., Jayaraj, J., Sozhan, G., 2009. Remediation of phosphate-contaminated water by electrocoagulation with aluminium, aluminium alloy and mild steel anodes. Journal of Hazardous Materials 164 (2-3), 1480–1486.

Vepsäläinen, M., Ghiasvand, M., Selin, J., Pienimaa, J., Repo, E., Pulliainen, M., Sillanpää, M., 2009. Investigations of the effects of temperature and initial sample pH on natural organic matter (NOM) removal with electrocoagulation using response surface method

(RSM). Separation and Purification Technology 69 (3), 255–261.

Vik, E.A., Carlson, D.A., Eikum, A.S., Gjessing, E.T., 1984. Electrocoagulation of potable water. Water Research 18 (11).

Villalobos, M., Leckie, J.O., 2000. Carbonate adsorption on goethite under closed and open CO2 conditions. Geochimica et Cosmochimica Acta 64 (22), 3787–3802.

Vogt, H., 1987. The voidage problem in gas-electrolyte dispersions. Journal of Applied Electrochemistry 17 (2), 419–426.

Wagner, C., 1951. Theoretical analysis of the current density distribution in electrolytic cells. Journal of the Electrochemical Society 98, 116.

Wander, M.C.F., Rosso, K.M., Schoonen, M.A.A., 2007. Structure and Charge Hopping Dynamics in Green Rust. The Journal of Physical Chemistry C 111 (30), 11414–11423.

Weijs, M., Janssen, L.J.J., Visser, G.J., 1997. Ohmic resistance of solution in a vertical gas-evolving cell. Journal of Applied Electrochemistry 27 (4), 371–378.

Weintraub, M.H., Gealer, R.L., Golovoy, A., Dzieciuch, M.A., Durham, H., 1983. Development of electrolytic treatment of oily wastewater. Environmental Progress 2 (1), 32–37.

Weng, Y.-C., Rusakova, I.A., Baikalov, A., Chen, J.W., Wu, N.-L., 2005. Microstructural evolution of nanocrystalline magnetite synthesized by electrocoagulation. Journal of Materials Research 20 (1), 75–80.

West, J.M.,1986. Basic Corrosion and Oxidation. Wiley, New York.

White, R.E., Bain, M., Raible, M., 1983. Parallel plate electrochemical reactor model. Journal of the Electrochemical Society 1037.

Wilkie, J.A., Hering, J.G., 1996. Adsorption of arsenic onto hydrous ferric oxide: effects of adsorbate/adsorbent ratios and co-occurring solutes. Colloids and Surfaces A: Physicochemical and Engineering Aspects 107, 97–110.

Williams, A.G.B., Scherer, M.M., 2001. Kinetics of Cr(VI) Reduction by Carbonate Green Rust. Environmental Science and Technology 35 (17), 3488–3494.

Williams, A.G.B., Scherer, M.M., 2004. Spectroscopic Evidence for Fe(II)−Fe(III) Electron

Transfer at the Iron Oxide−Water Interface. Environmental Science and Technology 38 (18), 4782–4790.

Wu, C.-H., Chang, C.-L., Kuo, C.-Y., 2008. Decolorization of Procion Red MX-5B in electrocoagulation (EC), UV/TiO_2 and ozone-related systems. Dyes and Pigments 76 (1), 187–194.

Yang, G.C.C., Tsai, C.-M., 2006. Performance evaluation of a simultaneous electrocoagulation and electrofiltration module for the treatment of Cu-CMP and oxide-CMP wastewaters. Journal of Membrane Science 286 (1-2), 36–44.

Yavuz, C.T., Mayo, J.T., Yu, W.W., Prakash, A., Falkner, J.C., Yean, S., Cong, L., Shipley, H.J., Kan, A., Tomson, M., 2006. Low-field magnetic separation of monodisperse Fe_3O_4 nanocrystals. Science 314 (5801), 964.

Yildiz, Y.S., Koparal, A.S., Keskinler, B., 2008. Effect of initial pH and supporting electrolyte on the treatment of water containing high concentration of humic substances by electrocoagulation. Chemical Engineering Journal 138 (1-3), 63–72.

Zhang, Z., Zhang, Q., Xu, L., Xia, Y., 2007. Preparation of Nanometer γ-Fe_2O_3 by an Electrochemical Method in Non-aqueous Medium and Reaction Dynamics. Synthesis and Reactivity in Inorganic, Metal-Organic, and Nano-Metal Chemistry 37 (1), 53.

Zhao, H., Zhao, B., Yang, W., Li, T., 2010. Effects of Ca^{2+} and Mg^{2+} on Defluoridation in the Electrocoagulation Process. Environ. Sci. Technol. 44 (23), 9112–9116.

Zhao, H.Z., Yang, W., Zhu, J., Ni, J.R., 2009. Defluoridation of drinking water by combined electrocoagulation: Effects of the molar ratio of alkalinity and fluoride to Al(III). Chemosphere 74 (10), 1391–1395.

Zhou, Q., Cabaniss, S.E., Maurice, P.A., 2000. Considerations in the use of high-pressure size exclusion chromatography (HPSEC) for determining molecular weights of aquatic humic substances. Water Research 34 (14), 3505–3514.

Zhu, B., Clifford, D.A., Chellam, S., 2005. Comparison of electrocoagulation and chemical coagulation pretreatment for enhanced virus removal using microfiltration membranes. Water Research 39 (13), 3098–3108.

Zhu, J., Zhao, H., Ni, J., 2007. Fluoride distribution in electrocoagulation defluoridation process. Separation and Purification Technology 56 (2), 184–191.

Zodi, S., Potier, O., Lapicque, F., Leclerc, J.-P., 2009. Treatment of the textile wastewaters by electrocoagulation: Effect of operating parameters on the sludge settling characteristics. Separation and Purification Technology 69 (1), 29–36.

Zongo, I., Leclerc, J.-P., Maïga, H.A., Wéthé, J., Lapicque, F., 2009. Removal of hexavalent chromium from industrial wastewater by electrocoagulation: A comprehensive comparison of aluminium and iron electrodes. Separation and Purification Technology 66 (1), 159–166.

Zongo, I., Maiga, A.H., Wéthé, J., Valentin, G., Leclerc, J.-P., Paternotte, G., Lapicque, F., 2009. Electrocoagulation for the treatment of textile wastewaters with Al or Fe electrodes: Compared variations of COD levels, turbidity and absorbance. Journal of Hazardous Materials 169 (1-3), 70–76.

Appendices

Appendix A – MATLAB Numerical Model Code

```
% This code calculates cell current based on equipotential polarization in an
% electrocoagulation reactor.
% Kristian Dubrawski, 2012 PhD Thesis
% University of British Columbia, Vancouver, British Columbia, Canada

clear all;
clc;

syms iy;

% Variables:

% R (J/molK), F (C/mol), z (dim), cp (J/(g*deg_C))
R=8.314472;
F=96485.339;
z=2;
cp=4.1813;
const=2.303;

% w is width of electrode (m)
w=0.038;

% d is inter-electrode gap (m)
d=0.002;

% l is overall length of electrode (m)
l=0.240;

% A_xc is cross sectional area (m)
A_xc=d*w;

% n is the number of vertical segmentations (dim)
n=12;

% dy is thickness of each segment (m)
dy=l/n;

% dV is differential volume (m^3)
dV=dy*A_xc;

% dm is mass of differential volume (g)
dm=dV*(100^3);

% dA is electrode area of each segment (m)
dA=dy*w;
```

```
% V is volumetric flow rate (m3/s);
V_L=0.3; %(L/min)
V=V_L/1000/60;

% U is initial average velocity (m/s);
U=V/A_xc;

% tau is residence time of water contacting segment [s]
tau=dy/U;

% initial temperature (K)
T(n)=zeros;
T(1)=293.15;

% initial liquid fraction (dim)
phi(n)=zeros;
phi(1)=1;

%initial ionic activities, (Mechelhoff, 2008) H2 at atmospheric,
%"The rate of hydrogen generation" (Vogt, 1982)

OH(n)=zeros;
OH(:)=0.001;
prH2(n)=zeros;
prH2(:)=1;
Fe2(n)=zeros;
Fe2(:)=0.0005;

% Equilibrium cell potentials (V)
Ea0= -0.41;
Ec0= -0.83;

% Entropy Temp coefficient (V/K)
delSa=0.00007;
delSc=-0.000836;

% Fe -> Fe(II) + 2e-  (A/m2)
i0a=0.00025;
ba=0.093;

% 2 H2O + 2e-  -> 1/2 H2 + 2 OH-  (A/m2) (Cojocaru et al., romania, 2009 -on Fe metal)
%(J.West, Basic Corrosion & Oxidation, pg. 82, on Fe metal)
i0c=0.001;
bc=0.164;

% Tafel parameters from a=-b log(i0)
ac=-bc*log10(i0c);
aa=-ba*log10(i0a);

% initial conductivity (S/m)

% Na2SO4:
% 50 mg/L ---> 0.0110
```

```
% 150 mg/L ---> 0.0312
% 500 mg/L ---> 0.1040

% NaCl:
% 50 mg/L ---> 0.0132
% 150 mg/L ---> 0.0410
% 500 mg/L ---> 0.1325


k(n+1)=zeros;
k(1) = 0.0110;

% conductivity/temperature slope (S/mK)

% Na2SO4:
% 50 mg/L ---> 0.027775
% 150 mg/L ---> 0.030159
% 500 mg/L ---> 0.030129
% NaCl:
% 50 mg/L ---> 0.03388
% 150 mg/L ---> 0.028479
% 500 mg/L ---> 0.025897

c_alpha=0.027775;

% E_cell is the potential across the metal side (V)
E_cell=[2 3 5 10 15 20];
E_len=length(E_cell);

% initialize currents
iy(n)=zeros;
c_tot(E_len)=zeros;
H_tot(n)=zeros;


for b = 1:E_len

 for j = 1:n

      % Finds the non-equilibrium potential with Nernst (V)
      Ec=(Ec0+delSc*(T(j)-298))-(R*T(j)/(z*F))*log(OH(j)^2*prH2(j));
      Ea=(Ea0+delSa*(T(j)-298))-(R*T(j)/(z*F))*log(1/Fe2(j));

      iy(j)=solve('-E_cell(b)= Ec-Ea-(bc*1/const*log(iy)+ac)-(ba*1/const*log(iy)+aa)-(iy*d/k(j))','iy');

      % Calculates current density at stage j (A/m2)
      c_density_dy(j) = eval(iy(j));

      % Calculates current at stage j (A)
      c_dy(j)=c_density_dy(j)*dA;

      % Sums current across j segments (A)
      c_tot(b)=c_tot(b)+c_dy(j);
```

```
        % H_dot is rate of molar evolution (mol/s)
        H_dot(j)=c_dy(j)/(z*F);

        % H_n is the number total moles hydrogen evolved in residence time of differential area (mol)
        H_n(j)=H_dot(j)*tau;

        % H_V is the total volume of hydrogen produced (m^3)
        H_V(j)=H_n(j)*R*T(j)/101300;

        % Phi is the liquid volume fraction (dim)
        phi(j)=1-H_V(j)/dV;

        % Calcualtes overpotential and ohmic voltage (V)
        V_heat(j)=abs((bc*1/const*log(c_density_dy(j))+ac))+abs((ba*1/const*log(c_density_dy(j))+aa))+
        abs((c_density_dy(j)*d/k(j)));

        %Energy balance on constituents calculates temperature change (K)
        T(j+1)=T(j)+(V_heat(j)*c_dy(j))/(cp*dm/tau);

        % Calculates k change based on T and phi
        k(j+1)= k(1)*(1+c_alpha*(T(j+1)-T(1)))*(phi(j)/phi(1))^1.5;

        % Tabulates all k, T, phi, i, V
        t_k(b,j)=k(j);
        t_T(b,j)=T(j);
        t_phi(b,j)=phi(j);
        t_c_density_dy(b,j)=c_density_dy(j);
        t_c_dy(b,j)=c_dy(j);
        t_eqm(b,j)=abs(Ec-Ea);
        t_nc(b,j)=bc/const*log(c_density_dy(j))+ac;
        t_na(b,j)=ba/const*log(c_density_dy(j))+aa;
        t_ir(b,j)=c_density_dy(j)*d/k(j);
        t_Vall(b,j)=t_eqm(b,j)+ t_nc(b,j)+t_na(b,j)+ t_ir(b,j);
        t_nc_percent(b,j)=t_nc(b,j)/t_Vall(b,j);
        t_na_percent(b,j)=t_na(b,j)/t_Vall(b,j);
        t_ir_percent(b,j)=t_ir(b,j)/t_Vall(b,j);

    end
end

% % plots 3,10,20V colormaps (uncomment to see results)
% % Create figure
% axes1 = axes('Parent',figure1,'YTick',[],'XTick',[]);
% % Change colorbar min and max
% cmin=0.13;
% cmax=0.21;
% caxis([cmin cmax])
%
% %Makes matrix for 2nd,4th,6th entry
%
% p_a1=t_k(2,:)';
% % Initial vectors.
```

```
% A = [p_a1'];
% % Values to insert
% Ai = p_a1(1);
% % Insertion process.
% p_a1 = [Ai A]';
%
% p_ax(:,1)=p_a1;
% p_ax(:,2)=p_a1;
% h_1=p_ax;
% subplot(1,10,1,'XTick',zeros(1,0),'YTick',zeros(1,0));
% pcolor(h_1);
% caxis([cmin cmax])
%
% p_a2=t_k(4,:)';
% % Initial vectors.
% A = [p_a2'];
% % Values to insert
% Ai = p_a2(1);
% % Insertion process.
% p_a2 = [Ai A]';
% p_ax(:,1)=p_a2;
% p_ax(:,2)=p_a2;
% h_2=p_ax;
% subplot(1,10,2,'XTick',zeros(1,0),'YTick',zeros(1,0));
% pcolor(h_2);
% caxis([cmin cmax])
%
% p_a3=t_k(5,:)';
% % Initial vectors.
% A = [p_a3'];
% % Values to insert
% Ai = p_a3(1);
% % Insertion process.
% p_a3 = [Ai A]';
%
% p_ax(:,1)=p_a3;
% p_ax(:,2)=p_a3;
% h_3=p_ax;
% subplot(1,10,3,'XTick',zeros(1,0),'YTick',zeros(1,0));
% pcolor(h_3);
% caxis([cmin cmax])
% colorbar('EastOutside')
```

Appendix B – Comparison of EC to CC and Testing of a Bench-scale Pilot

Appendix Synopsis

Electrocoagulation (EC) was used to remove natural organic matter (NOM) from a natural water source (pH_0=6.1, DOC_0=13.3 mg/L) using only immersed iron electrodes and a small amount of electricity. No pH control was used before or after EC, and no conductivity enhancing salt was added to improve EC performance. EC was compared with equivalent iron concentrations of Fe (II) sulfate and Fe (III) sulfate, showing that EC had better DOC removal than Fe (II) sulfate, and essentially the same DOC removal as Fe (III) sulfate at high doses (28.8 mg Fe/L). At lower doses (≤14.4 mg Fe/L), Fe (III) sulfate had approximately 10 % better DOC and UV-abs-254 removal than EC, high performance size exclusion chromatography (HPSEC) confirmed these results, showing greater removal of larger apparent molecular weight (AMW) NOM fractions with iron (III) sulfate than EC at lower iron equivalent doses. A continuous EC bench scale pilot operating at 1-3 L/min showed >80% DOC and 83% UV-abs-254 reductions. Minor improvements in DOC and UV-abs-254 reductions were made when pH was lowered to pH ~ 6 and flocculation increased from 12 to 20 min. The addition of conductivity enhancing salt (NaCl or Na_2SO_4) led to only marginal decreases in operating cost of the bench scale pilot reactor, operating cost estimations for a 4 ML/day EC plant were estimated between $0.07-0.15/1000 L including the distributed cost of electrical transformers and connections.

B.1 Introduction

Electrocoagulation (EC), the *in-situ* generation of charged metal hydroxide coagulant species, has had a recent surge in interest in drinking water treatment as a potential replacement for ubiquitous aluminum and iron salts. EC is often reported as vastly superior to chemical coagulation (CC), including reports of lower sludge production, lower total chemical use, lower overall cost, no pH control necessary, greater pollutant removal, and lower effluent total dissolved solids (Mollah et al., 2001). Yet, due to incomplete understanding of the impact of reactor design on EC electrochemical reactions and power consumption, claims of EC's superiority are still questionable. One of the most common uses of coagulation is the removal of NOM from raw surface waters. NOM has been identified as a precursor to harmful disinfection by-products (DBPs), including suspected carcinogenic substances such as tri-halomethanes (THMs) and halo acetic acids (HAAs) upon contact disinfection and/or coagulation (Liang and Singer, 2003). THM precursors exist even after coagulation (Liang and Singer, 2003), and coagulation generally removals the large apparent molecular weight (AMW) fraction of NOM, quantified by high performance size exclusion chromatography (HPSEC). NOM impacted source waters make an excellent candidate for comparing EC to CC, since the addition of conductivity enhancing salts is prohibitive in drinking water, and true cost and effectiveness can be easily compared.

Most investigations of NOM removal by EC have focus on aluminum anodes (Vik et al., 1984; Jiang et al., 2002; Mechelhoff, 2009; Vepsäläinen et al., 2009). However, an Al_2O_3

passivation layer can negatively affect EC, requiring the addition of sodium chloride to source waters (Mechelhoff, 2009) to circumvent the passivation effect. In Chapter 2 and 3, greater NOM removal was found with an iron anode compared with zinc or aluminum electrodes coupled with direct microfiltration, finding that current density (*i*), and charge loading rate (*CLR*) were the most important EC operational parameters when NaCl was not added to avoid passivation effects. The current study thus had two objectives: *i*) The comparison of iron EC to iron CC in treating natural waters, and ii) the evaluation of an iron EC bench scale pilot, without pH control or the addition of salts.

B.2 Materials and Methods

B.2.1 Waters

Stanley Park (SP) natural water was collected from Lost Lagoon, Stanley Park, Vancouver, Canada as representative poor quality and high DOM source water, raw water characteristics are: DOC_0=13.31 mg/L, UV-abs-254_0=0.560 cm^{-1}, SUVA=4.21, pH=6.1, conductivity (κ)=990 μS/cm, dissolved oxygen (DO)=5.2 mg/L, alkalinity=28 mg/L $CaCO_3$. The natural water was collected in June 2011, without further filtration, pH adjustment, solute addition, or disinfection, and stored at 5°C. All experiments were performed within 1 month of collection.

B.2.2 Electrocoagulation

For EC comparison to CC, a custom 60 mL batch electrolysis chamber was manufactured from inert acrylic. Twelve electrodes were utilized in monopolar connection, six anodes and six cathodes, each with a nominal surface area of 18.65 cm^2 on each side, and an inter-electrode gap of 2 mm. The anode metal grade (McMaster-Carr) was iron 1018, and the cathode was 304 stainless steel. A DC power supply (GW Instek PSP-2010) supplied DC current in galvanostatic mode, connected to a PC by RS-232 connection. Electrodes were rinsed, polished, and re-rinsed before each experiment. Current density was approximately 1 mA/cm^2, and the charge loading rate (*CLR*), as defined previously, was 60 C/L/min. After electrolysis, the electrodes were removed, and the system underwent slow flocculation (60 rpm) with a magnetic stir-bar for 10 minutes. The solution was then immediately filtered without sedimentation on a new 0.45 μm PTFE membrane filter for analysis. Metal doses (mg Fe/L) were correlated with charge (C/L) by Faraday's Law, and a known current efficiency of φ=1 for SP water, as described in Chapter 4.

B.2.3 Chemical Coagulation

A custom 60 mL acrylic flocculation chamber was constructed for chemical addition and flocculation. Iron (II) sulfate ($FeSO_4 \cdot 7H_2O$) and iron (III) sulfate ($Fe_2(SO_4)_3 \cdot 5H_2O$) (Laboratory Grade, Fisher Scientific) were added to the chamber (Fe-equivalent doses of 3.6-57.6 mg Fe/L) and flocculated with a magnetic stir bar under high speed (900 rpm) for

60 seconds, followed by slow flocculation (60 rpm) for 10 minutes. The solution was then immediately filtered as in EC. For practical industrial comparison, pH was controlled in CC. Optimum coagulation pH was determined in a range of pH=5.5-7.0, in increments of 0.5, adjusted during flocculation by NaOH or H_2SO_4 (Laboratory Grade, Fisher Scientific).

B.2.4 EC Bench Scale Pilot

A continuous EC bench scale pilot was constructed out of acrylic, with a reactor liquid volume of 2.1 L, operating at a flow rate of 1-3 L/min. Fourteen electrodes (52 mm width x 370 mm height), seven cathodes and seven anodes, were connected in monopolar arrangement, with an inter-electrode spacing of 3 mm. The total anode electro-active surface area was 0.25 m^2. Due to the high surface area, current density (i) was low, in a range of 0.5-5 mA/cm^2 depending on dose. This also led to low H_2 (g) flux, preventing any floc removal by flotation. The mean residence time (τ), varied from ~40-60 s, depending on flow rate. The outlet of the EC reactor entered a slow flocculation chamber, consisting of a baffled 40 L upflow tank, with a 40 cm diameter vertical paddle impeller operating at 15 rpm. Samples were taken at the outlet of the flocculation chamber at ten minute intervals, and filtered on a new 0.45 μm PTFE membrane filter for analysis. To determine the effect of flocculation time, separate outlet ports on the flocculation chamber were utilized. To determine if pH adjustment had any effect on NOM removal, a dosing pump connected to a pH meter (DLX-PH-RX) was integrated into the flocculation chamber. Cell voltage (E_{cell})

was monitored (Fluke 189 logging voltmeter) and averaged over a 30 minute process time to determine average electrical consumption for cost analyses.

B.2.5 Analytical Methods

Filtrate was analyzed for remaining TOC by a UV/persulfate oxidation TOC analyzer (Shimadzu TOC-VCPH). pH was monitored with an ATC-pH probe (Denver Instruments, UB-10). Absorbance measurements were determined using a UV-Vis spectrophotometer, (Shimadzu UV-mini 1240) with a cell path of 1 cm. HPSEC analysis was performed as described in Chapter 2. All analytical measurements were performed within 2 hours of each experiment, and all experiments were performed in duplicate. Standard error is reported as error bars in all figures.

B.3 Results and Discussion

B.3.1 Comparison to Chemical Coagulation

DOC and UV-abs-254 removal with EC (i=5 mA/cm^2), Fe(II) sulfate, and Fe(III) sulfate are shown in Figure B-1. Optimum coagulation pH values for Fe(II) sulfate and Fe(III) sulfate were found to be 7.0 and 6.0, respectively, and were used for all further tests. The higher optimum pH for Fe(II) sulfate was likely due to the greater oxidation rate of Fe^{2+} to Fe^{3+} by DO at higher pH (Stumm and Lee, 1961), since flocculation took place under

atmospheric conditions, accelerated by the presence of NOM (Liang et al., 1993). For intermediate iron doses (14 mg Fe/L), EC performed better (DOC removal = 62.4%) than iron (II) sulfate (DOC removal = 53.4%), but worse than iron (III) sulfate (DOC removal = 71.9%). The trend in UV-abs-254 removal was similar, iron (III) sulfate had the lowest residual value of 0.0835 cm^{-1}, compared to EC, with UV-abs-254=0.0975 cm^{-1}. At higher doses (28 mg Fe/L), NOM removal by EC (DOC removal = 70.7%) was comparable to iron (III) sulfate (DOC removal = 73.8%). When pH was not controlled for in CC, DOC and UV-abs-254 removal had greater residual DOC and UV-abs-254, since pH dropped to pH ~ 4-5 due to alkalinity consumption, increasing solubility of iron and NOM species. However, since industrial drinking water treatment by iron CC always requires pH control, the results of CC without pH control was not further considered.

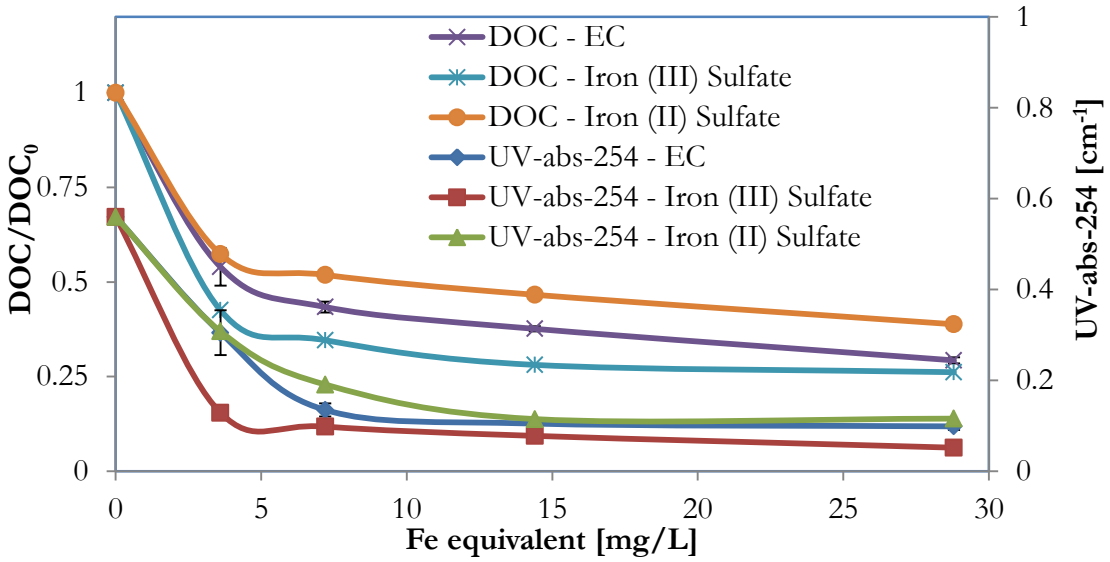

Figure B-1: EC vs CC, DOC and UV-abs-254, DOC_0=13.79 mg/L

Figure B-2 shows HPSEC AMW fractions comparing EC with the two metal salts at a dose of 7.2 mg Fe/L equivalent. HPSEC results confirm earlier findings of greater NOM removal with iron (III) sulfate with both absolute and relative (AMW fractionation) reductions in specific fractions. The relative reduction of the large NOM fraction (>1450 Da) was reduced by 42% with iron (III) sulfate. 27 % with EC, and 17% with iron (II) sulfate. This led to a greater relative fraction of smaller NOM fractions (< 550 Da) for iron (III) sulfate, although absolute reductions show similar residual fractions for both EC and iron (III) sulfate. This suggests that neither EC nor CC is competitively advantageous in removing small (< 550 Da) AMW fractions.

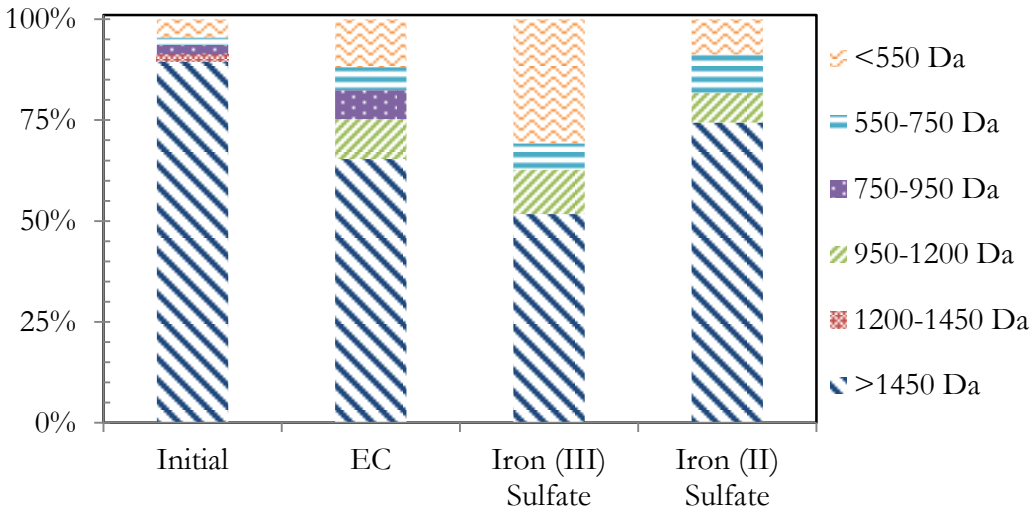

Figure B-2: EC vs CC, HPSEC peak-area normalized AMW fractions of initial and treated water (*ML* = 7.2 mg Fe/L).

At lower doses (≤ 14 mg Fe/L) NOM removal was lower with EC than iron (III) sulfate due to three phenomena: 1) EC generates only Fe^{2+} (Lakshmanan et al., 2009), which is more soluble than Fe^{3+} and known to complex quickly with NOM (Theis and Singer, 1974), preventing oxidation to Fe^{3+} especially at lower iron concentrations, 2) cathodic dissolved oxygen reduction, preventing Fe^{2+} oxidation, and 3) cathodic hydroxide generation, raising pH to ~7-8, beyond that of optimal coagulation for iron species. At greater doses (≥ 28 mg Fe/L), EC and CC had similar NOM removal, at a plateau removal of ~75%, where HPSEC confirmed only marginal and incremental removal of smaller AMW fractions, reaching the effective limit of the coagulation mechanism for either EC or CC. A plateau NOM removal of ~75% was also seen for EC with other NOM sources in Chapter 2. Findings of similar performance of iron EC and CC are in accordance with other comparisons (Bagga et al., 2008; Timmes et al., 2009), suggesting that EC without pH adjustment is a viable alternative to conventional iron CC, which generally requires pH adjustment in drinking water. Further work is required to optimize lower EC doses (≤ 14 mg Fe/L), including the possibility of a novel alloy anode or oxidation step to increase the rate of Fe^{2+} oxidation.

B.3.2 Continuous EC Bench Scale Pilot

Figure B-3 shows the NOM removal performance of the EC bench scale pilot for both the unaltered flow and for an adjustment to pH=6 in the flocculation chamber. Residual DOC instead of residual fraction is shown to better visualize actual performance. In both cases,

DOC removals were approximately 75-80 % in the dose range of 17-35 mg Fe/L, with an improvement of between 2-5% with pH adjustment. This is likely not significant enough to warrant the complexity of an industrial pH adjustment system, thus pH adjustment is not recommended unless further evidence shows significant improvement in bench-scale performance. The larger advantage of pH adjustment was an improvement in UV-abs-254, where pH adjustment led to a lower 0.035 cm^{-1} compared to 0.088 cm^{-1} for unadjusted pH. Since the absolute value of the UV-abs-254 in the outlet stream is far more important than relative removal in drinking water (for appearance, UV disinfection, etc.), this difference could be more significant.

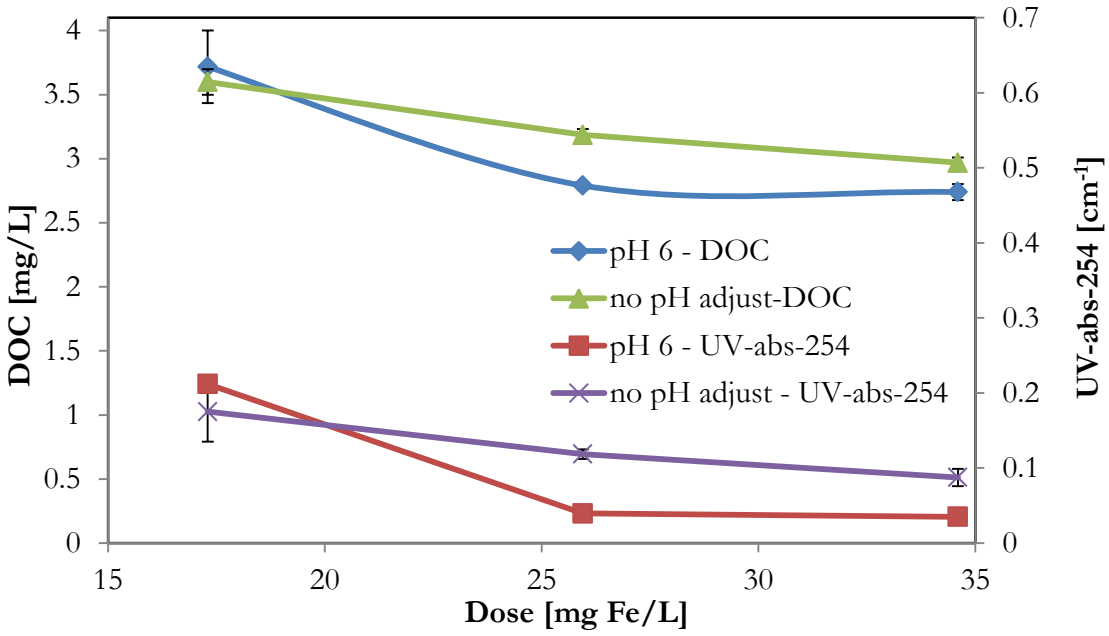

Figure B-3: NOM removal in continuous bench scale pilot, effect of pH adjustment

Figure B-4 compares the length of time the post-EC stream remains in the flocculation chamber. It is apparent that a longer flocculation time (20 min) increases NOM removal, as expected. Interestingly, at lower doses (17 mg Fe/L), there is little impact of flocculation time, likely due to unfavorable conditions (↑ pH and ↓ [Fe^{2+}]) for larger floc formation at lower doses, exemplified by the large residual UV-abs-254 of 0.20 cm^{-1} at this dose. As with CC, greater flocculation times often only have marginal gains in pollutant removal after a certain "optimal" flocculation time has been reached. A small sample determined optimum flocculation time in the bench scale pilot reactor at 40 min, after which only marginal gains were seen in NOM removal.

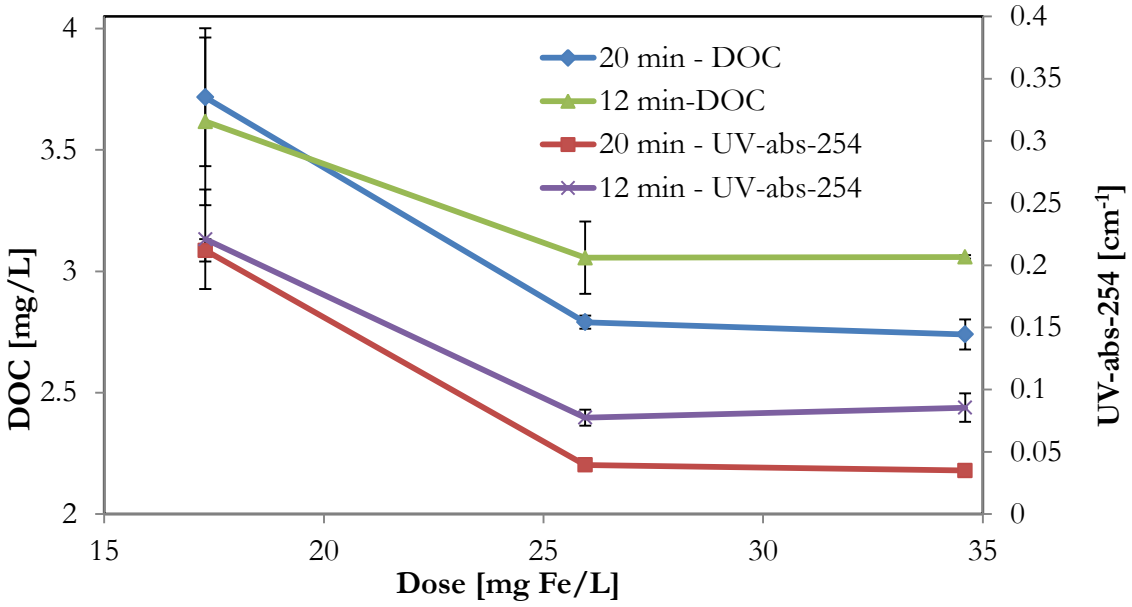

Figure B-4: NOM removal in continuous bench scale pilot, effect of flocculation time

B.3.3 Economics of EC bench scale pilot

A simple cost model of the EC bench scale pilot was applied to evaluate typical operating costs and approximate the capital cost of the system. For operating costs of the bench scale pilot, a flow rate of 3 L/min (~4000 L/day) was assumed, with a higher dose of 28.8 mg Fe/L for maximum NOM removal (Figure B-1), equivalent to CC. This gave a charge loading of 100 C/L and amperage of 5 A, assuming a Faradaic reaction and φ=1, which has been shown previously for EC with SP water in Chapter 4. Since total electro-active anode surface area was 0.25 m^2, i =2 mA/cm^2. A model relating E_{cell} to i for EC was described in Chapter 6, and a simplified version was solved numerically to give E_{cell}=2.18 V, which was approximately 10 % from the measured value of E_{cell}=2.41 V. Knowing E_{cell} and i, total power consumption was calculated as P_{cell}= 0.603 kWh/1000 L, corresponding to an electricity cost of $0.060/1000 L, assuming a nominal electricity cost of $0.10/kWh. Coagulant cost estimation assumed iron is purchased as sheet metal and machined into rectangular electrodes without waste at $2/kg, giving costs of $0.057/1000 L for coagulant. Assuming electrodes require replacement after 80% of total mass is used, total costs are $0.146/1000 L for consumables (electricity and metal), assuming no pH adjustment or salt dosing is used. If conductivity enhancing salts were used to enhance κ to 5000 µS/cm (possibly exceeding some total dissolved solids regulations), E_{cell} would be estimated at 1.68 V, and total costs would be $0.136/1000 L, saving only $0.01/1000 L with the conductivity enhancement.

Capital costs for the EC system alone include pumps, tanks, busbars, and a DC power supply, which are negligible at the bench scale. Recall that the EC reactor requires no fast-mixing impeller, unlike CC, since coagulant is already generated at the nanometre scale, allowing all micro mixing to take place *in-situ*. Capital costs are more relevant at greater scale, say 4 ML/day. Assuming electrodes can scale linearly (requiring 125 anodes of 1 m^2, in parallel plate or other electrode configuration), operating costs (electricity and metal) should remain the same. An electrode bank of this size would have a footprint of approximately 7.5 m x 1 m x 1 m, and the electrodes would last approximately six months before requiring replacement. A 5000 A DC power supply, transformer, and electrical connection cost estimation is ~ $200,000 (Magna Power). Assuming the most significant difference in capital cost between EC and CC is the DC electrical system, and the power supply cost can be distributed over a 20 year working life, EC operating costs show a total of $0.152/1000 L. For future comparisons, this value should be compared to CC operating cost, including: chemical supply and the 25 year distributed cost of the dosing pump, fast-mix impeller, and pH-control system, but not including other pumps, monitors, flocculation units, or filters (which would be required in both systems). These cost values are conservative, and industrial discounting of raw Fe metal (or possibly recycled Fe scrap material) and electrical costs could easily halve this estimation to $0.076/1000 L. This costing methodology will provide a simplified, but important decision making estimate for future EC evaluations and pilot studies.

B.4 Conclusion

A comparison of CC to EC in removing NOM from SP water showed that Fe (III) sulfate had approximately 10% better DOC and UV-abs-254 removal at lower doses (≤14 mg Fe/L), but approximately equivalent removal at higher doses (≥ 28 mg Fe/L). This suggests that EC, without the addition of conductivity enhancing salts or pH adjustment, is a viable alternative to ubiquitous CC. EC Bench scale pilot data confirm 75-80% NOM removal, and only marginal increases with pH control or conductivity enhancing salts, suggesting neither is necessary at scale.

Appendix C – Experimental Error and Analysis

In each chapter below, descriptions of experimental apparatus and procedures are given. Experimental results are either described in graphical form, where error bars represent standard error, or written form (e.g., 0.12 ± 0.02 mg/L) where the second number represents the absolute error (⊿*X*). Significant figures in all experimental results indicate the precision of experimental data. Calculations were of standard error (*SE*),

$$SE = \frac{\sqrt{\frac{1}{n}\sum_{a=1}^{n}(f_a - \mu)^2}}{\sqrt{n}}, \text{where } \mu = \frac{1}{n}\sum_{a=1}^{n} f_a \tag{C-1}$$

as well as relative standard error (*RSE*) to allow comparisons,

$$RSE = SE/\mu \times 100\% \tag{C-2}$$

and the student's T-test (*t*) for comparison of greater than one sample sets where appropriate:

$$t = \frac{\mu_1 - \mu_2}{\sqrt{\frac{\sigma_1^2}{n_1} - \frac{\sigma_2^2}{n_2}}} \tag{C-3}$$

where n is the number of experimental values, f is the a^{th} variable, μ is the mean, and σ is the standard deviation of the data set. For upper ($U_{95\%}$) and lower ($L_{95\%}$) confidence intervals for data points seen in graphical form, an approximation can be made as:

$$U_{95\%} = \mu + (SE \cdot 1.96) \tag{C-4}$$

$$L_{95\%} = \mu - (SE \cdot 1.96) \tag{C-5}$$

which states that there is a probability of 95% of the mean falling in between $\mu + (SE \cdot 1.96)$ and $\mu - (SE \cdot 1.96)$. Propagated relative systematic deviation (σ_x) due to individual instrumentation errors ($\sigma_1, \sigma_2, \ldots$) was determined by the root sum of squares approach:

$$\sigma_x = \sqrt{\sigma_1^2 + \sigma_2^2 + \cdots} \tag{C-6}$$

Error analysis details are given in each of Chapters 2 to 6.